



**FILTERED RAYLEIGH SCATTERING MEASUREMENTS IN A
BUOYANT FLOW FIELD**

THESIS

Steven Michael Meents, Captain, USAF

AFIT/GAE/ENY/08-M22

DEPARTMENT OF THE AIR FORCE

AIR UNIVERSITY

AIR FORCE INSTITUTE OF TECHNOLOGY

Wright Patterson Air Force Base, Ohio

APPROVED FOR PUBLIC RELEASE; DISTRIBUTION UNLIMITED

The views expressed in this thesis are those of the author and do not reflect the official policy or position of the United States Air Force, Department of Defense, or the United States Government.

**FILTERED RAYLEIGH SCATTERING MEASUREMENTS IN A
BUOYANT FLOW FIELD**

THESIS

Presented to the Faculty

Department of Aeronautics and Astronautics

Graduate School of Engineering and Management

Air Force Institute of Technology

Air University

Air Education and Training Command

In Partial Fulfillment of the Requirements for the
Degree of Master of Science in Aeronautical Engineering

Steven M. Meents, BS

Captain, USAF

March 2008

FILTERED RAYLEIGH SCATTERING MEASUREMENTS IN A BUOYANT FLOW FIELD

Steven M. Meents, BS

Captain, USAF

Approved:

//SIGNED//

Dr. Mark F. Reeder (Chairman)

14 March 2008

Date

//SIGNED//

Maj Richard E. Huffman (Member)

14 March 2008

Date

//SIGNED//

Dr. Robert B. Greendyke (Member)

14 March 2008

Date

Abstract

Filtered Rayleigh Scattering (FRS) is a non-intrusive, laser-based flow characterization technique that consists of a narrow linewidth laser, a molecular absorption filter, and a high resolution camera behind the filter to record images. Gases of different species have different molecular scattering cross-sections that become apparent as they pass through the interrogating laser light source, and this difference is used to discriminate between the different gaseous components. This study focuses on the behavior of a buoyant helium jet exiting horizontally into ambient air, and more specifically this jet's tendency to form side lobes that are discharged from the core fluid under low flow rate conditions. This jet behavior is documented and examined with relation to Froude, Grashof, and Reynolds numbers, and the behavior patterns are noted.

For my fiancée, whose love and support made this possible.

Acknowledgments

Laboratory experiments can be exceptionally challenging to accomplish, and even more so when working against a firm deadline. More often than not, anything that can go wrong with an experiment usually does, and this experiment was no exception to the rule. Thankfully, there were a few gentlemen that provided their assistance when it mattered most, and I'd like to take the time to thank them for their efforts.

First and foremost, I'd like to thank John Hixenbaugh for his outstanding laboratory support throughout this entire process. He put up with my countless questions and my never-ending parts lists that always needed to be ordered yesterday, and managed to do so without losing his sense of humor. He was always the first to tell me not to thank him since he was just doing his job, but without his support, I'm confident this project would have never moved past my random scribbling on a few sheets of paper. Thank you for *just* doing your job, John, and for doing it well.

I'd also like to thank Jay Anderson for his great technical support as well as Jan LaValley and the crew at the AFIT model shop for putting up with my less-than-stellar mechanical drafting skills; you really came through in a crunch for me. Jim Crafton at Innovative Scientific Solutions, Inc. also deserves special recognition; without his help, I'd probably still be trying to perform Filtered Rayleigh Scattering experiments with a broken iodine filter.

Last, but certainly not least, I'd like to thank my thesis advisor Dr. Reeder for his patience, wisdom, and encouragement. I hope this research benefits you as much as it has benefited me.

Steven M. Meents
Capt, USAF

Table of Contents

	Page
Abstract	iv
Acknowledgements	vi
Table of Contents	vii
List of Figures	x
List of Tables	xviii
List of Symbols	xx
List of Acronyms	xxii
1. Introduction	1
1.1 Background	1
1.2 Problem Statement	4
1.3 Research Objectives/Questions	5
1.4 Research Focus	5
1.5 Methodology	6
1.6 Assumptions/Limitations	7
1.7 Implications	7
2. Literature Review	8
2.1 Chapter Overview	8
2.2 Rayleigh Scattering	8

2.3	Molecular Absorption Filter	10
2.4	Filtered Rayleigh Scattering	13
2.5	Horizontal Buoyant Jets	14
2.6	Summary	18
3.	Methodology	20
3.1	Chapter Overview	20
3.2	Experimental Equipment	20
3.2.1	<i>Laser</i>	20
3.2.2	<i>Iodine Filter</i>	23
3.2.3	<i>Cameras</i>	25
3.2.3.1	<i>Cooke Corporation PCO.4000</i>	26
3.2.3.2	<i>Photron FastCam</i>	27
3.2.4	<i>Wavelength Meter</i>	28
3.2.5	<i>Power Meter</i>	32
3.2.6	<i>ThorLabs Optics</i>	33
3.2.6.1	<i>LMR2 lens mount with Spherical Lens</i>	34
3.2.6.2	<i>BSF10-A1 Beam Sampler</i>	34
3.2.6.3	<i>PF10-03-G01 Protected Aluminum Mirror</i>	34
3.2.7	<i>Other Optics</i>	34
3.2.7.1	<i>Cylindrical Lens</i>	35
3.2.7.2	<i>Spherical Lens</i>	35
3.2.8	<i>Aperture</i>	36
3.2.9	<i>Beam Trap</i>	37
3.2.10	<i>Flow Controllers</i>	38
3.2.11	<i>Compressed Gas</i>	42
3.2.12	<i>Traverse</i>	43
3.2.13	<i>Flow Field Box</i>	45

3.3	Experimental Setups	51
3.3.1	<i>Experimental Setup 1: Iodine Filter Characterization</i>	51
3.3.2	<i>Experimental Setup 2: Helium Flow Across Laser Sheet</i>	54
3.4	Experimental Methodology	56
3.4.1	<i>Iodine Filter Characterization Experiment Methodology</i>	56
3.4.2	<i>Fixed Froude and Reynolds Number Experiment Methodology</i>	57
3.4.3	<i>Trajectory Experiment Methodology</i>	65
3.5	Chapter Summary	67
4.	Results and Analysis	68
4.1	Chapter Overview	68
4.2	Experiment 1 Results: Iodine Filter Characterization.....	68
4.3	Experiment 2 Results: Fixed Froude Number Helium Flow	74
4.4	Experiment 3 Results: Fixed Reynolds Number Helium Flow	85
4.5	Experiment 4 Results: Helium Flow Trajectory	94
4.6	Summary of Helium Jet Results	101
5.	Conclusions and Recommendations	108
5.1	Research Conclusions	108
5.2	Significance of Research.....	109
5.3	Recommendations for Future Research	110
	Appendix A: Additional Iodine Filter Characterization Plots	112
	Bibliography	114
	Vita.....	117

List of Figures

Figure 1. Photograph of the exaggerated side lobes phenomenon taken during the previous research [9]. This phenomenon is a major focus of this document.	4
Figure 2. Simple mechanical model of a molecule. The nucleus in the center, shown with a positive charge, is connected to the electrons in the outer shell by springs with equal, linear spring constants (k).	9
Figure 3. Two photographs that show the difference between using a molecular absorption filter to block background scattering and not.	12
Figure 4. Illustration of the FRS concept. The plot on the far left shows the background/particle scattering signal and the molecular Rayleigh scattering signal. The middle plot shows the absorption spectrum of the molecular filter, and the plot on the far right shows the combination of the first two. The regions shown in red are the signals that make it through to the detector. .	14
Figure 5. The Coherent INNOVA® Sabre™ R Series Argon Ion Laser’s heat exchanger, power supply, laser head, and remote control key pad [25].	21
Figure 6. Diagram showing how each of the components of the Coherent laser system are connected during operation.....	22
Figure 7. Innovative Scientific Solutions Inc. iodine filter.....	24
Figure 8. The iodine filter’s two plugs. The power plug is a standard 120V, polarized, two-prong plug, and the thermocouple (light blue) is a type K, two blade miniature plug.	24
Figure 9. Cole-Parmer Digi-Sense temperature control box, showing a current iodine cell internal temperature of 20.3 °C, a set point of 90.0 °C, and currently not heating the cell.....	25
Figure 10. The Cooke Corporation PCO.4000 camera fitted with the Nikon Micro-Nikkor 85mm lens.	26

Figure 11. The camera, 85mm lens, iodine filter, and spherical lens as used during FRS experiments.	27
Figure 12. The Photron FastCam-X 1280 PCI camera system used for high speed imaging. The camera is fitted with an optional, smaller lens that was not used during testing.	28
Figure 13. The Bristol Model 621 Laser Wavelength Meter. The picture on the left (a) shows the main processing unit and where the fiber optic cable (yellow) from the sensor is connected. The picture on the right (b) shows the sensor itself mounted in a ThorLabs two-adjuster mirror mount.	29
Figure 14. Sample screen shot from the Bristol Instruments software, indicating a current laser wavelength of 1533.4614 nanometers, and an input power of 6.21 microWatts as measured in a vacuum [28].	29
Figure 15. The Bristol Instruments suggested method for aligning the wavelength meter's optical sensor. This method involves using a note card with a hole in the center, allowing the laser source to pass through while giving a surface to display the back reflections generated by the optical sensor. The ideal alignment will produce back reflections that symmetrically straddle the hole [28].	31
Figure 16. Alternate alignment method for the Bristol Wavelength Meter. The fiber optic cable (yellow) is removed from the processor and pointed at a business card. The picture on the left (a) shows the result of an improperly aligned sensor; the processor cannot read a signal of this intensity. The picture on the right (b) shows the intensity of laser light through a properly aligned sensor; the power reading is approximately 2.7 mW.	32
Figure 17. Coherent Fieldmaster power meter display on the left and the sensor on the right. The 7 nanoWatt reading displayed is a result of the ambient lighting conditions in the laboratory (no flash used in photograph).	33
Figure 18. Cylindrical lens and mount used to spread single laser beam line into a sheet of light.	35
Figure 19. Spherical lens and mount used in front of camera to magnify the region of interest and gather as much light as possible.	36

Figure 20. The mechanical aperture used in different parts of the experiments. The picture on the left (a) is a detailed view of the aperture, and the picture on the right (b) clearly shows the multiple beams that is has stopped from propagating further while still allowing the most intense to pass through unimpeded.	37
Figure 21. The Blue Sky Research Black Hole beam trap, shown with a simulated laser beam entering the device.	38
Figure 22. Alicat Scientific model number MCR-1500SLPM-D mass flow controller. The gas flows from left to right as pictured.	39
Figure 23. The Brooks Instrument 5850i mass flow controllers. The user interface box can control both units at the same time.	40
Figure 24. Compressed helium and nitrogen tanks and regulators used to supply the flow field box.....	42
Figure 25. The traverse and scissor jack are shown as attached to their respective adapter plates.	43
Figure 26. The scissor jack’s full range of motion of 2.25 in. The picture on the left (a) shows full extension, and the picture on the right (b) shows full compression.	44
Figure 27. The Anilam Wizard 150 power supply, joystick, and digital readout as connected to the traverse and scissor jack setup shown previously in Fig. 20. Note the display showing the maximum horizontal range of motion of 2.30445 inches.	45
Figure 28. Simple diagram showing the flow field box used in the previous AFIT research effort.....	46
Figure 29. The Plexiglas flow field box fully assembled and mounted to the scissor jack/traverse combination described earlier. The picture on the left (a) shows where the helium exits through the tube, and the picture on the right (b) shows how the box is attached to the scissor jack using a ThorLabs 90° angle bracket.	47

Figure 30. The aluminum plate that attaches to the back of the flow field box, shown assembled with the various fittings and adapters used during testing. The picture on the left (a) shows the back of the plate with the gray PVC through-wall fitting, the white stagnation chamber, and the inlets for the helium and nitrogen. The picture on the right (b) shows the tank washing nozzle that disperses the optional nitrogen co-flow. 48

Figure 31. Diagram showing the overall setup for the first experiment. The incident laser beam passes through three beam samplers, a spherical lens to increase the beam diameter, an aperture to block unwanted multiple beams from the beam samplers, and a mirror to turn the expanding beam 90°. After the beam passes through the iodine filter, it encounters another spherical lens that refocuses the beam back to a pinpoint, and its power is subsequently measured by the power meter. 51

Figure 32. Picture showing the expansion of the laser beam by placing a business card directly in front of the iodine filter..... 52

Figure 33. Pictures showing the power meter’s sensor, spherical lens, and iodine filter mounted in a box with the front panel removed. The picture on the left (a) shows the sensor and the lens without the filter in place, and the picture on the right (b) shows the filter in place and ready for testing..... 53

Figure 34. Diagram depicting the second experimental setup. The laser beam is spread into a sheet of light with a cylindrical lens, and passes through a slotted board that keeps background reflections produced by the laser itself to a minimum. The traverse, scissor jack, and flow field box are placed so that the helium jet intersects the laser sheet, and the camera is placed opposite the jet to record the images. The laser sheet passes through one more slotted board and is stopped with a makeshift beam block. 54

Figure 35. Picture showing one of the slotted boards used in the second experimental setup. Note the green glow that the board stops from further propagation while still allowing the incident laser beam to pass. 55

Figure 36. Four separate images collected at four different exposure rates. The upper left picture (a) was taken at an exposure rate of 25 milliseconds, and the rest of the images are similarly labeled with their respective exposure rates. 59

Figure 37. Plot showing the average raw intensity values for each of the frame rates examined.	60
Figure 38. A random, false-color image as processed by Matlab, and presented as a grayscale image. The dark spot is the helium jet as it crosses the laser sheet.	62
Figure 39. A screen capture of a single frame of data taken while helium was being expelled from the 1/8" O.D. tube. The helium is barely visible as the darkest spot in the image, and is surrounded by the reflection of the outside of the tube that appears white to the left and below the helium jet.	63
Figure 40. An example set of data reduced images. The image on the left shows the helium concentration that varies from 0 – 100%, and the image on the right shows the standard deviation that varies from 0 – 25%.	65
Figure 41. Mean helium concentration where the origin represents the center of the tube and not the center of the helium jet. From left to right, the normalized distances are $x/d = 2, 4, 6$, and 8 , respectively. Note that by the time $x/d = 8$, the center of the helium jet has moved nearly a full radius to the right of the center of the tube.	66
Figure 42. Results of the iodine filter characterization for the two filters available for testing plotted versus wavenumber. The black lines represent three separate runs for the first filter, and the red lines represent the three runs provided by the second, deeper filter.	69
Figure 43. Results of the iodine filter characterization for the two filters available for testing plotted versus relative frequency.	70
Figure 44. Results of the characterization of iodine Filter 2 at various temperatures. Note the decrease in incident light absorption as the filter temperature is decreased.	72
Figure 45. Results of the characterization of iodine Filter 2 at various temperatures. Note the decrease in incident light absorption as the filter temperature is decreased.	73
Figure 46. Two sets of four consecutive images representing the conditions listed in Table 4 taken at an exposure rate of 80 ms.	75

Figure 47. Mean helium concentration and standard deviation for the same conditions listed in Table 4, averaged over 50 images taken at an 80 ms exposure rate.	76
Figure 48. Three sets of four images representing the conditions listed in Table 5 taken at an exposure rate of 80 ms.	77
Figure 49. Mean helium concentration and standard deviation for the same conditions listed in Table 5, averaged over 50 images taken at an 80 ms exposure rate.	79
Figure 50. Three sets of four images representing the conditions listed in Table 6 taken at an exposure rate of 80 ms.	81
Figure 51. Mean helium concentration and standard deviation for the same conditions listed in Table 6, averaged over 50 images taken at an 80 ms exposure rate.	82
Figure 52. Two sets of four images representing the conditions listed in Table 7 taken at an exposure rate of 80 ms.	83
Figure 53. Mean helium concentration and standard deviation for the same conditions listed in Table 7, averaged over 50 images taken at an 80 ms exposure rate.	84
Figure 54. Five sets of four images representing the conditions listed in Table 8 taken at an exposure rate of 80 ms.	86
Figure 55. Mean helium concentration and standard deviation for the same conditions listed in Table 8, averaged over 50 images taken at an 80 ms exposure rate.	88
Figure 56. Four sets of four images representing the conditions listed in Table 9 taken at an exposure rate of 80 ms.	90
Figure 57. Mean helium concentration and standard deviation for the same conditions listed in Table 9, averaged over 50 images taken at an 80 ms exposure rate.	91

Figure 58. Two sets of four images representing the conditions listed in Table 10 taken at an exposure rate of 80 ms.	92
Figure 59. Mean helium concentration and standard deviation for the same conditions listed in Table 10, averaged over 50 images taken at an 80 ms exposure rate.	93
Figure 60. Four sets of four images representing the conditions listed in Table 11 taken at an exposure rate of 80 ms.	95
Figure 61. Mean helium concentration and standard deviation for the same conditions listed in Table 11, averaged over 50 images taken at an 80 ms exposure rate.	96
Figure 62. Four sets of four images representing the conditions listed in Table 12 taken at an exposure rate of 80 ms.	98
Figure 63. Mean helium concentration and standard deviation for the same conditions listed in Table 11, averaged over 50 images taken at an 80 ms exposure rate.	99
Figure 64. The trajectory of the jets as viewed from the top looking down in terms of the normalized horizontal distance as related to the tube radius compared to the normalized distance the jet has traveled from the tube exit as related to the tube diameter.	100
Figure 65. Scatter plot of all 21 data points taken at $x/d = 4$ plotted against the square root of the Grashof number and the Reynolds number. The black circles indicate that helium side lobes occurred under the conditions present at that point, and the red squares indicate data points where this phenomenon was not observed.	105
Figure 66. Single image taken from Fig. 54 (d) showing the formation of helium side lobes at a Froude number of 4.59 and a Reynolds number of 241.69. One of the side lobes, circled in black, is larger than the others.	106
Figure 67. Results of the iodine filter characterization for the two filters available for testing plotted versus wavelength. The black lines represent three separate runs for the first filter, and the red lines represent the three runs provided by the second, deeper filter.	112

Figure 68. Results of the characterization of iodine Filter 2 at various temperatures plotted versus wavelength.....	113
--	-----

List of Tables

Table 1. Absolute viscosity (η) values at 25°C for air, helium, methane, and nitrogen [35].	41
Table 2. The outer diameter, inner diameter, and length normalized by the inner diameter for each of the seven tubes available for this experiment. Each tube is approximately 13 inches in length.....	49
Table 3. The worst case (highest) flow rate conditions for each of the tubes used during this research. The Reynolds number is based off of each tube's inner diameter and the highest flow rate used for that tube. The entry length required is shown in terms of the number of diameters required.	49
Table 4. Fixed Froude number of 2 (approx.) test conditions.	74
Table 5. Fixed Froude number of 10 (approx.) test conditions.	77
Table 6. Fixed Froude number of 14 (approx.) test conditions.	80
Table 7. Fixed Froude number of 30 (approx.) test conditions.	83
Table 8. Fixed Reynolds number of 240 (approx.) test conditions.....	85
Table 9. Fixed Reynolds number of 400 (approx.) test conditions.....	89
Table 10. Fixed Reynolds number of 670 (approx.) test conditions.....	92
Table 11. Trajectory experiment test conditions at a fixed Reynolds and Froude number.	94
Table 12. Trajectory experiment test conditions at a fixed Reynolds and Froude number. The Froude number has remained nearly constant compared to the previous set of data.	97

Table 13. Flow conditions where the crescent moon to the right is present as the dominant jet behavior determined from the mean helium concentration of the 100 images taken for each flow condition.	102
--	-----

Table 14. Flow conditions where helium side lobes were present in the helium jet determined from examination of the images for each set of conditions.	104
---	-----

List of Symbols

English Symbols

BG	Background
c	Speed of Light
CH ₄	Methane
D	Diameter
E	Irradiating Intensity
f	Frequency
Fr	Froude Number
GHz	GigaHertz
Gr	Grashof Number
He	Helium
Hz	Hertz
I	Collected Power
L _e	Entry Length
mW	MilliWatts
N ₂	Nitrogen
nW	NanoWatts
Q	Flow Rate
Re	Reynolds Number
SiO	Silicon Monoxide

Greek Symbols

η	Absolute Viscosity
λ	Wavelength
μW	MicroWatts
ν	Kinematic Viscosity
ρ	Density
Σ	Summation
σ	Rayleigh Scattering Cross-Section
X	Species Mole Fraction

List of Acronyms

AFIT	Air Force Institute of Technology
CCD	Charge Coupled Device
CW	Continuous Wave
FPS	Frames per Second
FRS	Filtered Rayleigh Scattering
HVAC	Heating, Ventilation, and Air Conditioning
ISSI	Innovative Scientific Solutions, Inc.
LIF	Laser Induced Fluorescence
Nd:YAG	Neodymium Yittrium Aluminum Garnett
PIV	Particle Image Velocimetry
SLPM	Standard Liters per Minute
TSM	Tunable Sealed Mirror

FILTERED RAYLEIGH SCATTERING MEASUREMENTS IN A BUOYANT FLOW FIELD

1. Introduction

1.1 Background

Scientists and engineers alike have used many different methods throughout the years to characterize different types of flow fields. These methods include, but are not limited to, the use of hot-wire anemometers that correlate the resistance across a heated wire to flow velocity, pitot probes that relate pressure to velocity, and thermocouples that relate temperature to velocity. An inherent disadvantage to using any of the listed methods is the requirement of placing a device in the flow field, thus altering the fluid flow from what it would have been had a non-intrusive measurement technique been used. Additionally, the data acquisition procedure becomes time-intensive since the measurement device can only gather data on a point-by-point basis, often requiring the use of a multi-axis, automated traverse to help accelerate the process.

In order to keep from altering the flow field due to physically placing the measurement device in the flow, several non-intrusive measurement techniques have been developed over time that have greatly enhanced our understanding of fluid flows. One such method is particle image velocimetry (PIV), and involves illuminating a flow field that has been seeded with small particles while taking a series of images with a camera [1]. The small particles are assumed to follow the flow field, and the comparison of a time-series of images thus leads to a quantitative measurement of the fluid velocity vectors at a very large number of points simultaneously [1]. This method has proven to be both reliable and insightful, but the problem still remains that the

flow field must be seeded with particles for PIV to work properly. Flow field seeding can be especially problematic with high speed flows (Mach number 2+) due to the high likelihood of turbulence and the need to accelerate the relatively large mass of the particles to the high rates of speed being studied [2]. Additionally, seeding a flow can be just as challenging in the presence of large density gradients, such as can be found when mixing air with a buoyant gas like helium. It is difficult, at best, to uniformly mix the particles throughout the flow field when these density gradients exist. This challenge warrants the use of a molecular-based measurement approach.

Filtered Rayleigh Scattering (FRS) is a non-intrusive, laser-based flow characterization technique that was developed in the late 1980s and presented in early 1990 by Richard Miles and Walter Lempert [2]. Filtered Rayleigh Scattering was introduced as a solution to the shortcoming of characterizing high speed flows using point measurement techniques such as hot-wire anemometry, image based techniques including schlieren photography, and particle scattering approaches like PIV [2]. The fundamental principles that govern this measurement technique are the same as those observed by Lord Rayleigh when he showed that the color of the sky is caused by the scattering of light off of air molecules, known today as Rayleigh scattering [3].

Rayleigh scattering had long been looked at as a prime candidate for a flow diagnostic technique, but had inherent drawbacks that limited its effectiveness [2]. Rayleigh scattering occurs at roughly the same frequency as the light source, and is therefore subject to background interference from scattering caused by surfaces such as walls and tables, reflections from various optical components, and even particles in the flow field [2]. An atomic or molecular filter, typically one containing gaseous iodine or mercury [4], placed between the light source and the light detector provides an absorption notch that blocks certain wavelengths of light, yet allows

others to pass unimpeded. If the wavelength of the light source is adjustable, it can be set such that it coincides with the filter's absorption notch, thus blocking the unwanted scattering signals produced by background reflections and particles that are relatively motionless compared to the flow field being analyzed. Molecules in motion cause a Doppler-shift in the frequency of the light source, and thus the Doppler-shifted scattered light from the moving molecules of interest is allowed to pass through the filter [2]. This filter is a critical component of FRS, and allows measurements to be taken in less than ideal environments such as any laboratory that is not enclosed in a clean-room type of environment.

A typical FRS setup includes a narrow-linewidth laser used as the light source, a small absorption filter, and a high-resolution camera behind the absorption filter to collect the images. The original application of the FRS technique was to collect data concerning high speed flow regimes [2], and through further development, the technique has been used to collect species concentration, temperature, velocity, and density data [5]. This technique can also be used to examine low speed flows including buoyant jets.

Buoyant jet flows are different from a standard jet flow due to the presence of a large density gradient between the gas or liquid being expelled from the jet nozzle and the surrounding environment. Buoyant jets are present in such media as water, and more specifically have been studied in the transport of pollutants into a body of water [6]. Buoyant jets are also encountered in the form of diffusion flames that are present in a variety of industrial and fire safety problems [7]. Understanding the dynamics of these buoyant diffusion flames can lead to a more efficient and environmentally clean combustion process, and also enhance fire safety [7]. While these studies discuss buoyant jets, neither directly cover the study of horizontal buoyant jets, but they both show the importance of being able to appropriately account for the mixing behavior of two

fluids where a density gradient is present. The research in this document will describe the mixing behavior of a horizontal buoyant jet in the form of helium as it is expelled from various sized nozzles into air, and lend some insight as to why this particular type of jet behaves as it does.

1.2 Problem Statement

This research continues two previous efforts conducted at the Air Force Institute of Technology (AFIT) aimed at setting up an FRS system for the purpose of evaluating a flow field. The first of these efforts had the goal of setting up the FRS system, using it to generate flow visualizations and gather qualitative data [8]. The second effort focused on gathering quantitative data in the form of species concentrations, and also highlighted mixing behaviors that indicated the formation of exaggerated side lobes that were being expelled from the center of a helium jet at relatively low flow rates [9]. A picture of this phenomenon from the previous AFIT research is shown below:

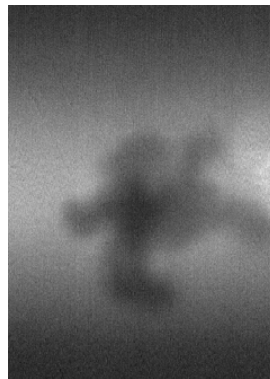


Figure 1. Photograph of the exaggerated side lobes phenomenon taken during the previous research [9]. This phenomenon is a major focus of this document.

This research effort is intended to further the understanding of the causes behind this mixing behavior by modifying the flow field to allow the quick changing of nozzle diameters to vary the Reynolds, Froude, and Grashof numbers and observing the corresponding changes in mixing behavior.

Additionally, this research is intended to provide another set of data that can be used in describing and understanding gaseous horizontal buoyant jets. The vast majority of the research available on buoyant jets is related to jets that issue vertically, and other research that has tracked horizontal jet trajectory has typically been water-based using other measurement techniques. This document will offer valuable insight into the behavior of a helium-based horizontal buoyant jet, and the ability to relate this type of flow to others with similar density gradients.

1.3 Research Objectives/Questions

The primary objective of this research is to gather a large amount of data about the behavior of a helium jet expelled horizontally into air as the Reynolds, Froude, and Grashof numbers are systematically changed. These non-dimensional parameters will be chosen to try and create different conditions where helium side jets are formed, and this behavior will be examined in terms of helium concentration and standard deviation. Secondary objectives involve the evaluation of the iodine filter used in this setup as well as gathering additional trajectory and species concentration data.

1.4 Research Focus

The current AFIT FRS setup including an argon-ion, continuous wavelength laser, an iodine filter, and a charge-coupled device (CCD) high resolution camera will be evaluated for effectiveness with the addition of a wavelength meter. The iodine filter's absorption profile will

be examined, revealing the wavelength of the laser that corresponds to the middle of one of the filter's absorption notches so that background scattering signals are almost entirely eliminated. The laser will then be held to this wavelength via its internal etalon temperature throughout testing while ensuring that the camera's acquisition frame rate is set such that it gathers data as quickly as possible while still allowing enough light to provide a high signal-to-noise ratio. Finally, a new flow field device that directs the helium jet will be constructed that will allow various non-dimensional parameters including the Reynolds and Froude numbers to be quickly and easily changed during testing.

1.5 Methodology

Testing will include two separate experimental setups that are used to perform four total experiments. The first setup and experiment will characterize the iodine filter's absorption profile, revealing the laser beam wavelength that corresponds with one of the filter's absorption notches. The second experimental setup will take the laser beam and spread it into a sheet of light with a cylindrical lens, and the flow field device will be positioned so that the jet of helium will cross the light sheet's path while a camera directly opposite the jet photographs its behavior. The first experiment with this setup will vary the Reynolds number of the helium jet as the Froude number is held constant, and any behavior patterns will be documented and examined in terms of helium concentration and standard deviation. A second experiment will be identical to the first, only this time the Froude number will be varied while holding the Reynolds number constant. A third and final experiment will look at the helium jet's trajectory as it is moved various distances away from the laser sheet.

1.6 Assumptions/Limitations

The iodine filter is characterized so that the optimal laser light wavelength is known, but the laser itself is subject to fluctuations in etalon temperature, which directly impacts the stability of the wavelength. Therefore, it will be necessary to ensure that the laser's wavelength has not drifted during data gathering sessions, thus altering the amount of unwanted backscattering that is allowed to reach the camera through the iodine filter. Additionally, the flow rate of the helium is assumed to be accurate, but is subject to the errors inherent to the mass-flow controller used.

1.7 Implications

This research further enhances the knowledge of the FRS system at AFIT, and of low-speed horizontal buoyant jets. In the interest of time, the amount of data that can be gathered must be limited, but the included work will allow future researchers to quickly and easily gather a large amount of data in a short period of time that can then be extensively examined to provide a great deal of insight into this particular flow field's behavior. Eventually, this system could be used to evaluate velocity and species concentration measurements in a supersonic wind tunnel.

2. Literature Review

2.1 Chapter Overview

The intent of this research is to foster a better understanding of the behavior of horizontal buoyant jets with the use of the Filtered Rayleigh Scattering flow field characterization technique. Filtered Rayleigh Scattering will be fully explored by first presenting the underlying physics of Rayleigh scattering. The atomic/molecular filters designed to enhance Rayleigh scattering measurements will be discussed next, and finally the entire FRS setup will be described including the basic principles of how everything fits together and what equipment is typically used to accomplish FRS measurements. Latter discussions will focus on the physics of horizontal buoyant jets, thus giving a full picture of the scope of this research.

2.2 Rayleigh Scattering

The study of atmospheric optics has long captivated the human imagination. The changing color of the sky, the moon, and the sun have often been sources of wonder and amazement, and have given rise to weather lore embraced by farmers and sailors alike [3]. Early scientists surmised that the changing light patterns in the sky were caused by particles in the air, but many of these theories could not be tested. Bouguer and de Saussure suggested that the color of the sky was caused by the air itself, but had no way to back up that claim [3]. Newton guessed that water droplets in the atmosphere reflected the light as thin plates, and Clausius contended that the color of the sky was due to reflections from small water bubbles [3]. While these explanations seemed to have merit at the time, they all failed to correctly describe the source of the color of the sky.

John William Strutt, the third Baron of Rayleigh, or more commonly known as Lord Rayleigh, was the first to offer a correct explanation of the color of scattered light as it passes through the atmosphere [3]. He used a simple mechanical model of an air molecule that consisted of a positively charged nucleus surrounded by a shell of negatively charged electrons [5]. The elements of the molecule are held together by forces that are represented by ideal springs with linear spring constants, and the molecule is assumed to be in electrical equilibrium (non-ionized) with the negative charges evenly distributed throughout the electron cloud (non-polarized) [5]. Additionally, this mechanical model is assumed to be lightly damped so that the amplitude of the motion between the nucleus and electron cloud does not grow unduly large near the system's resonant frequencies [3]. A simple diagram of this mechanical model of a molecule is shown below in Figure 2:

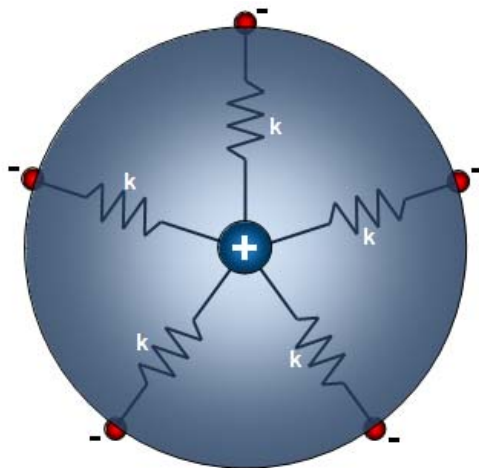


Figure 2. Simple mechanical model of a molecule. The nucleus in the center, shown with a positive charge, is connected to the electrons in the outer shell by springs with equal, linear spring constants (k).

When the system in Figure 2 is subjected to an electromagnetic field, the electric charges are redistributed, thus bringing the positive and negative charges to a new equilibrium position. This

creates an induced dipole that aligns itself with the impinging electric field. According to Lenz's law, which states that the magnetic field of any induced current opposes what caused it, the dipole tries to counteract the electric field's action [5]. If the electromagnetic field is replaced with an electromagnetic wave, the induced dipole will follow the temporal variations of the electric field, thus producing a secondary wave that propagates away from the dipole [5]. This secondary wave, or scattering, is said to be in the Rayleigh regime if the particle size is less than one tenth the wavelength of the incident electromagnetic wave [3]. Most molecules are considered to be subject to Rayleigh scattering since they are generally less than one tenth the size of visible light wavelengths, which range from 400 to 700 nanometers.

The intensity of the scattered light when compared to that of the source of illumination reveals how much energy is being drawn from the primary wave and sent in all directions. This is known as the Rayleigh scattering cross-section. For helium, this ratio is 1.4 percent [10].

2.3 Molecular Absorption Filter

In order to improve the quality of data from FRS techniques, it is necessary to spectrally modify the shape of the Rayleigh scattering spectrum [5]. Spectral modification can be accomplished with the use of a molecular absorption filter. A molecular absorption filter is typically made by enclosing a certain type of gas in a closed glass tube, which is then placed in front of the camera. Different types of molecular species have been investigated for use in these filters, including both iodine and mercury [4]. Each of these molecules in gaseous form has a high vapor pressure, which allows them to be operated only slightly above room temperature when enclosed in a glass tube [4]. Consequently, the overall construction and power requirement of the molecular filter is greatly simplified.

A molecular absorption filter must meet a handful of requirements before it can be considered for use during FRS experiments. First, and most obvious, the absorption filter must be able to absorb energy in the same wavelength range as the source of illumination. In the case of FRS, this means that the filter has to be able to absorb light around the same wavelength as the laser being used to interrogate the flow field. Second, the absorption band selected should have sharp frequency cut-off edges, and preferably be much narrower than the width of the Rayleigh scattering spectrum [5]. Finally, the filter's light transmission outside of the selected absorption notch should be as close to 100% as possible to prevent signal attenuation while at the same time allowing hardly any light to pass in the deepest portion of the notch [11]. Ideally, the amount of light absorbed, referred to as the extinction ratio, should be adjustable to suit different applications. High extinction ratios are desirable when trying to block strong background reflections, such as when examining a flow field that is near a surface like a table [5].

Iodine filters are the clear choice in most FRS studies due to their favorable absorption profiles that correlate to a 532 nm wavelength, which is the same wavelength as the widely-used Nd:YAG pulsed laser system [12]. The vast majority of the mapping of the iodine filter absorption profiles has been accomplished around the Nd:YAG laser's operating wavelength due to its popularity, and Forkey developed and verified a code that mapped the iodine absorption profile in [13]. Fortunately, the absorption notches of iodine filters cover a broad enough range of wavelengths that they can also be accessed by argon-ion lasers, which operate at a lower frequency than the Nd:YAG systems [14].

Researchers using frequency notch filters have been able to successfully reduce background scattering from walls and windows in flow visualizations, measure flow properties including velocity and temperature, and also measure multiple flow field properties

simultaneously. The absorption of background scattering can drastically improve overall image quality as can clearly be seen in the figure below:

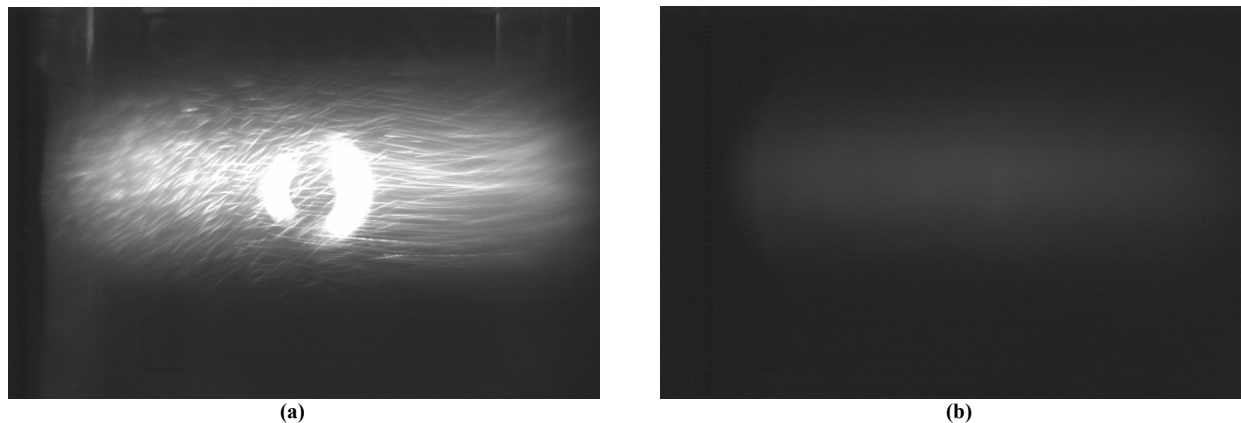


Figure 3. Two photographs that show the difference between using a molecular absorption filter to block background scattering and not.

The photograph on the left (a) is a picture of an ambient air flow field being illuminated with an argon-ion laser set to a wavelength of 514.5 nm. The circular object in the center of the picture is the end of a stainless steel tube that is glowing due to its close proximity to the laser sheet. The picture on the right (b) is the same exact image, only taken through an iodine filter set to a temperature of 90°C. The background particles have vanished, and the outline of the tube exit is nearly gone as well. This also shows a less than ideal situation; the laser light has been attenuated in the process.

There are many advantages to using an atomic/molecular filter instead of optical filters like interferometers or spectrometers that also block and transmit light at certain wavelengths. The molecular filter has the ability to look at a larger area of the flow field than a typical narrow slit spectrometer while still maintaining the ability to transmit and block certain wavelengths [4]. The broad field of view is beneficial since most flow fields are relatively large in nature, and the

desire is to photograph the entire field at once. Furthermore, molecular filters, in general, can block more unwanted background reflections than a typical interferometer filter and spectrometer, and also have wider acceptance angles to help resolve light from an image plane [11].

2.4 Filtered Rayleigh Scattering

The concept of Rayleigh scattering when combined with a molecular absorption filter are all that is required to accomplish Filtered Rayleigh Scattering measurements. A typical FRS setup includes a narrow linewidth laser to illuminate the flow field, an absorption filter, and a detector mounted behind the filter. In most techniques, the laser beam is either focused to a small volume or formed into a sheet of light that interrogates the flow field of interest [5]. The incident light from the laser encounters the gas molecules in the flow field, and a portion of the light is scattered. This scattered light, whether it is from molecules or particles, contains information about the fluid flow properties. Particle scattering is shifted in frequency due to the Doppler effect, but since they have a relatively large mass when compared to molecules, their spectral linewidth is approximately equal to that of the source of illumination [5]. The spectral linewidth for molecular scattering is much broader than that of a particle, and is what makes a molecular absorption filter ideal since it can block the narrow particle linewidth while allowing the broader molecular signal to pass. The FRS concept is shown as a series of plots in the figure on the following page [5]:

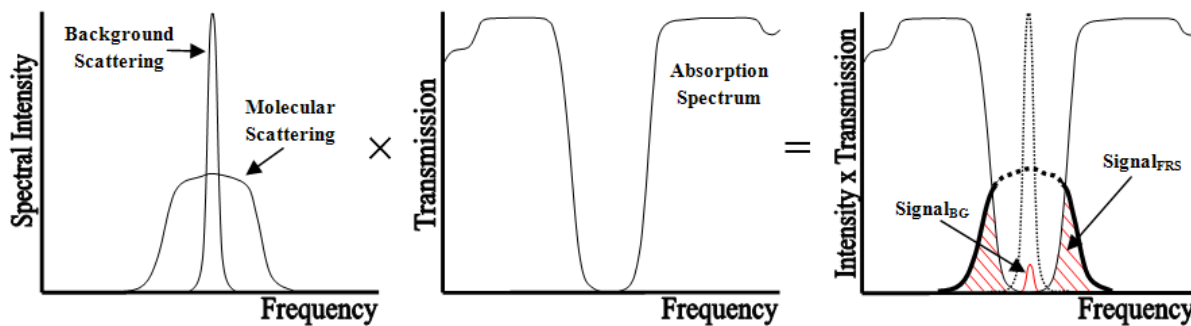


Figure 4. Illustration of the FRS concept. The plot on the far left shows the background/particle scattering signal and the molecular Rayleigh scattering signal. The middle plot shows the absorption spectrum of the molecular filter, and the plot on the far right shows the combination of the first two. The regions shown in red are the signals that make it through to the detector.

Figure 4 clearly shows the contributions from each of the signals that make up the entire FRS signal. Note that some of the background signal still makes it through to the detector as shown by the small red curve in the plot on the far right. Some background signal bleed-through is unavoidable since some of the signals, usually from larger particles, have enough intensity to overpower the ability of the filter to absorb that light.

2.5 Horizontal Buoyant Jets

Jet flows are present in many different real world scenarios, and have applications in aerodynamics, industrial processing, and even civil engineering. A buoyant jet is marked by its core having a lower density than its ambient surroundings, thus causing the jet's motion to oppose the force of gravity. Horizontal buoyant jets are injected into ambient conditions perpendicular to the force of gravity. A simple example can be seen on a cold day in the form of an automobile's exhaust rising into the air. A horizontal buoyant jet is noted for its trajectory that has an upward curve to it, and this type of jet is of great interest to many, but has not received nearly as much attention in the scientific world as the vertical buoyant jet.

Buoyant jets, like many other phenomena, are usually described in terms of non-dimensional parameters for ease of comparison. Typical parameters include, but are not limited to the Reynolds, Froude, and Grashof numbers. These non-dimensional parameters are described in Equation 1 [15]:

$$\begin{aligned}
 \text{Reynolds Number } (Re) &= \frac{\text{Inertial Forces}}{\text{Viscous Forces}} \\
 \text{Froude Number } (Fr) &= \frac{\text{Inertial Forces}}{\text{Gravitational Forces}} \\
 \text{Grashof Number } (Gr) &= \frac{\text{Gravitational Forces}}{\text{Viscous Forces}}
 \end{aligned} \tag{1}$$

For the purposes of this research, these equations take on the following forms:

$$\begin{aligned}
 Re &= U_{jet} \times \left(\frac{d}{\nu} \right) \\
 Fr &= \frac{U_{jet}}{\left(g \times d \times \sqrt{\left(\frac{\rho_{\infty} - \rho_{jet}}{\rho_{jet}} \right)} \right)} \\
 Gr &= \left(\frac{Re}{Fr} \right)^2
 \end{aligned} \tag{2}$$

where U_{jet} is the jet velocity, d is the tube diameter, ν is the kinematic viscosity, g is the gravitational constant, and ρ is the density. These non-dimensional parameters are used to characterize the flow regime of the jet they represent.

The Reynolds number is typically referenced to provide insight into whether a flow is laminar or turbulent. The Froude number is often used as a characteristic value when gravitational (or buoyancy) forces are important. The Grashof number becomes important when the ratio of buoyancy to viscous forces increases. When combined, the Grashof and Reynolds

numbers are used to describe a flow in terms of either forced, free, or mixed convection [16]. If the Grashof number is much less than the Reynolds number squared, forced convection dominates the flow. Free convection dominates for the opposite condition. If the Grashof number is on the same order as the Reynolds number squared, both forced and free convection are important players.

The helium flow rates chosen in this research have different values for the Grashof, Reynolds, and Froude numbers, all of which are calculated based off of their respective flow conditions. The diameter of the tube through which the helium flows is a known, measured value, and the velocity of the helium flow is kept as a variable. The tube diameter, measured in inches, is converted to meters, and the cross-sectional area of the tube is then calculated in units of meters squared. A velocity is picked in units of meters per second and multiplied by the cross-sectional area of the tube to give a flow rate in units of cubic meters per second. The cubic meters are then converted to liters, giving a flow rate in terms of liters per second, and with one more unit conversion to convert seconds to minutes, the final helium flow rate based off of the chosen velocity is known in terms of liters per minute. This form is useful since the mass flow controllers used in this experiment display the flow in terms of standard liters per minute (SLPM). Helium's density is a known value, so the mass flow rate of helium can also be shown in units of kilograms per second. All of the above information, combined with the published value for helium's kinematic viscosity, is used to calculate the Reynolds, Froude, and Grashof numbers using the equations presented in Eq. (2).

Typical studies of laminar and turbulent buoyant jets are accomplished using many different flow characterization techniques, including shadowgraph photography, laser sheet lighting, and even thermocouples physically inserted into the flow. These flow characterization

techniques do not rely on seeding the flow with particles or dyes, which is very important when dealing with a gas phase experiment where large density gradients exist since uniform seeding is very challenging in this environment. The authors in [17] successfully seeded a jet flow and characterized it using LIF, but only a small density gradient existed in their flow field of interest. Different molecular-based measurement approaches, including Filtered Rayleigh Scattering, can give valuable information about a buoyant jet without the need to modify the flow field.

The study of jet flows often examines the rate at which the jet entrains the ambient or outer fluid; this mixing rate is of great interest to those trying to improve combustion efficiency. The fluctuations associated with the mixing region of the jet can be characterized by using a simple standard deviation plot, as seen in [17] and [18]. The standard deviation plot is derived from examining the time variation in species concentration as flow field measurements are taken. The mixing region corresponds to a higher standard deviation value, whereas the core region shows a much lower value for the standard deviation. These mixing regions often contain interesting flow patterns that happen at various conditions.

The authors in [19] studied the phenomenon of the bifurcation of a horizontal, buoyant laminar jet in terms of the Reynolds and Grashof numbers. The buoyant jet in this study consisted of fresh water exiting from a nozzle into a brine solution at a relatively low rate of flow. Under certain conditions, this laminar jet would bifurcate, which was essentially a small plume that separated from the main jet ahead of the jet's transition to turbulent flow. The flow conditions that caused this phenomenon were found to be directly related to the flow's Reynolds and Grashof numbers, and when these values were plotted, this mixing behavior was shown to be most likely to occur above certain thresholds of these two non-dimensional parameters [19].

Other studies have been accomplished that have examined the mixing behavior of buoyant jets, only this time issuing vertically into an ambient fluid. The research presented in [20] studied the far field mixing structure of liquid buoyant jets with LIF, and provided many different interesting illustrations of how this type of flow mixes into the ambient environment. The study presented in [21] dealt with the mixing behavior of turbulent buoyant jets using planar laser imaging. They concluded that the buoyancy of the jet possibly reduced its entrainment with the ambient environment as evidenced by weaker jet centerline mole fraction fluctuations than typically seen with non-buoyant jets [21]. Based on this research, one might expect a non-buoyant jet to have better mixing characteristics than its buoyant counterpart.

Another interesting flow phenomenon is the formation of side jets, or lobes, that entrain the surrounding fluid. Side jets, which are strong ejections of jet fluid into the surroundings, were noted in [22] and were attributed to the generation of strongly coupled pairs of longitudinal vortices in the developing shear layer of the flow. The formation of side jets is further documented in [23] where the authors examined forced cold jets and self-excited hot jets. They concluded that the formation of side jets is not caused by some fundamentally new mechanism, but instead is a consequence of streamwise vorticity becoming so strong that the side jets appear, and thus engulf no external fluid into the jet. These side jets, along with another phenomenon referred to as helical mode excitation, are documented in [24], which also shows excellent photographs of this phenomenon from many different transverse views of the jet flow.

2.6 Summary

Buoyant jets with large density gradients are difficult at best to seed uniformly, and thus are best studied using molecular-based measurement approaches that do not require flow field

seeding. Filtered Rayleigh Scattering is one such method, and uses a source of illumination such as a laser, a molecular absorption filter to block unwanted background and particle reflections, and an imaging device to explore the different flow field characteristics. This method has been used to study various types of flow conditions, and in this document is used to study the formation of side jets in a horizontal buoyant flow field.

The formation of side jets is not a new phenomenon, and has not been found to be caused by any type of new, undocumented mechanism, but their study has been found to be limited in the research examined. This document is intended to add additional information to this interesting phenomenon in hopes of providing additional understanding about the fundamental causes of this behavior.

3. Methodology

3.1 Chapter Overview

This chapter describes the equipment and procedures used to collect data during the Filtered Rayleigh Scattering experiments performed. The first portion of this chapter is dedicated to the description of the equipment used in the FRS experiments starting with the laser system and continuing all the way to the compressed air sources used in the flow field. The second portion is dedicated to describing how these pieces of equipment are used in two different experimental setups. These two experimental setups are used to perform a total of four different experiments, and the third portion of this chapter details the methodology for each of these experiments.

3.2 Experimental Equipment

Filtered Rayleigh Scattering at its most fundamental requires a source of illumination, an atomic/molecular filter, and an image capturing device. For this experiment, a continuous wave (CW) laser is used for illumination, an iodine filter is used for background light absorption, and a digital camera is used to capture the images. These items, as well as other supporting equipment, are described in the following sub-sections.

3.2.1 Laser

The laser used throughout this experiment is a Coherent INNOVA® Sabre™ R Series Argon Ion Laser. The laser, as well as all other optics, are held stable on a 48 ft² optics table manufactured by ThorLabs. The laser itself consists of the laser head, a power supply, a remote

control key pad, and a heat exchanger [25]. All of these items are depicted in the following figure:

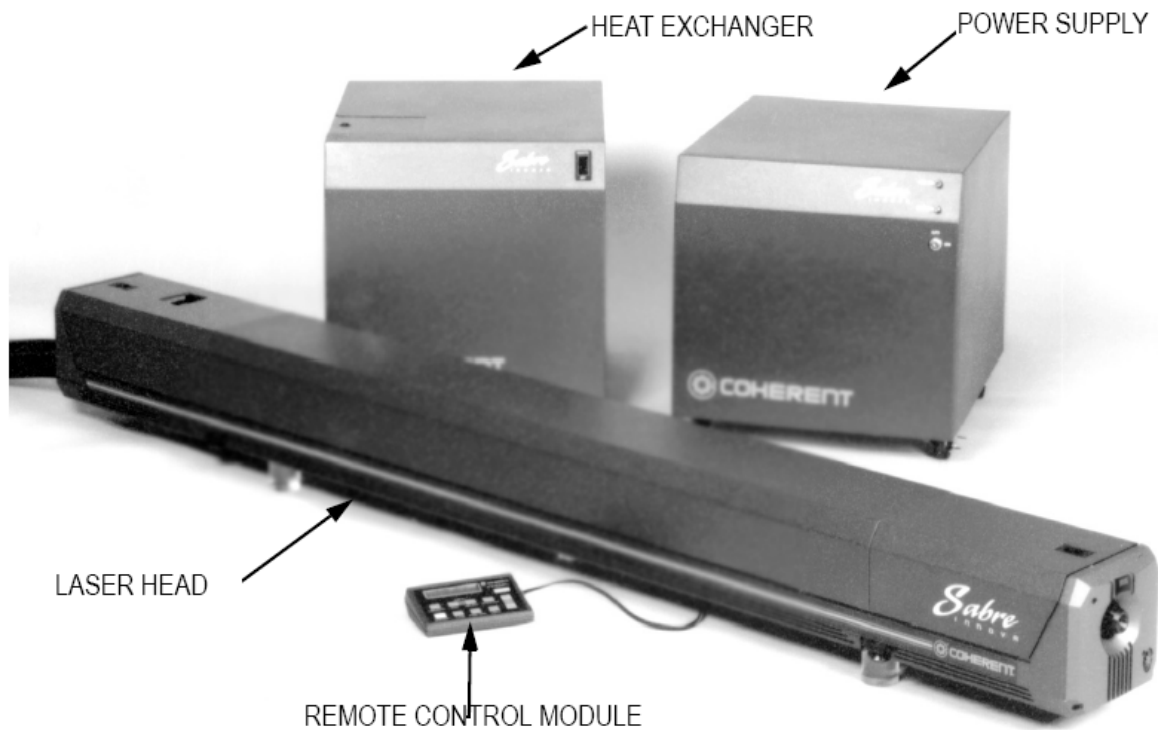


Figure 5. The Coherent INNOVA® Sabre™ R Series Argon Ion Laser's heat exchanger, power supply, laser head, and remote control key pad [25].

The laser system receives its required cooling supply from the building's ethylene glycol cooling system, and its power is supplied by a 480 Volt, 3 phase power supply rated up to 70 amps.

Figure 6 on the following page is a simple diagram of how everything is connected:

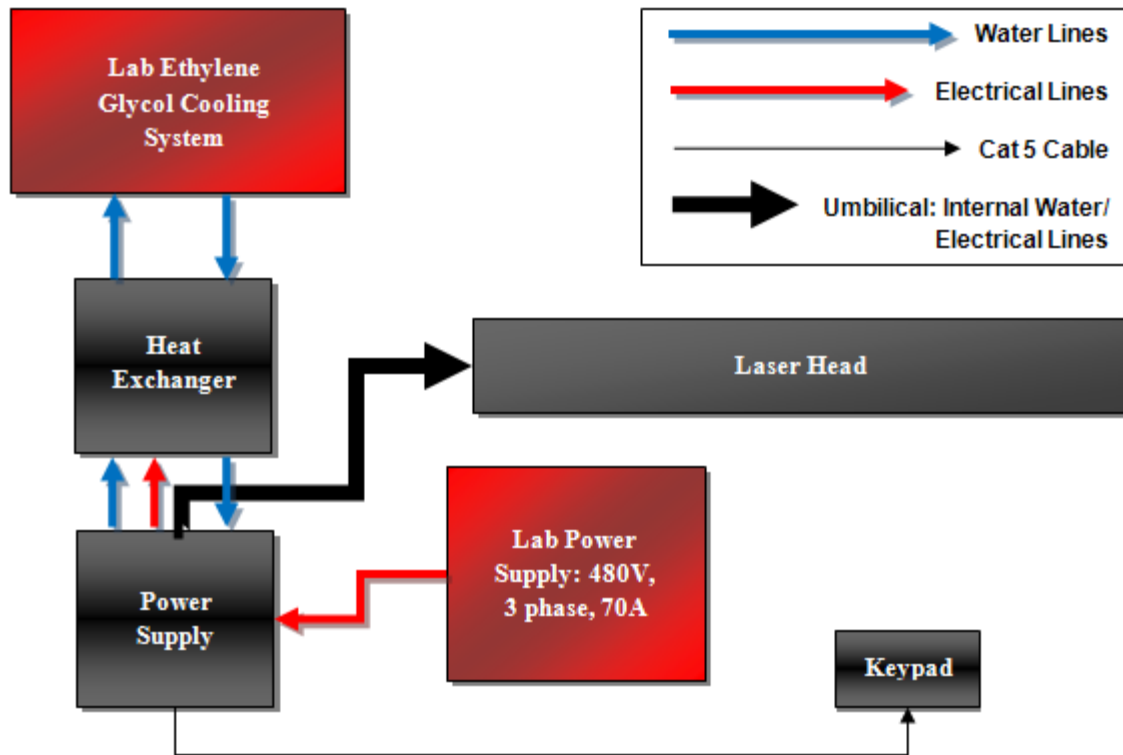


Figure 6. Diagram showing how each of the components of the Coherent laser system are connected during operation.

Coherent, Inc. offers many different configurations for this particular series of laser, and the configuration selected for this experiment is the Argon Tunable Sealed Mirror (TSM) System, identified by the Coherent part number TSM-15. According to the manufacturer's specifications, this laser can produce wavelengths between 454.5-514.5 nm, and can be set by adjusting the etalon temperature [25]. The laser's maximum output occurs at a wavelength of 514.5 nm, and is dependent on the laser's mode of operation; in multiline mode, the rated power output is 7.0 Watts, and in single frequency operation, the rated output drops to 4.2 W [25]. The instantaneous system power output is displayed on the keypad's main menu throughout the laser's operation.

According to the manufacturer's specifications, the laser system requires a warm-up period of approximately 10 minutes before the system has fully stabilized [25]. This warm-up period is marked by a noticeable loss in power when compared to normal operation, and in practice, the warm-up period required is on the order of three to four hours in order for the system to reach its maximum power output and stability.

For the purposes of this experiment, the laser is used in its single frequency mode due to the necessity of maintaining the laser's wavelength in the iodine filter's absorption notch. In order to control the laser's inherent frequency drift during single frequency operation, Coherent has included the v-Track feature. This feature is an active stabilization loop that adjusts the internal cavity length to track the drift in etalon temperature, keeping the laser from mode-hopping [25]. The frequency drift is then a direct function of the etalon temperature stability, and is continuously monitored by the system [25]. Unfortunately, the laser system cannot provide a direct measurement of the beam's wavelength, so a wavelength meter is required to verify its stability, and is described later in this chapter.

3.2.2 Iodine Filter

The iodine filters used in this research have a simplicity that belies their importance in Filtered Rayleigh Scattering. Their construction consists of a cylindrical aluminum outer housing that provides durability, allows for easy mounting on an optics table, and also contains a 3.5 inch diameter glass tube that is filled with the iodine gas. The filters used are manufactured by Innovative Scientific Solutions Inc. (ISSI) of Dayton, OH, and Figure 7 on the next page shows one of the two filters provided for this experiment:

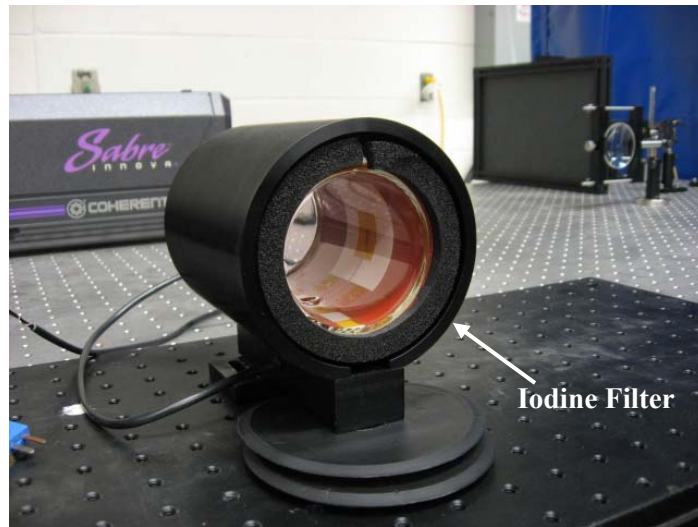


Figure 7. Innovative Scientific Solutions Inc. iodine filter.

There are two cords that exit the base of the aluminum housing; one provides power to the internal heating element and the other is from the internal thermocouple. These plugs are shown below in Figure 8:

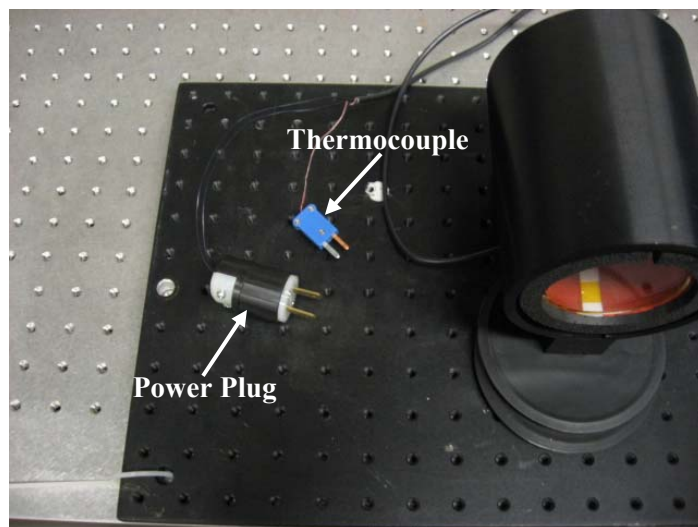


Figure 8. The iodine filter's two plugs. The power plug is a standard 120V, polarized, two-prong plug, and the thermocouple (light blue) is a type K, two blade miniature plug.

The two plugs connect into the back of a Cole-Parmer Digi-Sense temperature controller, shown in Figure 9 below:

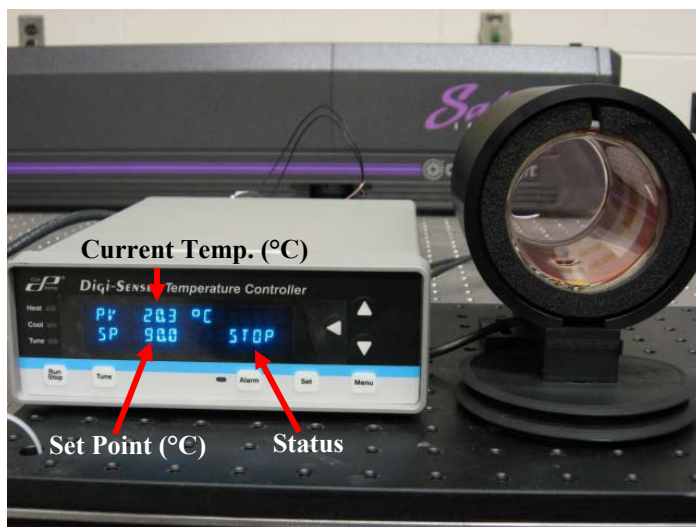


Figure 9. Cole-Parmer Digi-Sense temperature control box, showing a current iodine cell internal temperature of 20.3 °C, a set point of 90.0 °C, and currently not heating the cell.

The two iodine filters tested during the filter characterization described later in this chapter are identical in appearance, but differ in the amount of iodine contained within the glass cell. This difference is important, especially when determining a filter's suitability for FRS measurements. It is also important to note that the iodine filters used in this research are used for background suppression only and not for distinguishing Doppler effects.

3.2.3 Cameras

Two different camera systems are evaluated for their effectiveness in the FRS setup. The first is a high resolution Cooke Corporation PCO.4000 camera system, and the second is a high speed Photron FastCam. Each of these systems is described in detail on the following pages.

3.2.3.1 Cooke Corporation PCO.4000

The PCO.4000 camera manufactured by the Cooke Corporation is a 4008 x 2672 pixel high resolution camera system designed for use in particle image velocimetry, laser induced fluorescence (LIF), and high resolution microscopy experiments among other applications [26]. The particular model used features a thermo-electrically cooled monochrome charge-coupled device and image memory within the camera itself, allowing a frequency sampling rate of up to 80 Hz according to the manufacturer [26]. The camera binning can be set from 1x1 to 2x8, thus allowing the user to manually set the camera's resolution based on application [26]. The camera is fitted with a Nikon 85 mm, 1:2.8 D AF Micro-Nikkor lens, and is shown in Figure 10 below attached to an optics plate:



Figure 10. The Cooke Corporation PCO.4000 camera fitted with the Nikon Micro-Nikkor 85mm lens.

The camera and lens are placed behind the 3” spherical lens and iodine filter during the FRS experiments, all of which are mounted to a single optics plate to allow for ease of movement between experiments. This setup is shown in Figure 11 below:

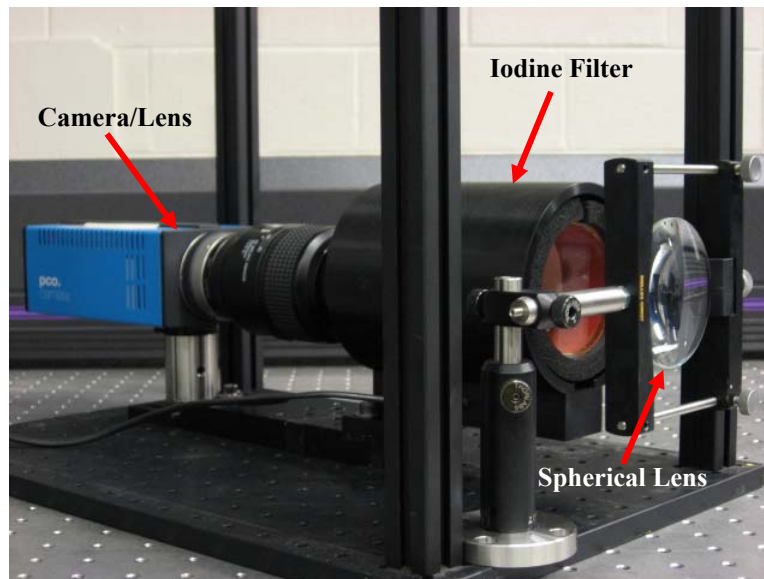


Figure 11. The camera, 85mm lens, iodine filter, and spherical lens as used during FRS experiments.

3.2.3.2 *Photron FastCam*

The Photron FastCam-X 1280 PCI camera system is a high speed camera system that gives up overall image resolution for speed when compared to the PCO.4000 system described previously. It can take full resolution images of up to 1280 x 1024 pixels at up to 500 frames per second (FPS), or 1280 x 512 pixels and lower resolutions at up to 1000 FPS [27]. This camera is pictured on the following page in Figure 12:



Figure 12. The Photron FastCam-X 1280 PCI camera system used for high speed imaging. The camera is fitted with an optional, smaller lens that was not used during testing.

The FastCam was fitted with the same 85 mm Micro-Nikkor lens used on the PCO.4000 camera and tested for suitability of use with the FRS system. Unfortunately, it proved to be unsatisfactory in this particular application. The camera system simply could not gather enough light to produce discernable images during the FRS experiments, and therefore the decision was made to use the PCO.4000 camera and trade off high speed photography for higher quality images.

3.2.4 Wavelength Meter

A Bristol Model 621A Laser Wavelength Meter is used during the experiments to verify the laser beam wavelength. The device is simple in appearance and operation, and its two main parts are shown in Figure 13 on the following page:

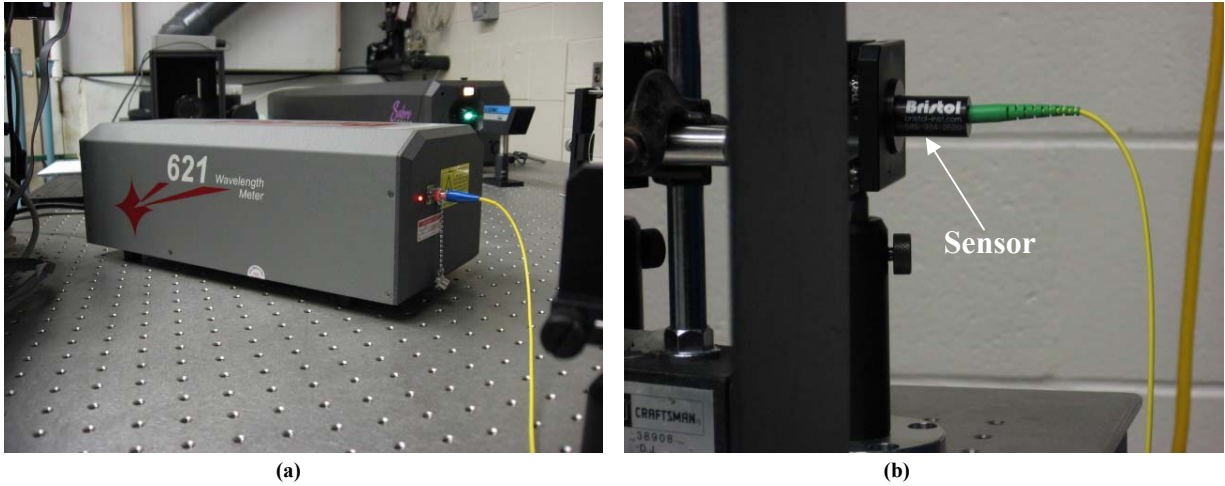


Figure 13. The Bristol Model 621 Laser Wavelength Meter. The picture on the left (a) shows the main processing unit and where the fiber optic cable (yellow) from the sensor is connected. The picture on the right (b) shows the sensor itself mounted in a ThorLabs two-adjuster mirror mount.

The main processing unit for the wavelength meter connects to any computer via USB, and the included software displays the real-time laser wavelength and input power, as can be seen in Figure 14 below:

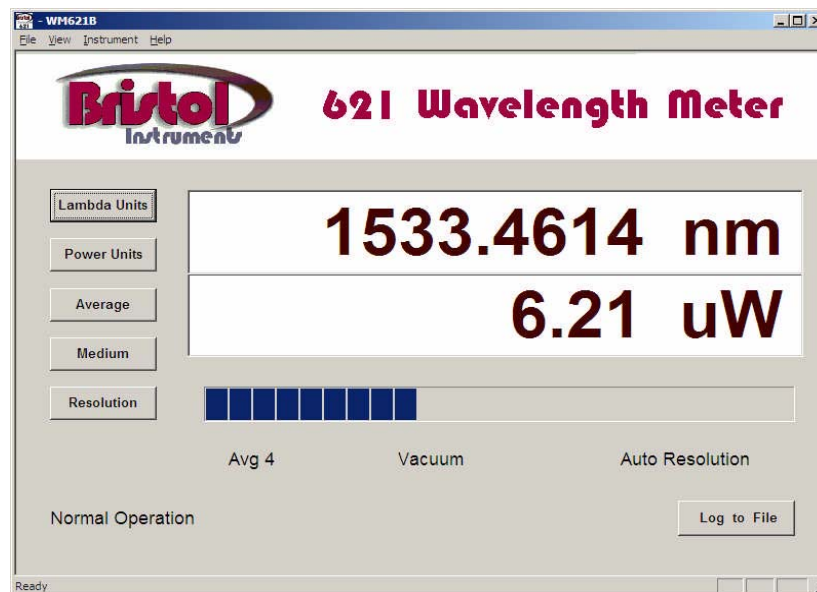


Figure 14. Sample screen shot from the Bristol Instruments software, indicating a current laser wavelength of 1533.4614 nanometers, and an input power of 6.21 microWatts as measured in a vacuum [28].

The wavelength meter sensor's maximum acceptable input power is 10 mW [28]. When using the Argon Ion laser listed above, even the laser's lowest power setting can easily overpower the sensor, and thus cause damage. It is therefore necessary to use a series of beam samplers in order to reduce the incident beam's power enough to stay under the 10 mW maximum threshold, but still above the 1 μ W minimum input required [28]. Beam samplers will be discussed later in this chapter.

The most difficult part of using the Bristol Wavelength Meter involves aligning the sensor so that the laser beam's light can travel through the fiber optic cable without impediment. While it seems that a simple point-and-shoot methodology would suffice, this process actually requires great care, as the smallest of adjustments can mean the difference between the machine being able to read the wavelength and showing no output at all. The ability to make fine adjustments necessitates the use of a ThorLabs two-adjuster mirror mount to hold the sensor, as was shown in Figure 13 (b) previously. The operator's manual suggests an alignment method shown in Figure 15 on the following page:

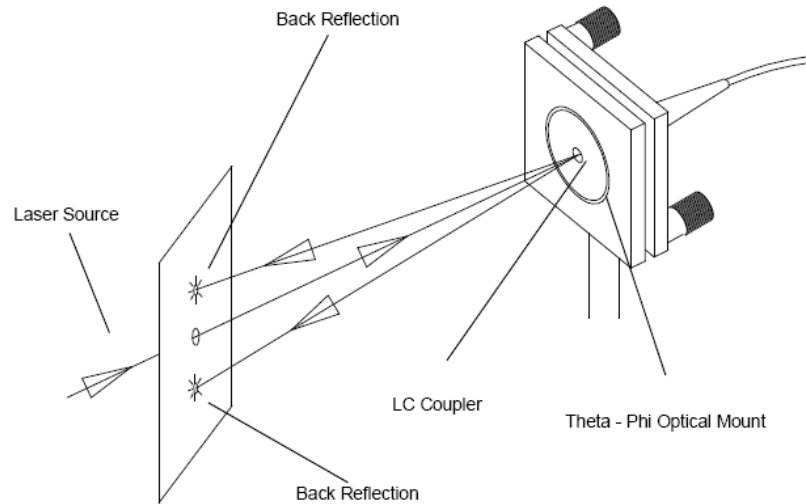


Figure 15. The Bristol Instruments suggested method for aligning the wavelength meter's optical sensor. This method involves using a note card with a hole in the center, allowing the laser source to pass through while giving a surface to display the back reflections generated by the optical sensor. The ideal alignment will produce back reflections that symmetrically straddle the hole [28].

The alignment method in Figure 15 involves watching the location of the back reflections and also watching the software's power output display on the computer monitor while making small adjustments to the optical mount until maximum input power is achieved. This method proved to be tedious at best, and yielded less than ideal results. In order to speed up the process, a new alignment procedure was developed.

Since the optical sensor uses a fiber optic cable, the light coming in through the sensor is observable at the other end of the cable that connects to the main processing unit. Removing this connection and pointing it at a simple business card while adjusting the optical mount allows the user to easily see whether or not the adjustments being made are producing more or less light.

Figure 16 on the following page shows this method in detail:

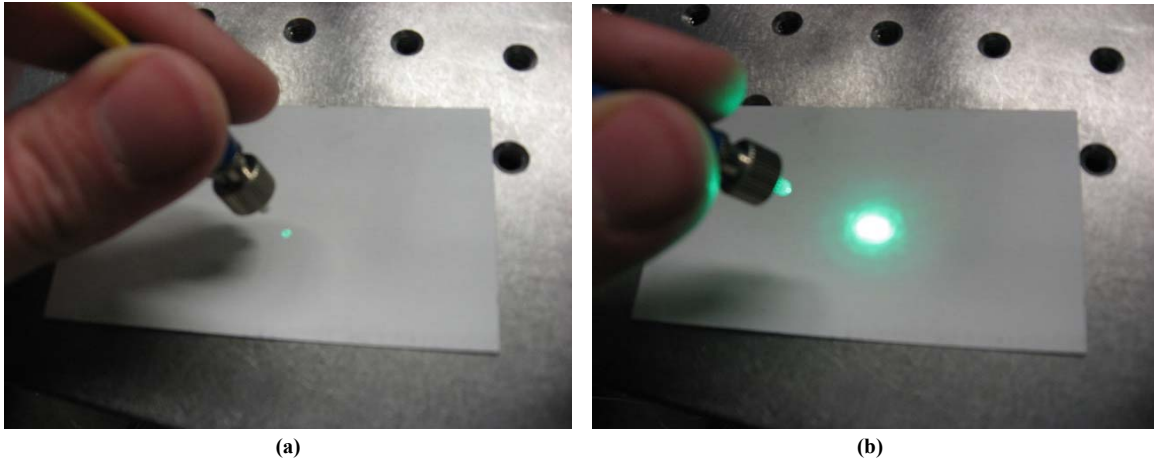


Figure 16. Alternate alignment method for the Bristol Wavelength Meter. The fiber optic cable (yellow) is removed from the processor and pointed at a business card. The picture on the left (a) shows the result of an improperly aligned sensor; the processor cannot read a signal of this intensity. The picture on the right (b) shows the intensity of laser light through a properly aligned sensor; the power reading is approximately 2.7 mW.

Once the fiber optic cable shows a similar output to what is seen in Figure 16 (b), the alignment process is complete. The fiber optic cable can then be plugged back in to the main processing unit, and the software will then show the correct wavelength and input power. The wavelength displayed is accurate to ± 0.0002 nm @ 1,000 nm, and the power displayed is accurate to $\pm 15\%$ [28].

3.2.5 Power Meter

A Coherent Fieldmaster power meter is used to measure the laser beam's output power during some experiments. This meter includes an automatic resolution display and the sensor, shown in Figure 17 on the next page:



Figure 17. Coherent Fieldmaster power meter display on the left and the sensor on the right. The 7 nanoWatt reading displayed is a result of the ambient lighting conditions in the laboratory (no flash used in photograph).

This particular power meter has a rated accuracy of $\pm 2\%$ [29], and as can be seen in Figure 17, great care must be taken to ensure that the ambient lighting conditions are taken into account before using it to measure the power of another light source.

3.2.6 *ThorLabs Optics*

Three types of optics manufactured by ThorLabs are used throughout these experiments, including spherical lenses, beam samplers, and mirrors. Each device is described individually in the following sub-sections.

3.2.6.1 LMR2 lens mount with Spherical Lens

The ThorLabs LMR2 fixed optic mount holds a 2" diameter spherical lens, and maintains its affordability by giving up ease of adjustment [30]. These lenses can be used to both expand and refocus the incident laser beam when used in pairs, and are used in such a manner during the iodine filter characterization discussed later in this chapter.

3.2.6.2 BSF10-A1 Beam Sampler

The ThorLabs BSF10-A1 Beam Sampler uses Fresnel reflections to pick-off between 1% and 10% of the incident beam at 45°, dependent on polarization [31]. This particular model is a 1" diameter, 5 mm thick, UV fused silica sampler that is designed to be used with an incident beam wavelength of between 400-700 nm [31]. All beam samplers used are mounted in ThorLabs two-adjuster mirror mounts to allow for fine adjustment.

3.2.6.3 PF10-03-G01 Protected Aluminum Mirror

The PF10-03-G01 protected aluminum mirror is designed for general broadband use, and features a Silicon Monoxide (SiO) coating that protects the aluminum from the incident beam [32]. All mirrors used are mounted in ThorLabs two-adjuster mirror mounts.

3.2.7 Other Optics

Certain aspects of the experiments require different types of optics including cylindrical and spherical lenses. The particular lenses used are described in the next sub-sections.

3.2.7.1 *Cylindrical Lens*

A small cylindrical lens is used during portions of the experiments to take the narrow incident beam line from the laser and spread it into a sheet of light. The actual cylindrical lens used is shown in its mount in Figure 18 below:



Figure 18. Cylindrical lens and mount used to spread single laser beam line into a sheet of light.

3.2.7.2 *Spherical Lens*

A 3 inch diameter spherical lens is mounted in front of the camera lens during the FRS experiments to serve a two-fold purpose. First, it acts as a magnifying glass to enlarge the area of interest where the helium flow crosses the laser beam, and second, it helps to gather as much light as possible to enhance the signal that the camera receives. The spherical lens used is shown in Figure 19 on the following page:



Figure 19. Spherical lens and mount used in front of camera to magnify the region of interest and gather as much light as possible.

3.2.8 *Aperture*

An unfortunate byproduct of the ThorLabs BSF10-A1 beam sampler is the creation of multiple beams once the incident beam has passed through the initial beam sampler. These other beams are lower in intensity when compared to the reflected beam of interest, but these can still pose problems with unwanted stray reflections. In order to keep these stray reflections to a minimum, a small mechanical aperture can be used to allow only the beam of interest to pass through uninterrupted, while the other multiple beams are stopped from further propagation. Figure 20 on the following page shows the mechanical aperture used, and provides a good example of the multiple beams produced by the beam samplers:

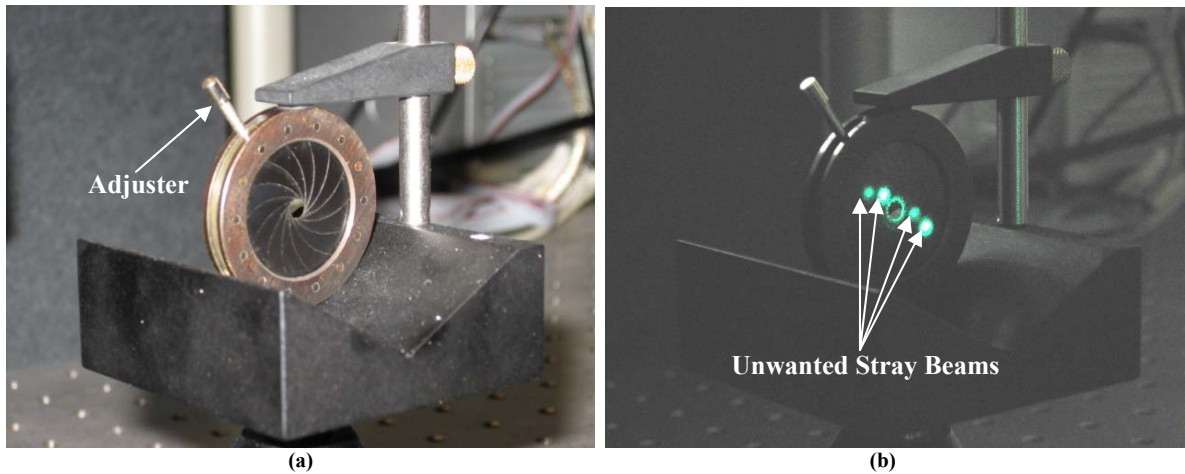


Figure 20. The mechanical aperture used in different parts of the experiments. The picture on the left (a) is a detailed view of the aperture, and the picture on the right (b) clearly shows the multiple beams that is has stopped from propagating further while still allowing the most intense to pass through unimpeded.

3.2.9 *Beam Trap*

Scattered laser beam energy can cause two major problems during FRS experiments performed with the Coherent laser system. First, the scattered beam can reflect off many different surfaces, including walls and the optics table, and unless adequate eye protection is worn at all times by all personnel within the same room as the operating laser, the reflected beams can cause permanent eye damage. Secondly, the scattered light can be reflected directly into the camera lens, thus increasing the background noise compared to the signal of interest. The iodine filter helps eliminate some of this backscattering, but the use of a Blue Sky Research Model 500 beam trap after the beam has traveled past the flow field eliminates almost all of the backscattering. This device, shown in Figure 21 on the next page, simply absorbs the laser energy that enters the device:

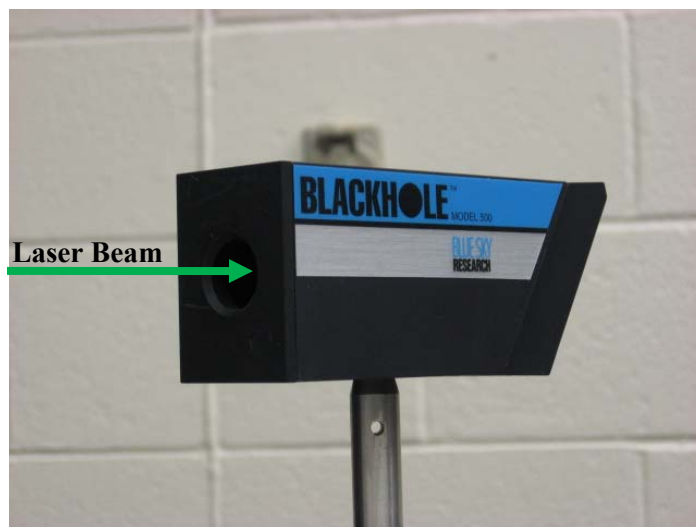


Figure 21. The Blue Sky Research Black Hole beam trap, shown with a simulated laser beam entering the device.

3.2.10 Flow Controllers

There are two brands of mass flow controllers available for this experiment including the Alicat Scientific model number MCR-1500SLPM-D and the Brooks model number 5850i. As the Alicat's model number indicates, it is capable of flowing up to 1500 standard liters per minute (SLPM) of gas, and has an advertised accuracy of $\pm 0.8\%$ of the indicated reading on its display and $\pm 0.2\%$ of its 1500 SLPM full scale mass flow rating [33]. Its user interface is compact in design, and is incorporated into the flow controller itself, thus making for a relatively small overall package. As with any measurement device, the Alicat gives up the ability to make small adjustments to the mass flow for the ability to flow a large amount of gas; it can only be adjusted to ± 1 SLPM. The Alicat's main advantages are its compact design and its ability to internally adjust for 30 different types of gas with the push of a few buttons [33]. This mass flow controller is pictured on the next page in Figure 22:



Figure 22. Alicat Scientific model number MCR-1500SLPM-D mass flow controller. The gas flows from left to right as pictured.

The Brooks 5850i mass flow controller has an advertised accuracy of $\pm 1\%$ of its rated full scale flow rate, and comes calibrated from the factory for only one type of gas [34]. The single gas calibration combined with the bulky user interface puts the Brooks mass flow controller at a distinct disadvantage to the Alicat model, but due to the flow rates of the Brooks controllers available for this research, they could be adjusted to ± 0.1 SLPM, providing a much finer adjustment when compared to the Alicat unit available for testing. The two Brooks flow controllers are calibrated for different gases and flow rates; the first is calibrated for methane (CH_4) and a full scale flow rate of 3 SLPM, and the second is calibrated for air and a full scale flow rate of 30 SLPM. The Brooks flow controllers are pictured in Figure 23 on the following page:

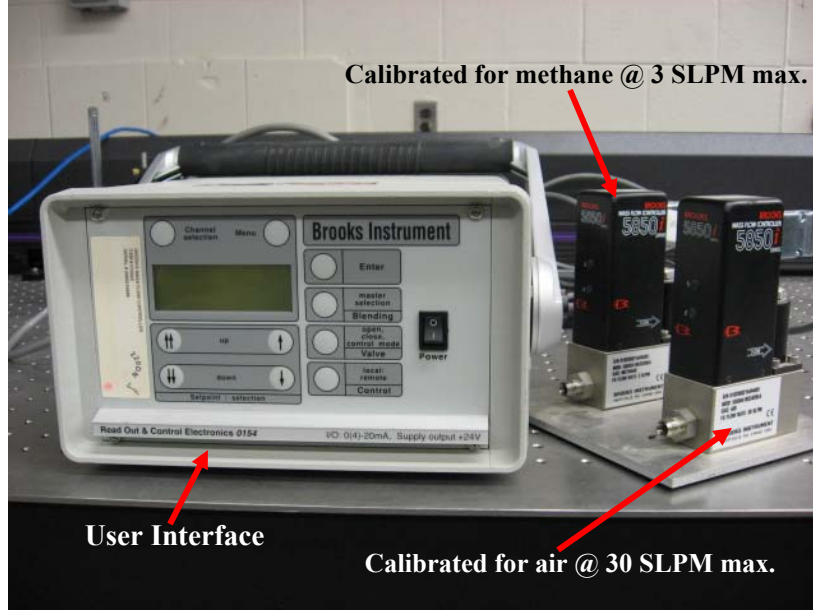


Figure 23. The Brooks Instrument 5850i mass flow controllers. The user interface box can control both units at the same time.

The Brooks mass flow controllers are calibrated for different gases than their intended use during the FRS experiments, and thus require a conversion factor in order to ensure that the user interface's readings correlate to the desired flow rate of the actual gases used. The Brooks unit calibrated for methane at a maximum flow rate of 3 SLPM is used to flow small amounts of nitrogen (N_2) during the experiments as a co-flow with the helium, and the unit calibrated for air at a maximum flow rate of 30 SLPM is used to flow the helium (He). The following equation is used to correlate the flow rate of methane to nitrogen as well as air to helium:

$$Q_{AG} = Q_I \times \left[\frac{\eta_{cg}}{\eta_{ag}} \right] \quad (3)$$

where Q_{AG} is the flow rate of the alternate gas in SLPM, Q_I is the flow rate indicated by the user interface in SLPM, η_{cg} is the absolute viscosity of the calibrated gas, and η_{ag} is the

absolute viscosity of the alternate gas [35]. This equation requires viscosity values for all of the gases involved, and these are provided in Table 1 below:

Table 1. Absolute viscosity (η) values at 25°C for air, helium, methane, and nitrogen [35].

Gas	Absolute Viscosity (η) @ 25°C
Air	184.918
Helium (He)	198.457
Methane (CH ₄)	111.852
Nitrogen (N ₂)	178.120

These values, combined with Eq. (1), yield two equations required during the FRS experiments to calibrate the Brooks mass flow controllers. Equation (4) below converts the indicated flow rate of methane to the actual flow rate of nitrogen for the first flow controller:

$$Q_{N_2} = 0.62796 \times Q_{CH_4} \quad (4)$$

where Q_{N_2} is the actual flow rate of nitrogen and Q_{CH_4} is the indicated flow rate of methane, both in SLPM. Similarly, Eq. (5) converts the indicated flow rate of air to the actual flow rate of helium for the second flow controller:

$$Q_{He} = 0.93178 \times Q_{air} \quad (5)$$

where Q_{He} is the actual flow rate of helium and Q_{air} is the indicated flow rate of air. This ultimately allows the use of nitrogen through a flow controller that was originally calibrated for methane, and helium through a flow controller that was originally calibrated to flow air.

3.2.11 Compressed Gas

The nitrogen co-flow and helium gases used in the flow field box are supplied by two separate tanks shown in Figure 24:

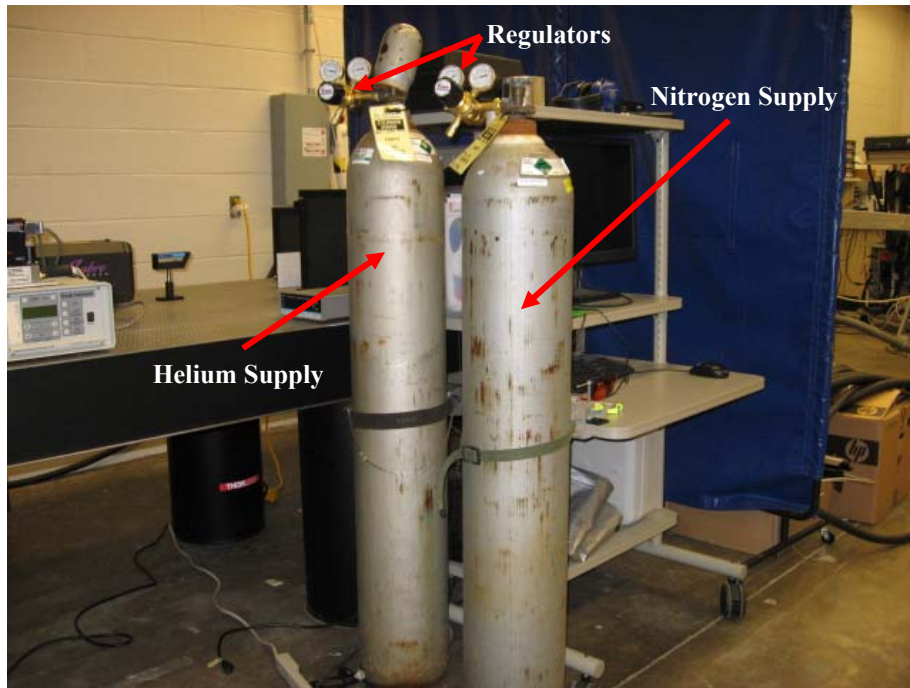


Figure 24. Compressed helium and nitrogen tanks and regulators used to supply the flow field box.

The compressed helium and nitrogen are both ultra-high purity gases, eliminating any possibility of injecting unwanted particles into the flow field. The nitrogen tank is fitted with a Concoa 0-100 psi regulator, and the helium tank is fitted with a Concoa 0-30 psi regulator. The regulators are connected to their respective mass flow controllers with 0.25 in. flexible plastic tubing and various brass Swagelok® tubing adapters and ferrules.

3.2.12 Traverse

In order to gather helium concentration data during the FRS experiments, the helium stream must intersect the laser beam in front of the camera system used. The PCO.4000 camera system shown in Fig. 11 is easily maneuverable, but the laser head, weighing in at 240 lbs. [1], is not. Therefore, it is necessary to be able to move the helium stream both vertically and horizontally to be able to place the stream so that it intersects the laser beam properly at different flow rates. This maneuverability is accomplished using a combination of a horizontal traverse and a scissor jack shown in Figure 25 below:

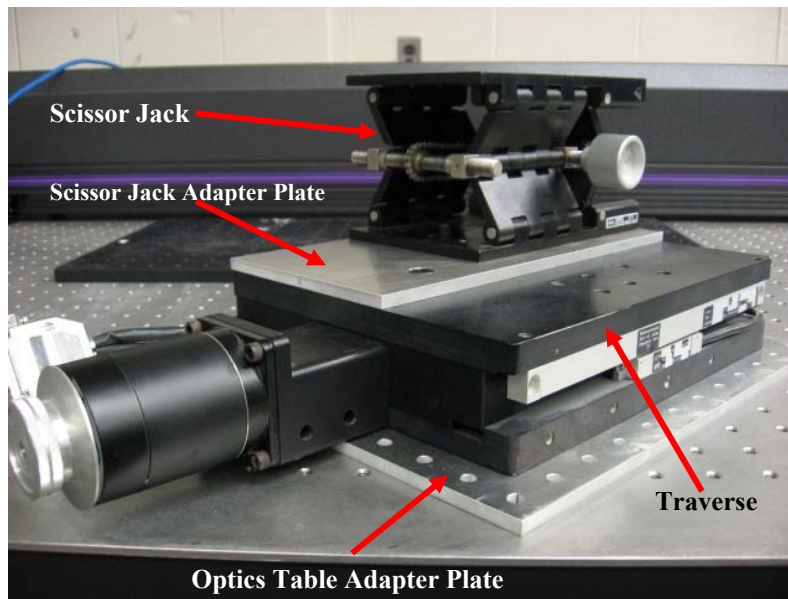
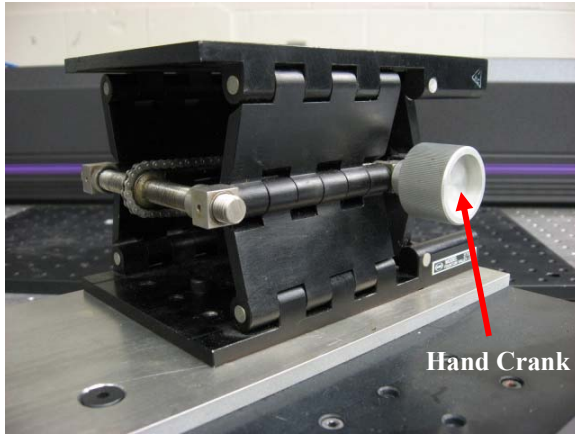
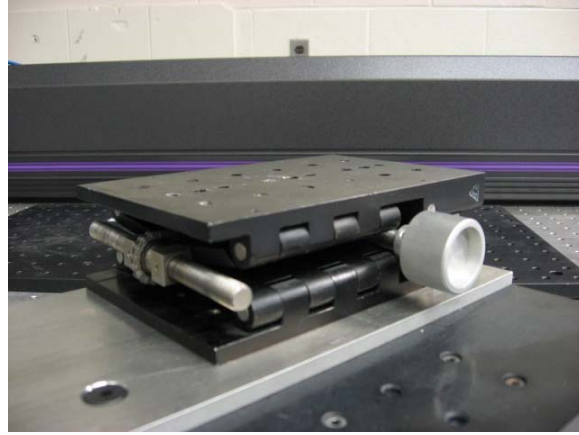


Figure 25. The traverse and scissor jack are shown as attached to their respective adapter plates.

The bottom of the traverse is mounted to a $\frac{1}{4}$ -in. thick aluminum adapter plate with holes drilled 1 in. apart on-center to match the hole pattern of the optics table, and the scissor jack is connected to the top of the traverse with another $\frac{1}{4}$ -in. thick aluminum adapter plate. The scissor jack allows for 2.25 in. of vertical movement, and the traverse allows for 2.30445 in. of horizontal movement. The scissor jack's range of movement is shown in Figure 26:



(a)



(b)

Figure 26. The scissor jack's full range of motion of 2.25 in. The picture on the left (a) shows full extension, and the picture on the right (b) shows full compression.

The advantage to using the traverse pictured in Fig. 25 is the ability to automate its operation. The traverse can be connected to an Anilam Wizard 150 power supply and digital readout, allowing the user to control fore and aft motion with a joystick in increments of 0.00005 in. This entire setup is shown on the next page in Figure 27:

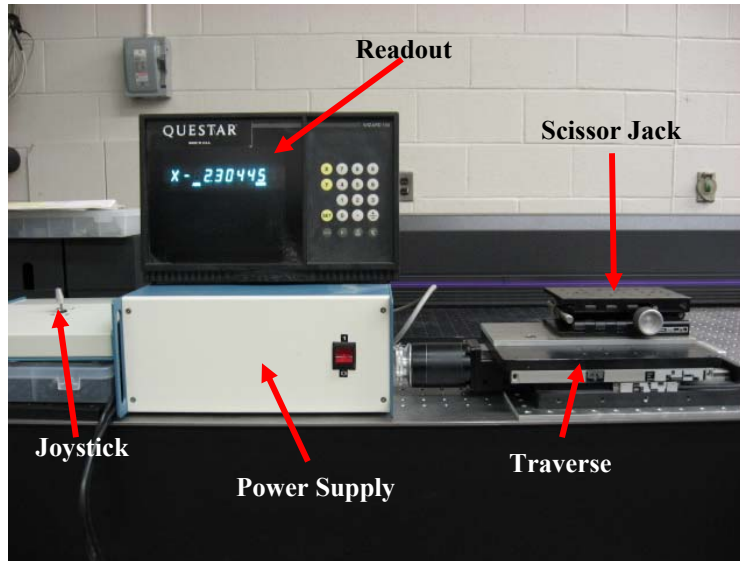


Figure 27. The Anilam Wizard 150 power supply, joystick, and digital readout as connected to the traverse and scissor jack setup shown previously in Fig. 20. Note the display showing the maximum horizontal range of motion of 2.30445 inches.

Unfortunately, only the horizontal direction can be automated; vertical adjustments must still be made by turning the hand crank shown in Fig. 26 (a) and (b).

3.2.13 Flow Field Box

The previous FRS research effort at AFIT used a very simple apparatus to direct the buoyant helium jet of interest as well as a co-flow of air to help control the amount of small particles that crossed through the laser beam. This device was effective, but had only one size tube (0.25" inner diameter) that could not easily be changed to a different size. The helium tube had a 90° bend upstream of the exit, which is shown in Figure 28 on the following page:

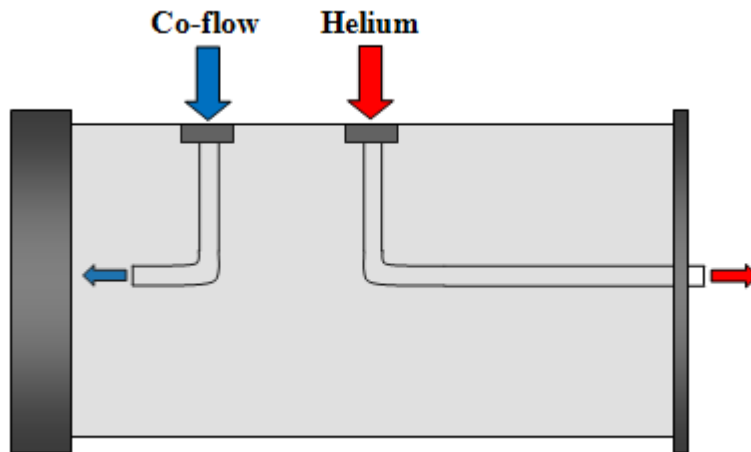


Figure 28. Simple diagram showing the flow field box used in the previous AFIT research effort.

The 90° bend was approximately 20 diameters upstream of the tube exit. It most likely had a negligible effect on the overall quality of the helium flow, but the design could have been better. The desired experiments for this research required the use of multiple sizes of tubes that could quickly and easily be changed, and thus a new flow field device was designed and built.

The design is based around an 8 inch wide by 8 inch high by 14 inch long optical grade Plexiglas box. The sides of the box are bonded together, and it is subsequently bonded to aluminum angle stock that has been formed into a square and serves as a mounting surface for an aluminum plate. An additional piece of one inch thick Plexiglas is drilled with the same one inch on-center hole pattern as the optics table, tapped for ¼”-20 mounting hardware, and bonded to the side of the box. This device can be seen in Figure 29 on the following page:

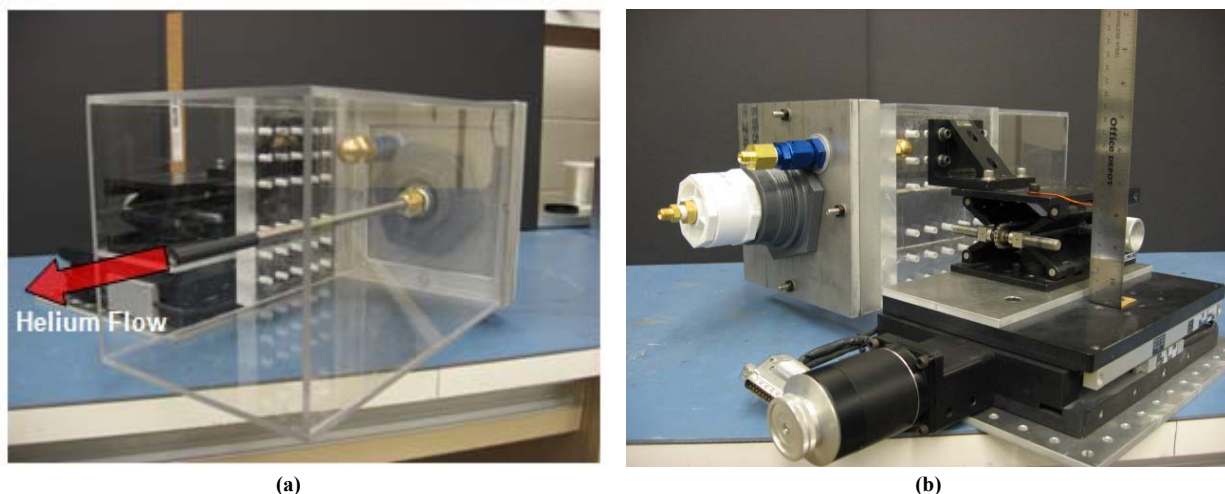


Figure 29. The Plexiglas flow field box fully assembled and mounted to the scissor jack/traverse combination described earlier. The picture on the left (a) shows where the helium exits through the tube, and the picture on the right (b) shows how the box is attached to the scissor jack using a ThorLabs 90° angle bracket.

The 0.375” thick aluminum plate has a 3.25” diameter hole cut out of the center to allow the use of a PVC through-wall fitting and rubber seal, and a smaller 0.625” diameter hole cut approximately 2.83” and 45° from the center of the larger hole. This smaller hole allows the passage of an aluminum -10AN bulkhead fitting and bulkhead nut, and is sealed on each side of the plate with an Earl’s Performance Plumbing Stat-O-Seal combination aluminum crush washer and Viton® o-ring seal. A brass tank washing nozzle is attached to the end of the bulkhead fitting with a -10AN to ½”-NPT adapter, and is used to disperse the nitrogen co-flow in a 240° spray pattern. This plate can be seen in Figure 30 on the following page:

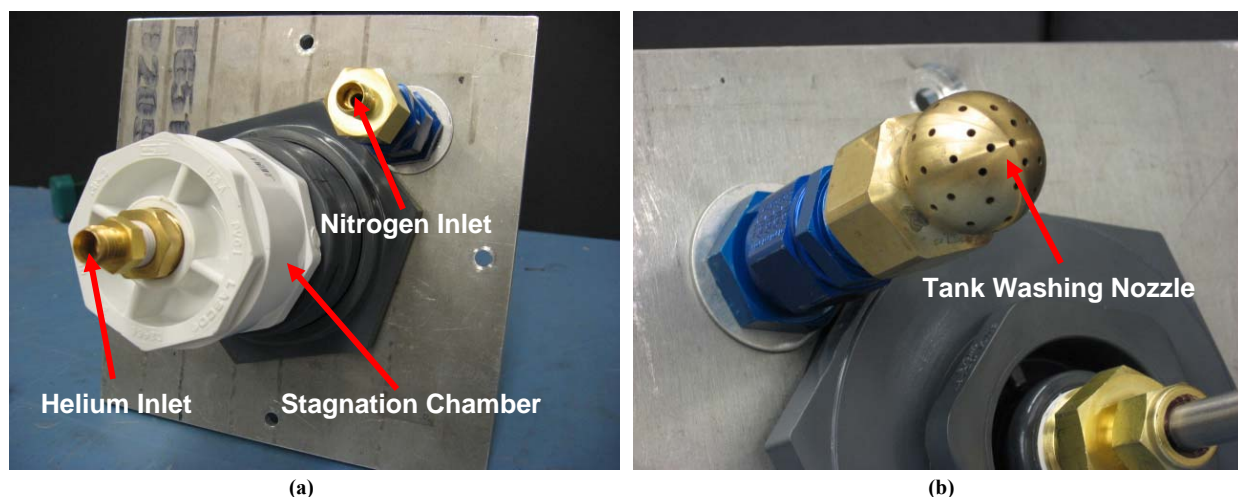


Figure 30. The aluminum plate that attaches to the back of the flow field box, shown assembled with the various fittings and adapters used during testing. The picture on the left (a) shows the back of the plate with the gray PVC through-wall fitting, the white stagnation chamber, and the inlets for the helium and nitrogen. The picture on the right (b) shows the tank washing nozzle that disperses the optional nitrogen co-flow.

A simple stagnation chamber is made from off-the-shelf PVC plumbing, and is screwed into the 2"-NPT through-wall fitting shown in Figure 30 (a). The through-wall fitting and PVC plumbing combine to form a $\sim 15.4 \text{ in}^3$ stagnation chamber so that the helium has a place to dwell before entering the tube attached to the other side of the gray through-wall fitting.

There are seven different sizes of tubes available for testing purposes, and each of these tubes is sealed to the through-wall fitting with various NPT adapters, Swagelok® bored-through tubing adapters and Teflon® ferrules. The Teflon® ferrules allow the tube to seal to the Swagelok® adapters without crimping the tubes, thus allowing them to be slid into and out of the stagnation chamber as necessary to ensure maximum flexibility in placing the helium jet in the desired location. Table 2 on the following page shows the tube sizes available for this research:

Table 2. The outer diameter, inner diameter, and length normalized by the inner diameter for each of the seven tubes available for this experiment. Each tube is approximately 13 inches in length.

#	Tube O.D. (in.)	Tube I.D. (in.)	Length
1	1/8"	0.081	160.5 D
2	1/4"	0.224	58.0 D
3	3/8"	0.306	42.5 D
4	3/8"	0.352	36.9 D
5	1/2"	0.454	28.6 D
6	5/8"	0.575	22.6 D
7	3/4"	0.675	19.3 D

In order to ensure that the helium flow through the tubes is fully developed, the following equation is used to determine the entry length required assuming laminar flow [15]:

$$\frac{L_e}{D} = 0.06 \times Re \quad (6)$$

where L_e is the entry length, D is the tube's inner diameter, and Re is the Reynolds number.

Table 3 below shows the worst case scenarios for the required entry length based off of a predetermined set of test points for the different tubes used during the experiments:

Table 3. The worst case (highest) flow rate conditions for each of the tubes used during this research. The Reynolds number is based off of each tube's inner diameter and the highest flow rate used for that tube. The entry length required is shown in terms of the number of diameters required.

#	Tube O.D. (in.)	Tube I.D. (in.)	Re_{max}	L_e
1	1/8"	0.081	672.2	$40.3 \times D$
2	1/4"	0.224	797.5	$47.9 \times D$
3	3/8"	0.306	597.9	$35.9 \times D$
4	3/8"	0.352	518.0	$31.1 \times D$
5	1/2"	0.454	241.2	$14.5 \times D$

Due to time constraints, only five out of the seven tubes available were used during testing.

Comparing Table 2 to Table 3, it is shown that each of the tubes is sufficiently long for the flow to fully develop under the highest flow rate conditions tested.

The Plexiglas flowfield box was originally designed to allow the tube exit to be positioned before the end of the box, thus keeping all present room currents caused by the laboratory's heating, ventilation, and air conditioning (HVAC) system to a bare minimum immediately surrounding the helium jet. As a result, the laser sheet that illuminated helium jet flow would have to pass through the box itself, hence the use of the optical grade Plexiglas. In reality, this idea did not work as intended. The optical properties of the clear plastic panels were quickly degraded during the assembly process, and thus the laser sheet did not cleanly pass through the box. The laser light scattering drove the signal-to-noise ratio down, and the camera was unable to produce a discernable image of the helium jet. Therefore, it was necessary for the tube exit to occur just outside of the 14 inch long box to keep this light scattering to a minimum.

Additionally, this box was designed for the optional use of a co-flow from a compressed nitrogen bottle, with its mass flow rate manipulated by a second mass flow controller. This co-flow was originally intended to help purge the particles from the field of view, but at a very low velocity so that the helium jet's behavior was not disturbed. After some brief experimentation, the co-flow did not seem to help eliminate any of the particles in the flow field, and it in no way enhanced the image quality. Thus the decision was made to leave the co-flow turned off throughout all of the experiments. This choice helped to simplify the overall problem by eliminating that variable completely. If it had been used, a flow straightening device would have been incorporated in the flow field box to help evenly distribute the co-flow, and is why such a device is not seen in Figure 29 (a).

3.3 Experimental Setups

There are a total of two different experimental setups that are used to perform four different experiments. The first setup is unique to the first experiment, and is used to characterize two iodine filters. The second setup is used for each of the final three experiments.

3.3.1 Experimental Setup 1: Iodine Filter Characterization

The experimental setup used to characterize the iodine filter is best described with a simple diagram, shown below in Figure 31:

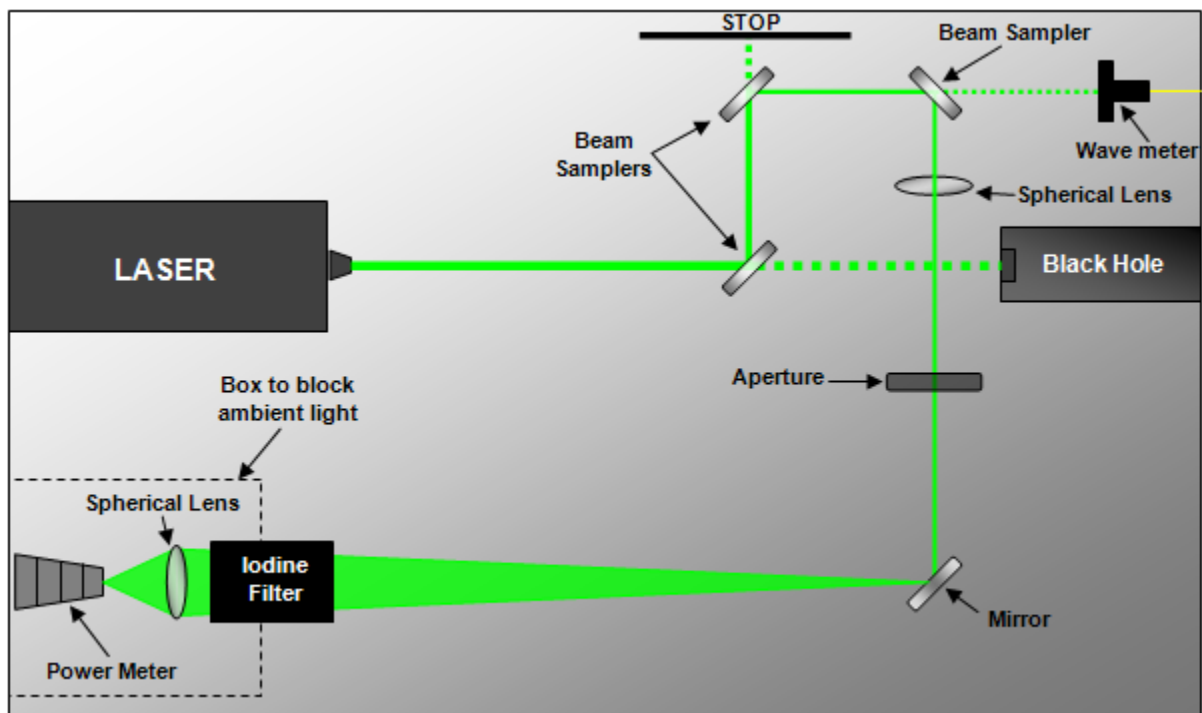


Figure 31. Diagram showing the overall setup for the first experiment. The incident laser beam passes through three beam samplers, a spherical lens to increase the beam diameter, an aperture to block unwanted multiple beams from the beam samplers, and a mirror to turn the expanding beam 90°. After the beam passes through the iodine filter, it encounters another spherical lens that refocuses the beam back to a pinpoint, and its power is subsequently measured by the power meter.

Although the laser is set to its smallest aperture for this experiment to limit its power output, the incident beam is still too powerful to be sent directly to the wavelength meter (recall the wavelength meter can only handle up to 10 mW of power before damaging the fiber optics) or the iodine filter. Consequently, the beam is sent through a series of beam samplers in order to step down the power of the beam to acceptable levels. The Black Hole beam trap is placed after the first beam sampler to catch the highest intensity non-reflected beam for safety reasons, and the wavelength meter is placed so that it receives enough input power to show a reading, but not enough to destroy the sensor. A spherical lens is placed after the third beam sampler to allow sufficient distance for the beam to spread, and the aperture is placed after that to block the unwanted stray beams produced by the samplers. The laser beam passing through the spherical lens takes a much longer distance to expand than contract, hence the mirror that is used to direct the expanding beam down the length of the table; the optics table is not wide enough to allow adequate expansion of the beam. By the time the beam reaches the iodine filter, it has expanded from a pinpoint to 1.5" in diameter, as shown below in Figure 32:

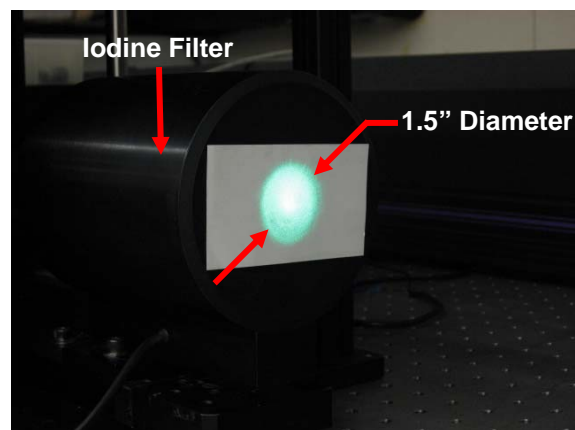


Figure 32. Picture showing the expansion of the laser beam by placing a business card directly in front of the iodine filter.

By expanding the beam, it passes through a larger volume of iodine molecules, thus increasing the effectiveness of the filter while also more closely resembling the actual conditions in which the iodine filter will be exposed since the filter is used to suppress background reflections and not the incident beam itself.

Recall from Figure 17 the power meter's displayed power output from the ambient lighting conditions. Due to the sensitivity of the power meter's sensor, it is placed in a box to limit the amount of ambient light that is allowed to reach it, but the front panel of the box is removed to allow the expanded laser beam to pass. This is shown in Figure 33 below:



Figure 33. Pictures showing the power meter's sensor, spherical lens, and iodine filter mounted in a box with the front panel removed. The picture on the left (a) shows the sensor and the lens without the filter in place, and the picture on the right (b) shows the filter in place and ready for testing.

The box effectively eliminates any power meter readings due to the ambient lighting so that any output displayed is purely a result of the laser beam power that remains after passing through the iodine filter.

3.3.2 Experimental Setup 2: Helium Flow Across Laser Sheet

The second experimental setup is the one used for the vast majority of this research, and is shown below in Figure 34:

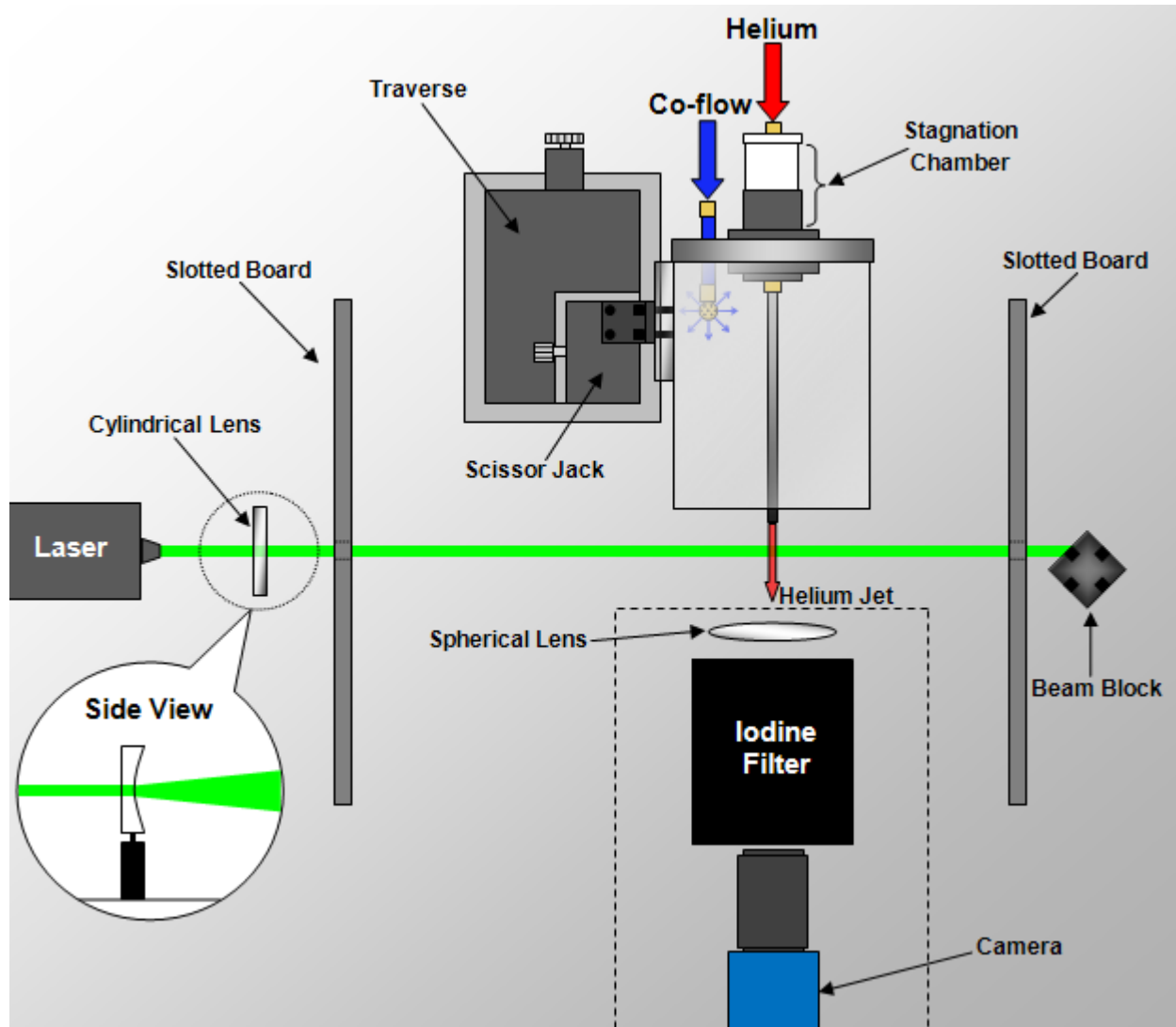


Figure 34. Diagram depicting the second experimental setup. The laser beam is spread into a sheet of light with a cylindrical lens, and passes through a slotted board that keeps background reflections produced by the laser itself to a minimum. The traverse, scissor jack, and flow field box are placed so that the helium jet intersects the laser sheet, and the camera is placed opposite the jet to record the images. The laser sheet passes through one more slotted board and is stopped with a makeshift beam block.

Figure 34 is self-explanatory, but the rationale behind using the slotted boards is not nearly as intuitive. The laser itself produces a great amount of stray light that is emitted along with the incident beam, and this stray light illuminates the optics table as well as any equipment that is attached to it, including the flow field box and the enclosed tubes. Under ideal conditions, the only light detected by the camera would be from the laser sheet itself, and the background would be completely dark. A perfectly dark background is not possible with this setup, and thus there is a great deal of background light that effectively decreases the signal-to-noise ratio. The signal in this case is the laser sheet while the helium flowing across the sheet causes a dark region due to Rayleigh scattering. The iodine filter is designed to eliminate as much of this background scattering as possible, but it cannot eliminate it all. Therefore, it is imperative that any source of stray light be eliminated before it has a chance to propagate. A board with a slot cut in it only slightly wider than the laser beam helps to eliminate the stray light produced by the laser while allowing the incident beam to pass. Figure 35 clearly shows how effective the slotted board is:



Figure 35. Picture showing one of the slotted boards used in the second experimental setup. Note the green glow that the board stops from further propagation while still allowing the incident laser beam to pass.

The laser sheet's width is too large to be captured by the Black Hole beam trap after it has passed the flow field box. Therefore, a beam block made from a slotted piece of black anodized aluminum is used to catch the laser sheet. This beam block is far from ideal, and reflects a great deal of light back towards the flow field box. Consequently, a second slotted board is placed so that the back reflections are kept to a minimum.

Another point of interest in Figure 34 is the box surrounding the 3" spherical lens, iodine filter, and camera. This box is the same that was used in the previous experimental setup (shown in Figure 31), only this time the rear panel is also removed to allow the camera's rear connections to be easily accessed. The side panels keep any reflected laser light from making its way to the camera, thus ensuring the highest signal-to-noise ratio possible.

3.4 Experimental Methodology

Before delving into the experimental results presented in the next chapter, a brief explanation is required that details the methods of experiment chosen as well as a quick description of how the data was generated and displayed that best conveyed the results. The iodine filter characterization experiment methodology is presented first; the second and third experiments used an identical methodology, and are combined into one section. The final section details the methodology that is used in the trajectory experiment.

3.4.1 Iodine Filter Characterization Experiment Methodology

The overall objective of this experiment is to figure out how much laser beam power is transmitted through the iodine filter as the beam's wavelength is systematically changed. In order to determine the amount of light being transmitted through the iodine filter, a power ratio is used that compares the laser's power before entering and after passing through the filter. The

power meter placed after the iodine filter records the power at that location, and the wavelength meter's built in power meter is used to record the laser power prior to the filter as well as the laser's approximate wavelength, which is set by adjusting the etalon temperature. In order to ensure accurate and repeatable results, the wavelength meter is set to display the average of its last 100 recordings, which greatly helps to stabilize the displayed readings since they jump around quite rapidly during the laser's transition to different wavelengths.

3.4.2 Fixed Froude and Reynolds Number Experiment Methodology

The fixed Froude and fixed Reynolds number experiments are based around a set of 21 different data points that are chosen to expose the helium flow to a variety of conditions. By varying the flow rates and tube diameters, the Froude number can be held constant while the Reynolds number is varied, and vice versa. The data point selection is driven by a variety of reasons, but the most compelling factor behind these points is actually related to the mass flow controllers mentioned previously in this chapter.

Two different brands of mass flow controllers were listed earlier, but only one ended up being used for the second, third, and fourth experiments. The previous research effort used the Alicat Scientific 1500 SLPM unit, which sufficed for that particular experiment since it was looking at FRS from a somewhat broader perspective, and found an interesting flow phenomenon that this document explores more in-depth. During the initial planning stages of this research, it was decided that the Reynolds, Froude, and Grashof numbers of the helium flow would need to be manipulated in an organized fashion. The decision was made to perform two different experiments; the first would hold the Froude number constant while varying the Reynolds number, and the second would hold the Reynolds number constant instead. This

method required a fair amount of precision with the selection of the helium flow rates in order to keep the Reynolds and Froude numbers as close to each other as possible while the other parameter was changed. The Alicat mass flow controller only allowed an adjustment of ± 1 SLPM, and this was not fine enough to keep the Reynolds and Froude numbers as consistent as possible. Consequently, the Brooks mass flow controller was chosen. Although it could only flow up to 30 SLPM, the flow rate could be adjusted to ± 0.1 SLPM, thus making it easier to create a list of desired data points that would make for an easy comparison.

This choice of mass flow controllers had a direct impact on the list of data points that was developed to explore the formation of side lobes in low flow rate helium jets. Since the flow rates had to remain under the 30 SLPM upper limit, this limited the range of Reynolds numbers given the available tube sizes. This flow rate limit is also what prompted the use of only the five smallest tubes instead of using all seven that were available. Additionally, it is standard practice to place the tube exit a fixed distance away from the interrogating sheet of laser light normalized by the tube's inner diameter, so a constant value had to be chosen and kept consistent among all 21 data points. Based on previous experience with the type of jet behavior desired, it was decided that all 21 data points would be taken with the helium jet exiting the tube 4 diameters away from the laser sheet.

A possible advantage to using a continuous wave laser is that the data acquisition rate is only limited by the camera equipment available. This type of environment, however, challenges even the best camera systems, so compromises must be made when selecting the data acquisition rate. Although the laser sheet appears very bright to the human eye, the high-resolution CCD camera chosen for this experiment had a difficult time collecting this light and displaying it as an easily discernable image. The camera's lens was set to its lowest numerical f/stop value of 2.8 to

gather as much light as possible, and the spherical lens was put in place to increase light sensitivity. Different exposure settings were examined to figure out the best possible compromise between a high enough frame rate and a good quality, properly exposed image. Four exposure rates were chosen, and images taken at each of these exposure rates is shown in Figure 36 below:

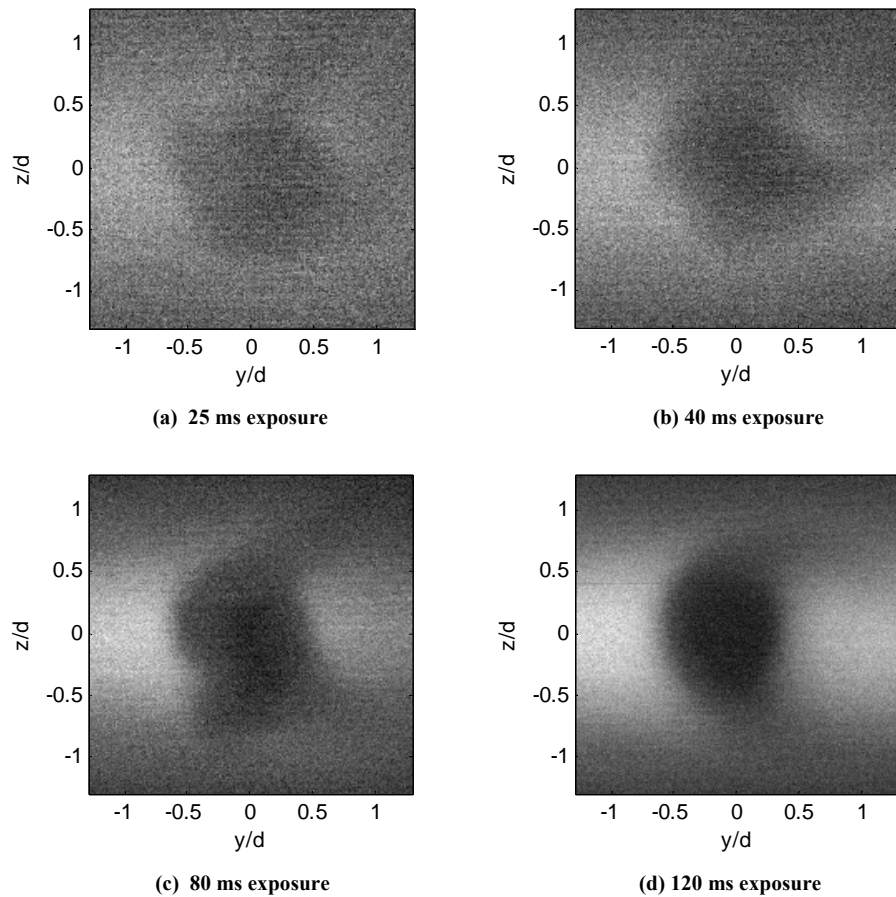


Figure 36. Four separate images collected at four different exposure rates. The upper left picture (a) was taken at an exposure rate of 25 milliseconds, and the rest of the images are similarly labeled with their respective exposure rates.

It is evident from the above figure that the 25 and 40 millisecond exposure rates did not produce good images, but the 80 and 120 millisecond exposure rates provided images that were easy to see. To further illustrate the differences among the four different frame rates, the average raw

intensity values were taken at a z/d location of zero for each frame rate represented above. The results are shown below:

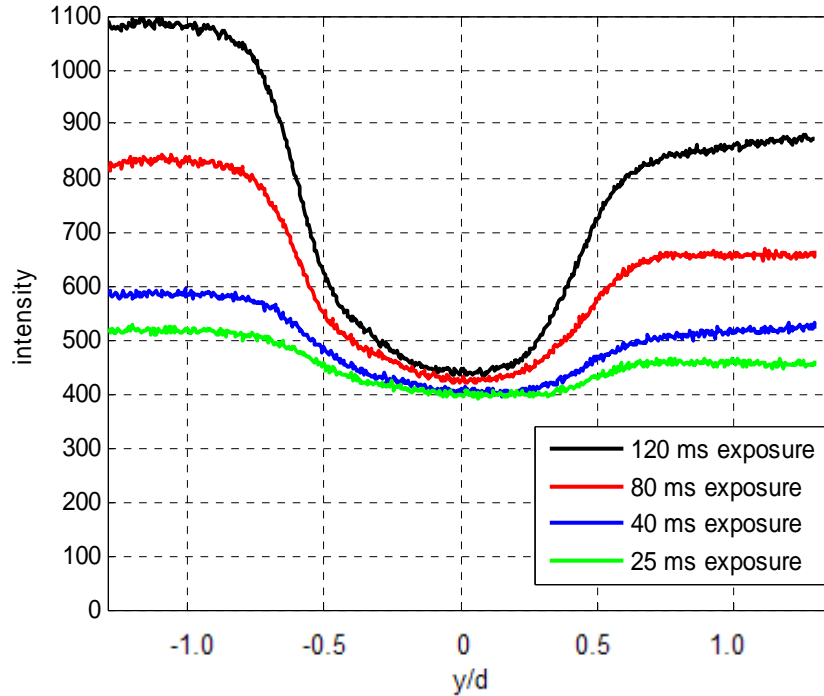


Figure 37. Plot showing the average raw intensity values for each of the frame rates examined.

The plot in Fig. 37 was generated by taking the single line of intensity values located at $z/d = 0$ across the width of the image (582 pixels). Each single line of intensity values above represents the average intensity of that same line over all 100 images at the exposure rate specified. The x-axis is labeled the same as in Fig. 36, and $y/d = 0$ represents the center of the helium jet. The 25 millisecond exposure rate revealed an approximate 120 count intensity difference between the brightest value produced by the laser when compared to the intensity at the center of the helium jet. There was an approximate 190, 400, and 650 count difference for the respective 40 ms, 80 ms, and 120 ms exposure rates when the highest intensity value was compared to the lowest at

the center of the helium jet for each rate. The intensity values to the right of center were lower than to the left due to the laser sheet expansion caused by the cylindrical lens.

In the end, the 80 ms exposure rate was the one chosen based on the quality of the images combined with the higher data acquisition rate it allowed over the 120 ms exposure setting. The 80 ms exposure time provided a marked increase in contrast between the helium jet and the laser sheet intensity values when compared to those of the 25 and 40 ms exposure rates. In the interest of time, these were the only four exposure rates examined.

In addition to setting the camera's frame rate, its binning also had to be set. The previous research used a 2x2 binning format, and this research uses the same. The 2x2 binning provides a good balance between high resolution and an acceptable signal-to-noise ratio. A higher numerical binning number reduces the resolution of the camera, but increases the signal-to-noise ratio. At the 80 ms exposure rate and this binning setting, the typical background intensity values were around 400, the laser sheet at its brightest showed intensity values of around 820, and the helium jet itself was around 420.

The images collected throughout these two experiments are presented in two different formats: the first is as a set of four images displayed in chronological order from left to right, shown as a false-color representation as processed by Matlab, and the second format is a fully processed set of data that shows the helium concentration and standard deviation. A single image displayed in the first, false-color format is shown in Figure 38 on the following page:

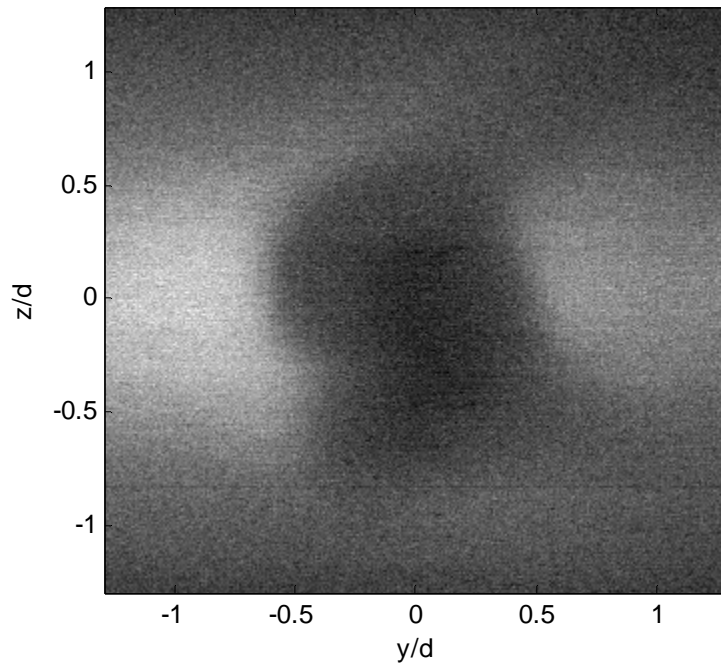


Figure 38. A random, false-color image as processed by Matlab, and presented as a grayscale image. The dark spot is the helium jet as it crosses the laser sheet.

The vertical axis is labeled in terms of vertical distance normalized by the tube's inner diameter (z/d), and the horizontal axis is labeled in terms of the horizontal distance normalized by the inner diameter (y/d). The image itself is centered on the approximate center of the helium jet, and that point is considered the origin. All of the images are scaled up or down in size based on the tube size being used so that each image is proportionally the same size regardless of tube diameter for ease of comparison. Most images are presented in grayscale, but certain images had to be presented using the hue saturation value (HSV) color palette.

Since all of the images in the 21 point data set were taken with the tubes 4 diameters away from the laser sheet, the smaller tubes had to be physically closer to the laser sheet to achieve the normalized distance of $x/d = 4$. In the case of the 1/8" outer diameter tube (0.081" inner diameter), it was close enough to the laser sheet that the tube itself glowed due to the laser

light in its immediate vicinity, even with the filter in place. This glow can be seen in the figure below:

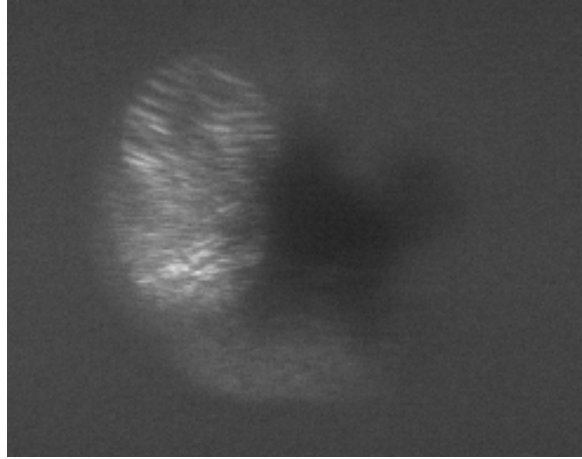


Figure 39. A screen capture of a single frame of data taken while helium was being expelled from the 1/8" O.D. tube. The helium is barely visible as the darkest spot in the image, and is surrounded by the reflection of the outside of the tube that appears white to the left and below the helium jet.

The green glow, which appears white due to the camera being of the black and white variety, was unavoidable regardless of the tube's surface treatment. The outer surface was first covered with black heat-shrink tubing to minimize the reflections, which produced the picture above, and finally, it was painted flat black which produced even worse results than those pictured above. Since the 1/8" O.D. tube provided many valuable data points, this is something that was worked around. In order to see enough contrast between the helium and the tube reflection, the false color images for the 1/8" tube are displayed with the HSV color scheme. Using these colors, the helium appears as an orange and yellow color combination, and the tube reflections appear as blue and violet colors.

The second presentation format showing the helium concentration and standard deviation was a much more time-intensive process that involved matrix manipulation in Matlab. In order to get helium concentration data, the following equations are used:

$$I \propto E_0 \sum_i X_i \sigma_i \quad (7)$$

where I is the collected power, E_0 is the irradiating intensity, X is the species mole fraction, and σ is the Rayleigh scattering cross section. In this situation, the air and helium mole fractions add to one, so a subtraction of the background intensity from each signal combined with Eq. (7) yields the helium concentration fraction, shown below:

$$X_{He} = \frac{1 - \frac{I_{He} - BG_{He}}{I_{Air} - BG_{Air}}}{1 - \frac{\sigma_{He}}{\sigma_{Air}}} \quad (8)$$

where I is the collected power, BG is the background intensity, and σ is the Rayleigh scattering cross section. Recall from chapter two that the Rayleigh scattering cross section of helium is 1.4 percent [10]. Each image is stored in Matlab as a matrix, and Matlab assigns a value to each pixel that corresponds to the intensity of that pixel. This value is stored as a 16-bit unsigned integer by Matlab, but the program is only capable of performing addition and subtraction with unsigned integers. In order to perform the division operations necessary in Eq. (8), the matrices are first converted to single precision values. The background intensity is determined by taking an average of 50 images with the laser turned off, and the air collected power (I_{Air}) is determined by taking an average of 50 images with the laser turned on, but without the helium flowing across the jet. The helium collected power (I_{He}) is determined by taking the average across all 50 images pixel-by-pixel as helium is flowing across the laser sheet, so each pixel is only averaged

against the other pixels at that same location. The standard deviation is also calculated pixel-by-pixel. So for each set of data, 150 total images, including 50 background images, 50 laser-only images, and 50 helium flow images are manipulated as matrices by Matlab, and an example result is displayed below:

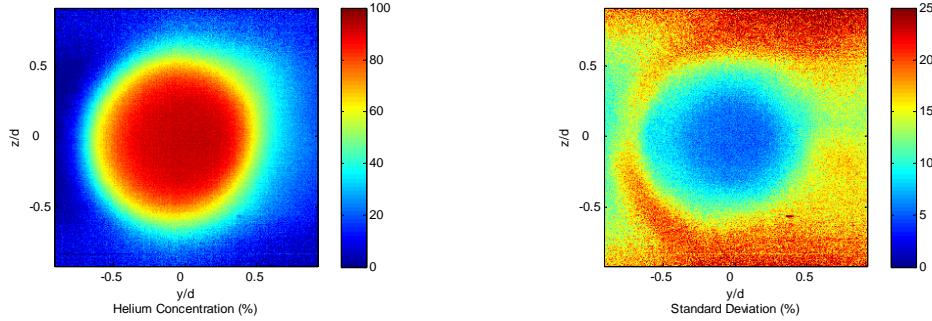


Figure 40. An example set of data reduced images. The image on the left shows the helium concentration that varies from 0 – 100%, and the image on the right shows the standard deviation that varies from 0 – 25%.

Note that the standard deviation displayed does not account for the fluctuations in helium concentration that occur during the camera’s 80 ms exposure, but is an indication of where fluctuations with relatively large time scales exist; i.e. where mixing is occurring over the 50 images.

3.4.3 *Trajectory Experiment Methodology*

Due to time constraints, only two different helium flow rates could be examined with respect to their trajectories. A simple methodology was chosen to figure out where these helium jets were in relation to the tube exit. The tube itself was measured and adjusted so that it was straight in the flow field box and centered top to bottom and side to side. A picture of the tube was taken as close as possible to a normalized distance of zero diameters away from the laser sheet. This image was examined in Matlab, and the approximate center of the tube was

determined in terms of a set of x/y coordinates. The flow field box was then moved to different x/d locations, and additional pictures were taken and examined in Matlab. The center of the tube remained at the same set of x/y coordinates regardless of x/d location, and thus serves as the reference point for all images taken. The helium concentration for each variation of the normalized distance from the tube exit was then calculated and displayed. Once that was displayed, the actual center of the jet was compared to the known location of the center of the tube, and this difference was recorded in terms of both x and y coordinates. The scissor jack was never touched, and thus z/d remained constant as the x/d distance was changed, so the full vertical and horizontal movement of the jet could be determined solely from the image itself. A set of four of these helium concentration images where the origin was actually the center of the tube instead of the jet itself is shown below:

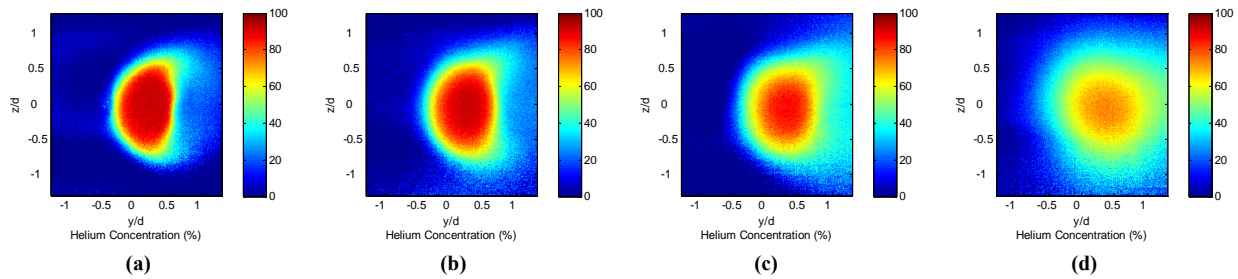


Figure 41. Mean helium concentration where the origin represents the center of the tube and not the center of the helium jet. From left to right, the normalized distances are $x/d = 2, 4, 6$, and 8 , respectively. Note that by the time $x/d = 8$, the center of the helium jet has moved nearly a full radius to the right of the center of the tube.

Once the distance of the helium jet away from the center of the tube was recorded, the images were then centered so that the helium jet itself was centered in the image window so that all images presented were standardized.

3.5 Chapter Summary

The core equipment used in this Filtered Rayleigh Scattering experiment includes a continuous wave, Argon Ion laser to illuminate the flow field, an iodine filter to suppress background and particle reflections, and a high resolution CCD camera to capture images of a helium jet as it crosses a sheet of laser light. A new flow field box is constructed to allow the quick and easy interchangeability of different sized tubes, and allows the Reynolds, Froude, and Grashof numbers of the helium jet to be changed as a result.

Two experimental setups are used to accomplish separate tasks. The first setup uses the vast majority of the optics listed in an effort to characterize the iodine filter. The second setup features the new flow field box, and uses FRS to characterize helium jet flows at different flow rates through various sized tubes. The results of the iodine filter characterization and the FRS images of the helium jet flows are presented in the following chapter.

4. Results and Analysis

4.1 Chapter Overview

The results of all four experiments performed throughout this research are presented in chronological order in this chapter. The iodine filter characterization experiment is first on the list, followed by the fixed Froude number experiment results, the fixed Reynolds number experiment results, and finally the brief jet trajectory experiment results. A summary of the results of the helium flow experiments concludes the chapter that examines the trends observed and relates it to other research that has been studied.

4.2 Experiment 1 Results: Iodine Filter Characterization

Two iodine filters were available for testing, and each was characterized using the experimental setup and methodology laid out in the previous chapter. The two iodine filters were externally identical, but differed in the amount of iodine each contained. This difference can clearly be seen in Figure 42 on the following page:

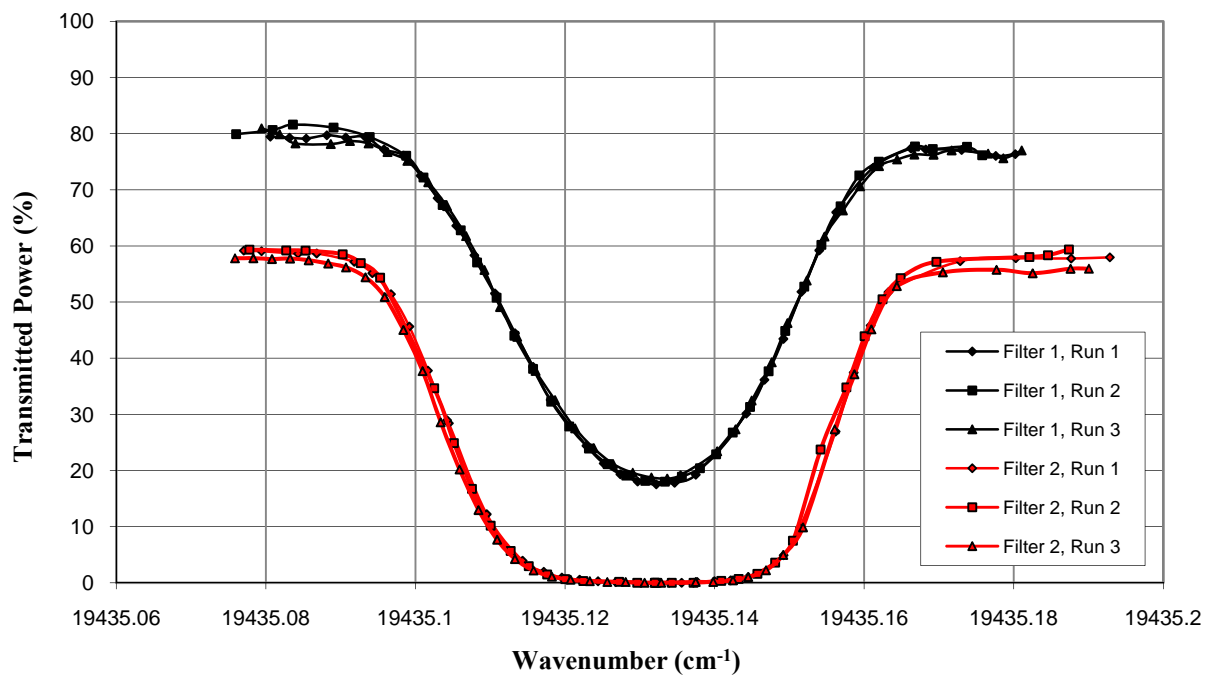


Figure 42. Results of the iodine filter characterization for the two filters available for testing plotted versus wavenumber. The black lines represent three separate runs for the first filter, and the red lines represent the three runs provided by the second, deeper filter.

This same figure is shown again in Figure 43 on the next page, only this time the x-axis is represented in terms of relative frequency:

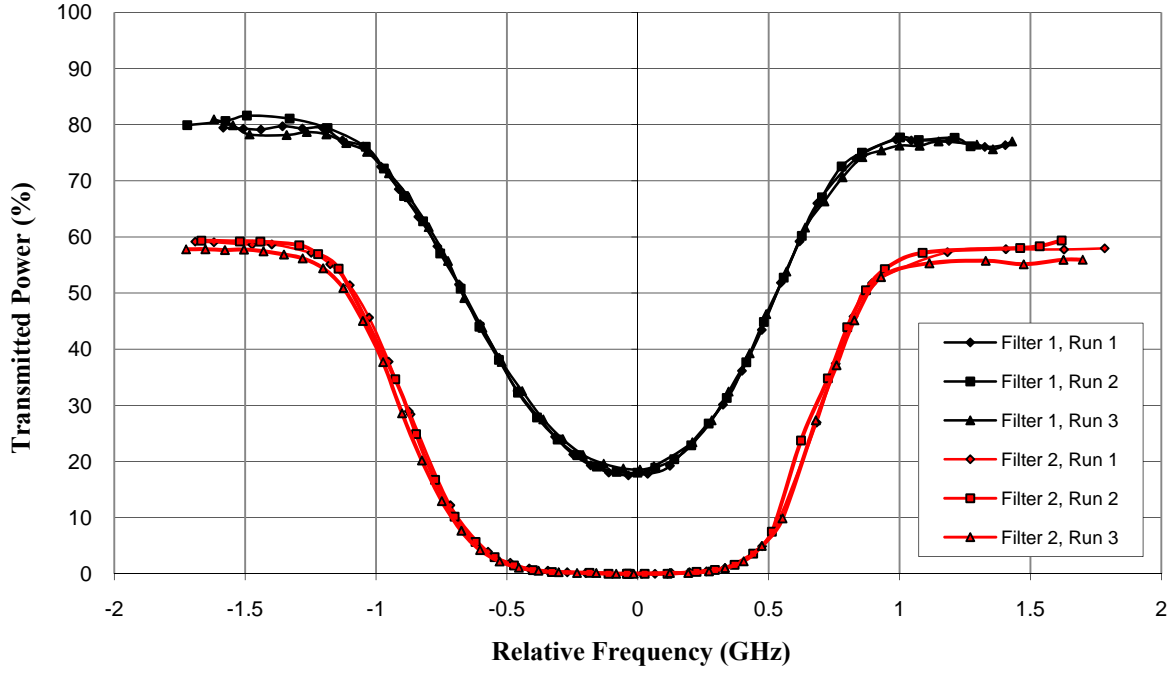


Figure 43. Results of the iodine filter characterization for the two filters available for testing plotted versus relative frequency.

The figure above is presented in terms of transmitted power versus relative frequency for ease of comparison to other research. The approximate center of the absorption notch for both filters occurred at a wavenumber of $19435.13336 \text{ cm}^{-1}$. A simple equation can be used to convert wavenumber to wavelength, and is shown below:

$$\text{Wavenumber}(\text{cm}^{-1}) = \frac{10^7}{\text{Wavelength}(\text{nm})} \quad (9)$$

Thus, the deepest part of the absorption notch corresponds to a wavelength of 514.532100 nm for each filter. This value was chosen as the basis for comparison for the entire set of data points.

The wavelength is related to frequency by the following equation:

$$f = \frac{c}{\lambda} \quad (10)$$

where f is the frequency in Hertz, c is the speed of light, approximated to be 3.0×10^8 m/s, and λ is the wavelength in meters. The wavelength value of 514.532100 nm corresponds to a frequency of 5.83054×10^{14} Hz, leading to the following equation:

$$Relative\ Freq\ (GHz) = \frac{Actual\ Freq. - 5.83054 \times 10^{14}}{10^9} \quad (11)$$

thus giving the relative frequencies of the other data points.

Filter 1 was manufactured with the intent of providing a more shallow absorption notch by reducing the amount of iodine available within its glass housing. This is evident from the apparent 20% greater power transmission throughout the curve when compared to Filter 2. Runs 1 and 2 for both the first and second filters were conducted at an iodine cell temperature of 80°C, and the third runs of each cell were conducted at a cell temperature of 90°C. This 10°C change in temperature was prompted by observing some iodine crystallization in the middle of the iodine filters' optical windows at 80°C. The crystallization appears as small metallic particles, and generally forms in the coldest part of the device, which in this case is the middle of the optical windows due to the filters being heated around the periphery of their cylindrical aluminum housings. This small increase in temperature was enough to eliminate the crystallization, thus ensuring that the images would be free of metallic particles while at the same time producing a minimal decrease in the amount of light transmitted outside of the absorption notch.

Filter 2 is the clear choice for use in an FRS experiment due to its ability to completely absorb the incident light at a selected wavelength, whereas Filter 1 would only absorb at most 83% of the incident light. Filter 2 was further tested by varying the internal cell temperature, and those results are shown in Figure 44 on the following page:

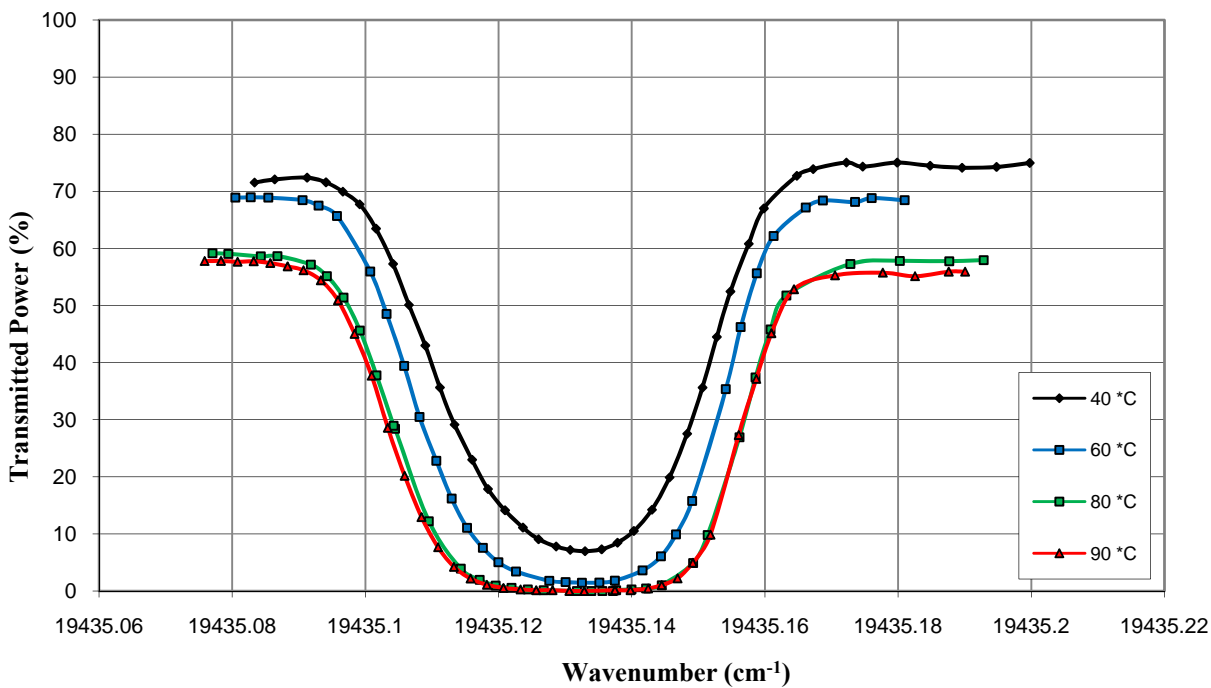


Figure 44. Results of the characterization of iodine Filter 2 at various temperatures. Note the decrease in incident light absorption as the filter temperature is decreased.

Figure 44 is shown again on the following page with the wavenumber replaced by the relative frequency, and the iodine filter internal temperature converted from degrees Celsius to degrees Kelvin for ease of comparison to other research:

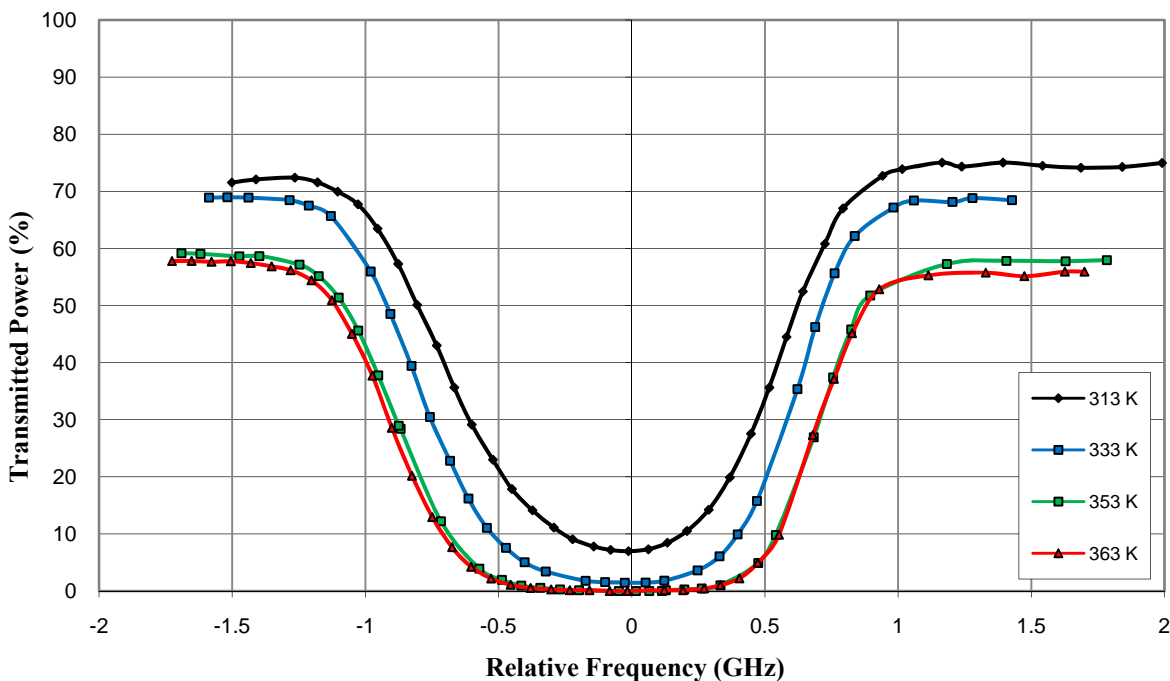


Figure 45. Results of the characterization of iodine Filter 2 at various temperatures. Note the decrease in incident light absorption as the filter temperature is decreased.

Each of these runs showed that the absorption notch was centered at $19435.13336 \text{ cm}^{-1}$, which backs the findings of the first set of experiments shown in Figure 42, and is a good starting point for adjusting the laser wavelength to enhance the use of this absorption notch as much as possible. The results of the runs in Figs. 42 - 45 also show the same general trends in relation to the frequency width of the absorption notch and the effect of the iodine cell temperature as the results given by Mosedale et al. in [36], Boguszko and Elliot in [5], and Shirley and Winter in [37]. It should be noted that the results presented in this document are obtained from an argon ion laser, and the results given in [36], [5], and [37] use a Nd:YAG laser system.

The iodine filter profile around the wavelength of the laser's operation is an exercise in compromise. Operating the filter at a temperature suitable for eliminating iodine crystallization reduces the amount of light that can be transmitted outside of the absorption notch, thus reducing

the signal-to-noise ratio for data collection. Fortunately, this is somewhat offset by the observation that the laser power was at a maximum during the absorption notch, but this is still not an ideal profile as was described in Chapter II, which would allow 100% light transmission outside of the absorption notch. In the interest of time, this was the only absorption notch fully analyzed, as others required setting the laser to a wavelength less than 514.5 nm, which would result in a decrease in the laser's output power according to the manufacturer's specifications and thus a corresponding decrease in signal-to-noise ratio.

The data points in Figures 42 - 45 are shown in Appendix A plotted with respect to the laser's wavelength for reference.

4.3 Experiment 2 Results: Fixed Froude Number Helium Flow

The following experimental results show the overall trends associated with the flow of the helium jet as its Froude number is held constant while the Reynolds number is varied. Four total Froude numbers are investigated including the approximate Froude numbers of 2, 10, 14, and 30. The results are presented in numerical order from the lowest fixed Froude number to the highest.

Table 4 below shows the conditions of the first set of data:

Table 4. Fixed Froude number of 2 (approx.) test conditions.

Picture Set	Tube I.D. (in.)	Velocity (m/s)	Flow Rate (SLPM)	Re	Fr	\sqrt{Gr}
(a)	0.352	1.503	5.68	106.00	2.02	52.6
(b)	0.454	1.704	10.72	155.00	2.01	77.1

The Reynolds numbers are both fairly low along with the helium flow velocity, so it is expected that the helium's buoyant nature should dominate the flow patterns, and this is evident from Figure 46 below:

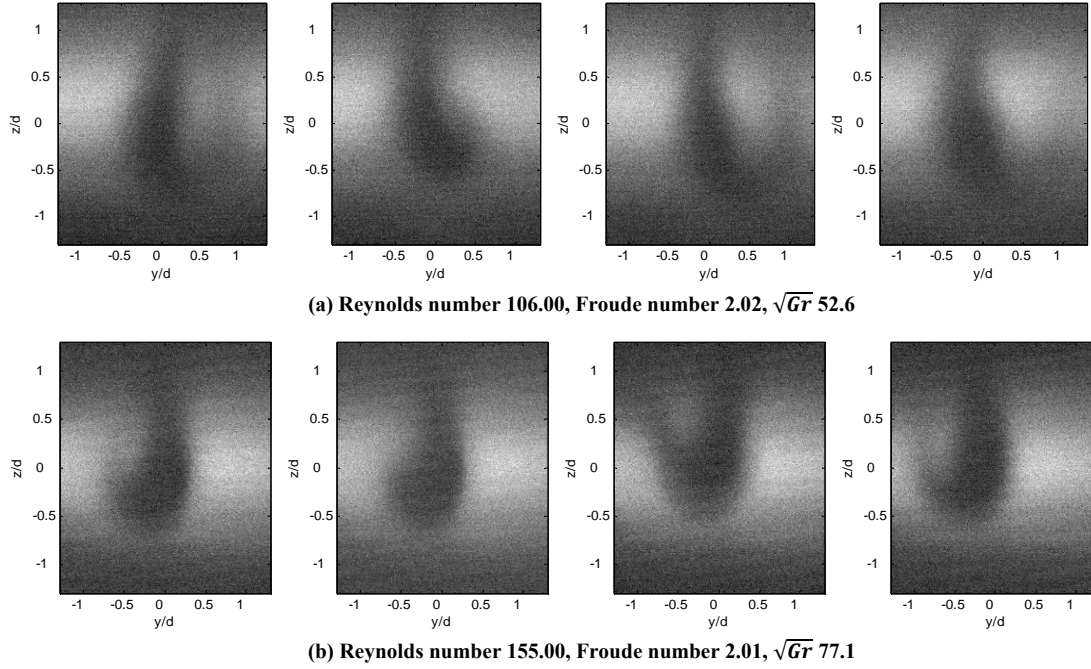


Figure 46. Two sets of four consecutive images representing the conditions listed in Table 4 taken at an exposure rate of 80 ms.

Both helium jets appear to stretch vertically, indicating that the helium's buoyancy is playing a large role in jets' behavior. Also noteworthy is the apparent instability of the helium jet, shown best in Figure 46 (b), the fourth image (far right). The center of the jet has moved approximately a half radius to the left of the image's center from the previous frame, which corroborates what was observed while the data was being recorded. Figure 47 on the next page shows the results of the 50 image average helium concentration and standard deviation for the same conditions:

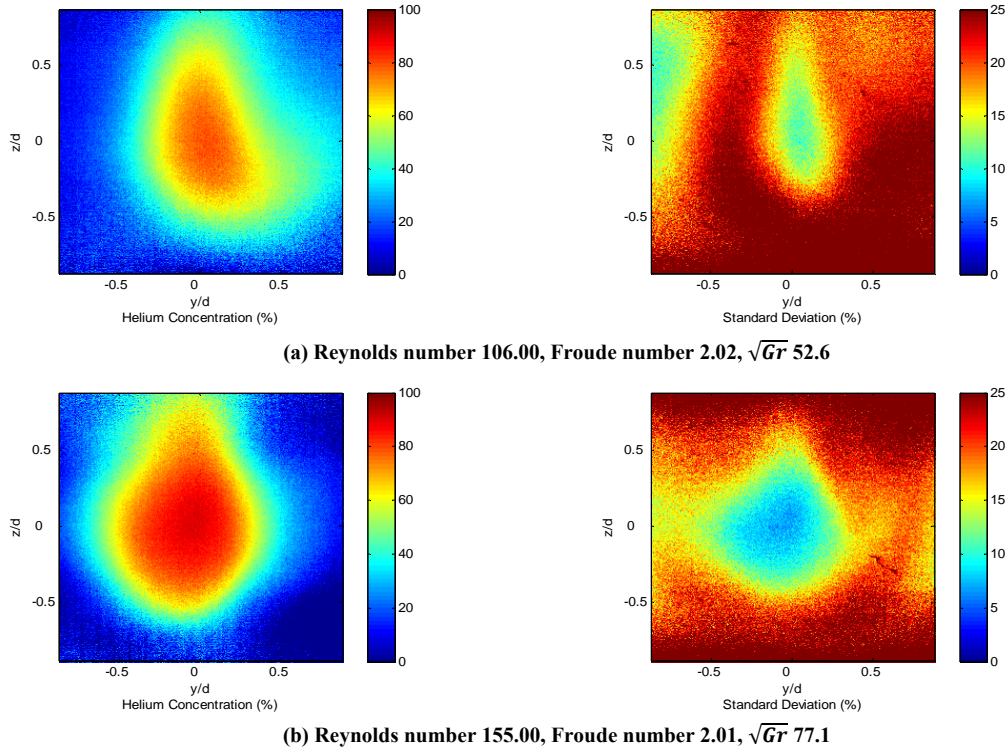


Figure 47. Mean helium concentration and standard deviation for the same conditions listed in Table 4, averaged over 50 images taken at an 80 ms exposure rate.

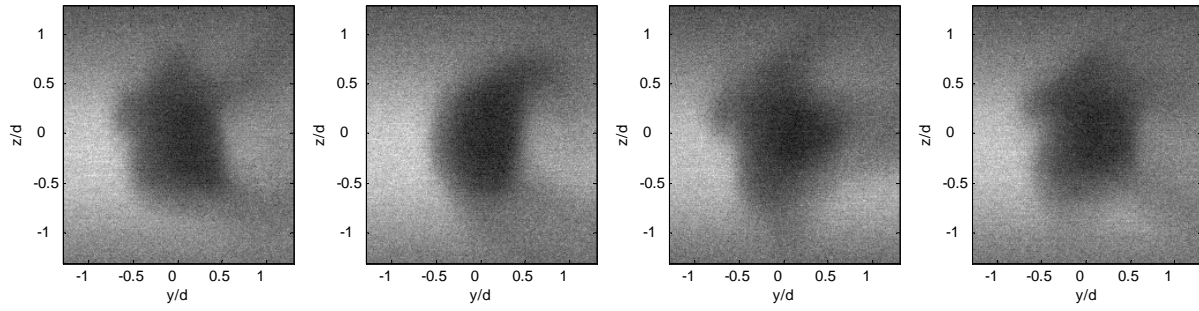
The overall shape of the jets over the 50 images indicates a core region of helium that is surrounded on the top and bottom of the image with the fluctuations in helium concentration caused by the jets' instability. The standard deviation for both indicates the greatest mixing around the core helium fluid. The red areas at the top and bottom of the standard deviation plots are a direct result of being close to the edge of the laser sheet; the signal (laser light) is the lowest at the edges, and thus the signal-to-noise ratio decreases.

The next set of data shows the effect of increasing the Froude number from approximately 2 to approximately 10. The Reynolds numbers are notably higher here than in the first set of data, as can be seen in Table 5 on the next page:

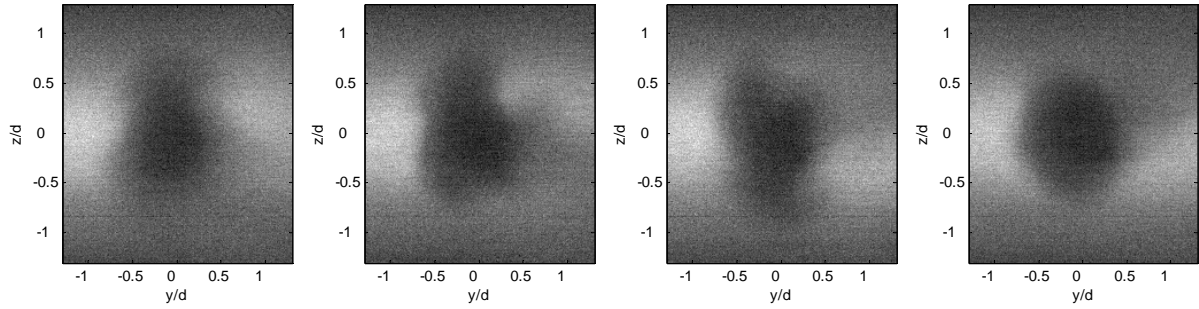
Table 5. Fixed Froude number of 10 (approx.) test conditions.

Picture Set	Tube I.D. (in.)	Velocity (m/s)	Flow Rate (SLPM)	Re	Fr	\sqrt{Gr}
(a)	0.224	5.84	8.94	262.10	9.82	26.7
(b)	0.306	6.85	19.56	419.84	9.85	42.6
(c)	0.352	7.35	27.77	518.01	9.85	52.6

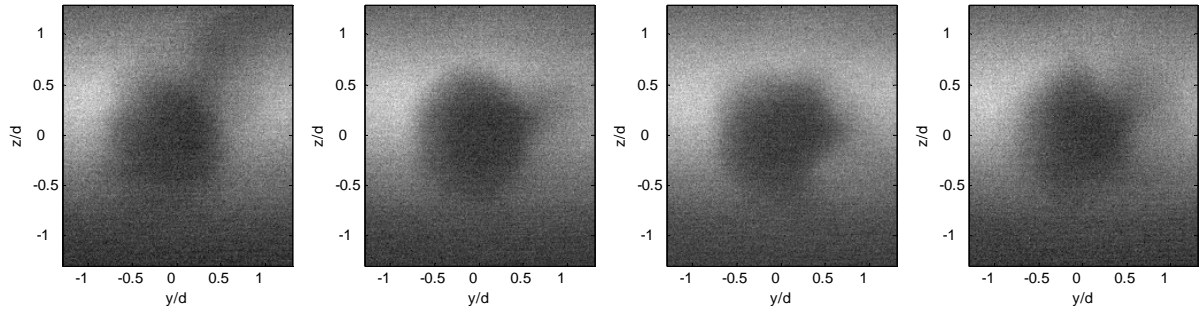
The three sets of four chronologically ordered false-color images representing the conditions listed in Table 5 are shown below:



(a) Reynolds number 262.10, Froude number 9.82, \sqrt{Gr} 26.7



(b) Reynolds number 419.84, Froude number 9.85, \sqrt{Gr} 42.6



(c) Reynolds number 518.01, Froude number 9.85, \sqrt{Gr} 52.6

Figure 48. Three sets of four images representing the conditions listed in Table 5 taken at an exposure rate of 80 ms.

The images shown on the previous page indicate the formation of side jets issuing from the center mass of helium for each of three conditions tested. The side jets appear to become less exaggerated as the Reynolds number is increased from 262.10 in the first set of four images to 518.01 in the last set of four images. The helium concentrations and standard deviations for the full sets of 50 images are shown on the following page:

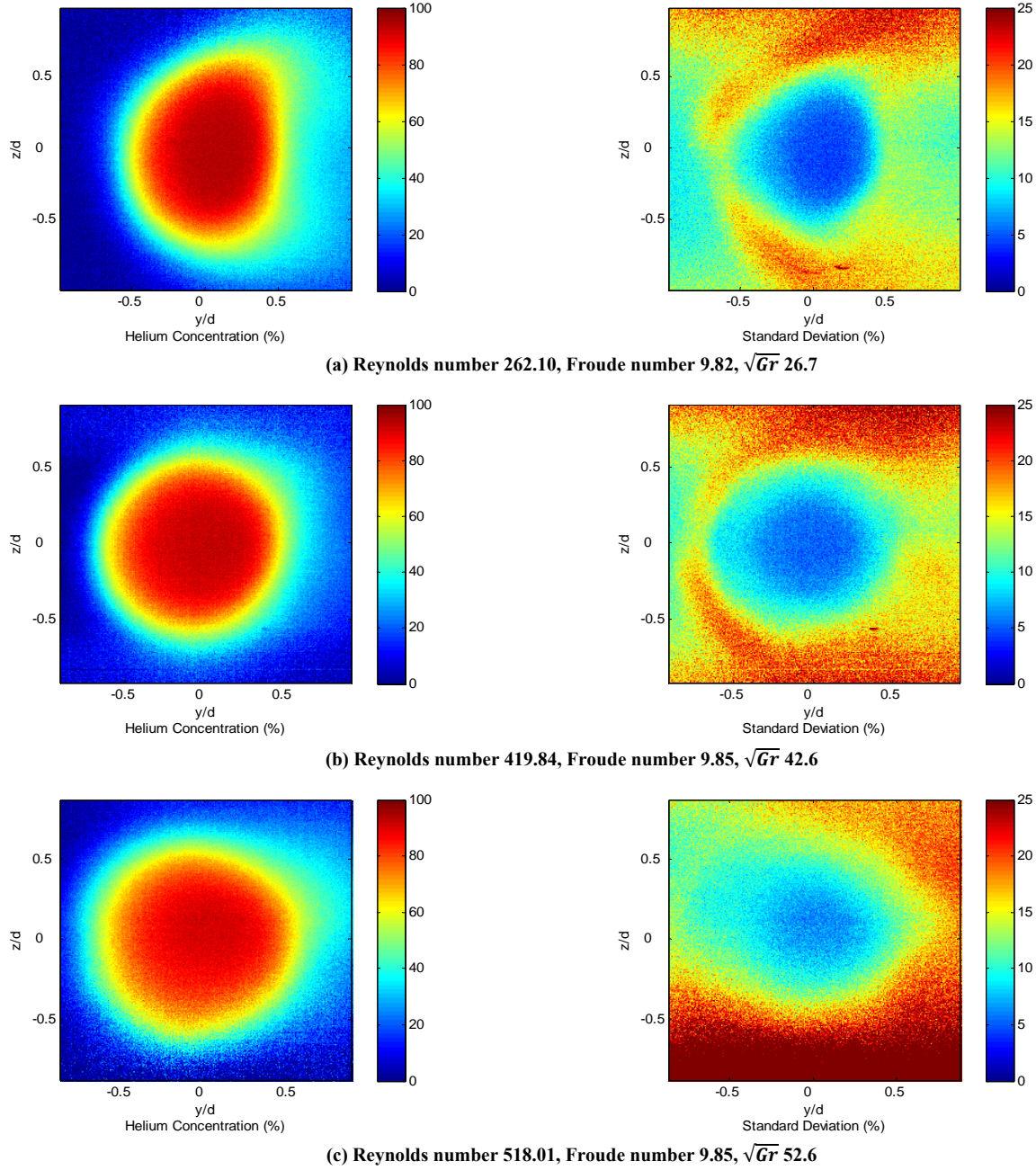


Figure 49. Mean helium concentration and standard deviation for the same conditions listed in Table 5, averaged over 50 images taken at an 80 ms exposure rate.

The helium concentrations for all three conditions show a clearly defined helium core at the center of each image that quickly diminishes approximately one radius in any direction from the center of the jet. The most noteworthy observations for Figure 49 involve the helium

concentration and standard deviation in Fig. 49 (a) and the standard deviation in Fig. 49 (c).

Figure 49 (a) depicts an overall shape that is similar in appearance to a crescent moon pointing to the right. This behavior is not unique to this set of flow conditions, and will be seen many times later as the results are presented. This behavior will be discussed at the end of this chapter. The standard deviation in Fig. 49 (c) indicates the most mixing at the bottom of the picture, but again, this is a result of the picture being taken near the fringe of the laser sheet.

The next three sets of flow conditions increments the Froude number to approximately 14, and covers a wide range of Reynolds numbers. These conditions are listed in Table 6 below:

Table 6. Fixed Froude number of 14 (approx.) test conditions.

Picture Set	Tube I.D. (in.)	Velocity (m/s)	Flow Rate (SLPM)	Re	Fr	\sqrt{Gr}
(a)	0.081	5.10	1.02	82.77	14.25	5.8
(b)	0.224	8.34	12.77	374.30	14.01	26.7
(c)	0.306	9.75	27.86	597.89	14.02	42.6

Again, the sets of four consecutive images are shown on the following page:

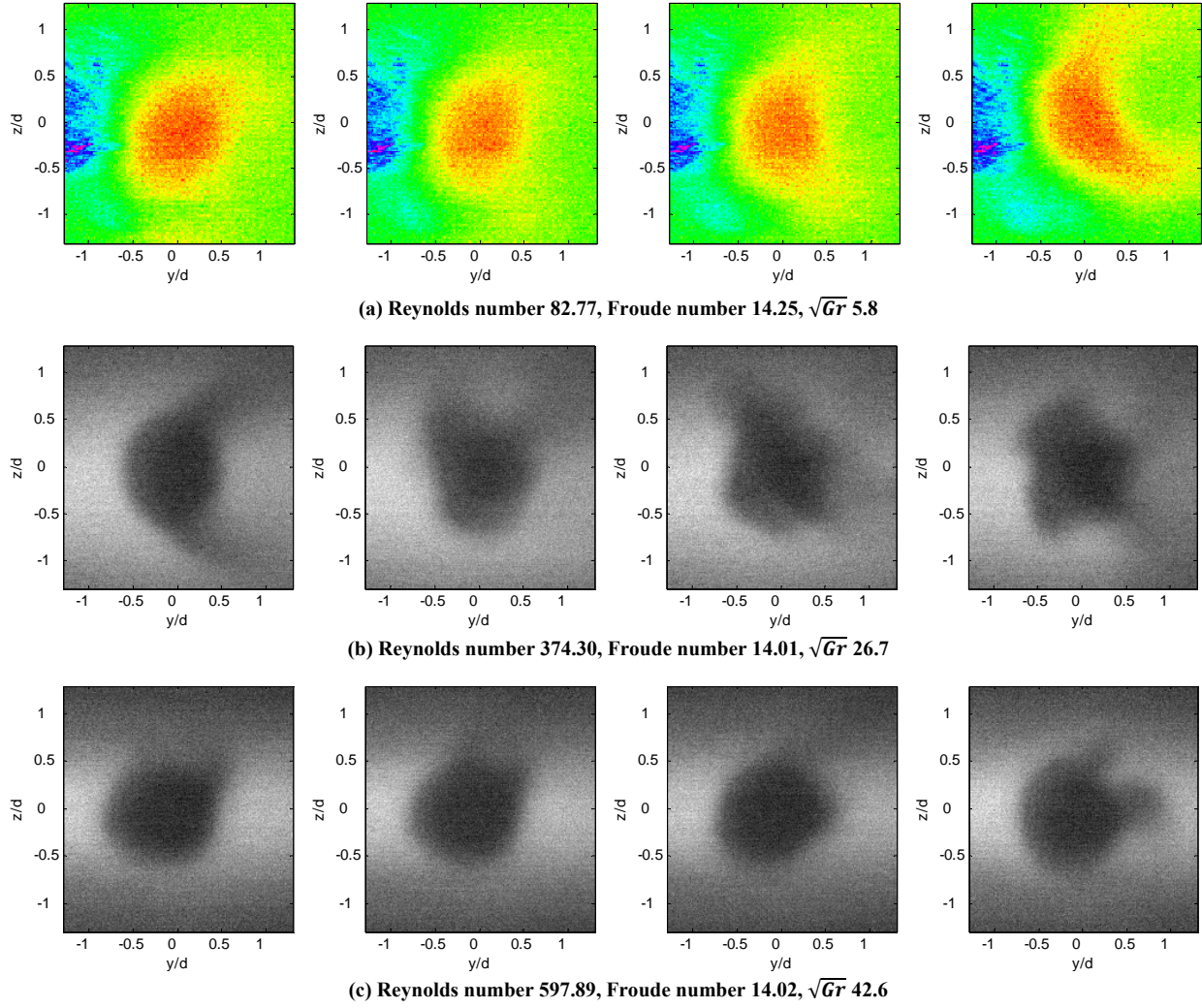


Figure 50. Three sets of four images representing the conditions listed in Table 6 taken at an exposure rate of 80 ms.

The results of the first set of flow conditions shown in Fig. 50 (a) indicate that the helium jet has taken on the same crescent moon shape noted previously. The last two sets of flow conditions at this Froude number show the formation of the side lobes of helium, and again, they are less exaggerated as the Reynolds number is increased. The helium concentrations and standard deviations are shown on the following page:

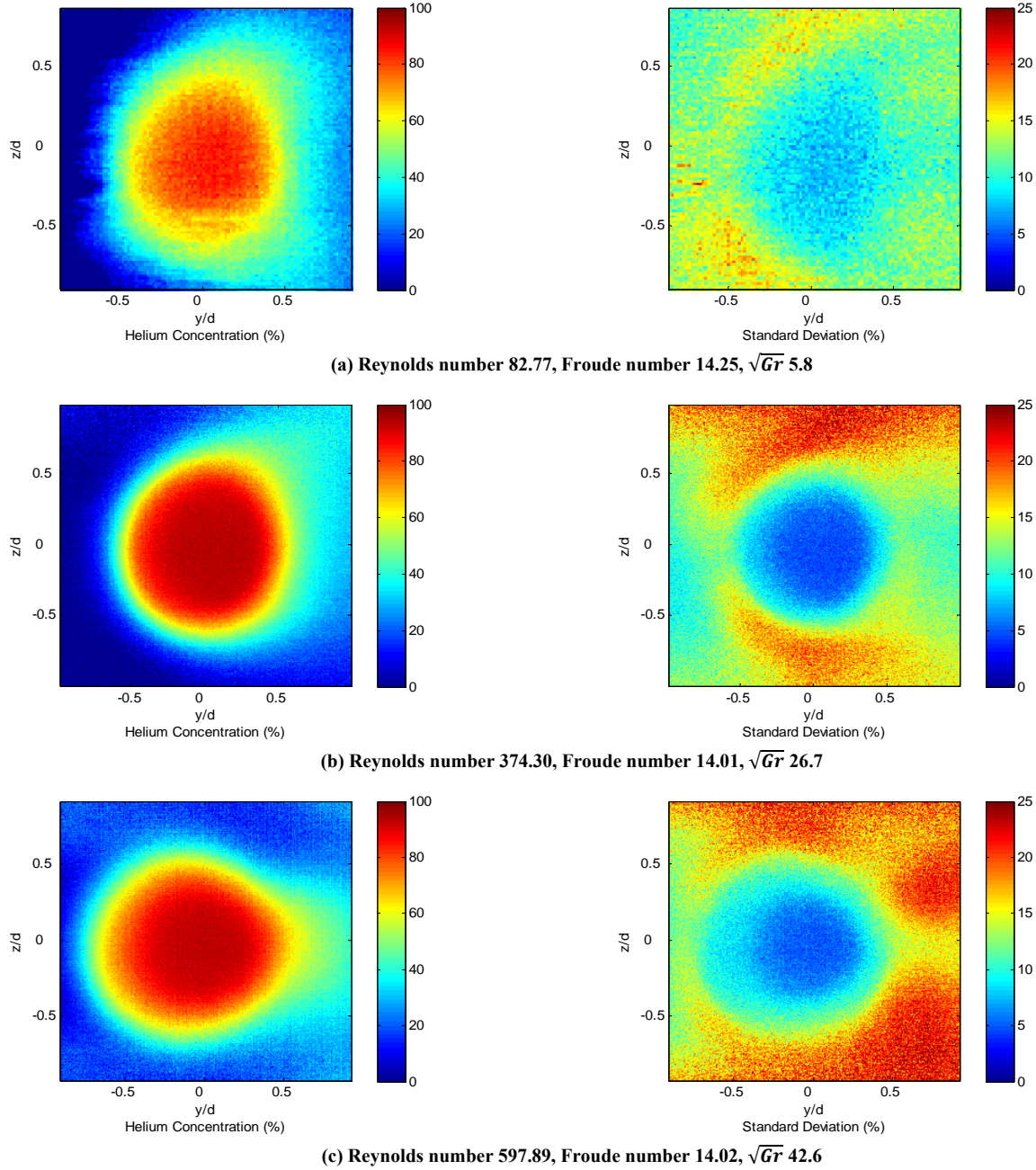


Figure 51. Mean helium concentration and standard deviation for the same conditions listed in Table 6, averaged over 50 images taken at an 80 ms exposure rate.

The crescent moon shape present in Fig. 51 (a) happens only at the lowest Reynolds number in this set of data, which mirrors the behavior observed in the previous set of data (fixed Froude number of ~ 10). The overall pattern of the standard deviations indicate that a greater amount of

mixing occurs farther away from the center of the helium jet as the Reynolds number is increased.

The final set of data observes the effect of setting the Froude number to approximately 30, and the two flow conditions tested are listed in Table 7:

Table 7. Fixed Froude number of 30 (approx.) test conditions.

Picture Set	Tube I.D. (in.)	Velocity (m/s)	Flow Rate (SLPM)	Re	Fr	\sqrt{Gr}
(a)	0.081	10.69	2.14	173.49	29.88	5.8
(b)	0.224	17.77	27.20	797.52	29.87	26.7

The two sets of four images created as a result of these flow conditions are shown below:

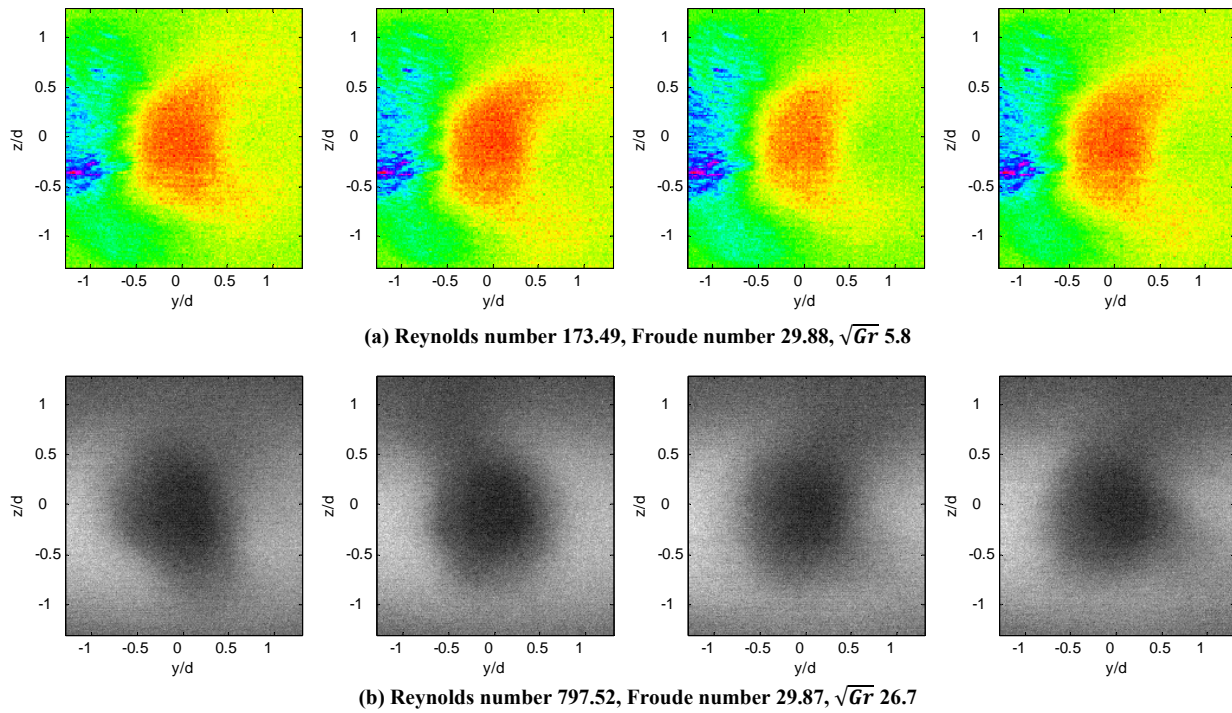


Figure 52. Two sets of four images representing the conditions listed in Table 7 taken at an exposure rate of 80 ms.

Again, the lower Reynolds number condition shows the reappearance of the crescent moon shape, but the formation of the side lobes of helium are notably absent from this set of data. The helium concentrations and standard deviations are shown below:

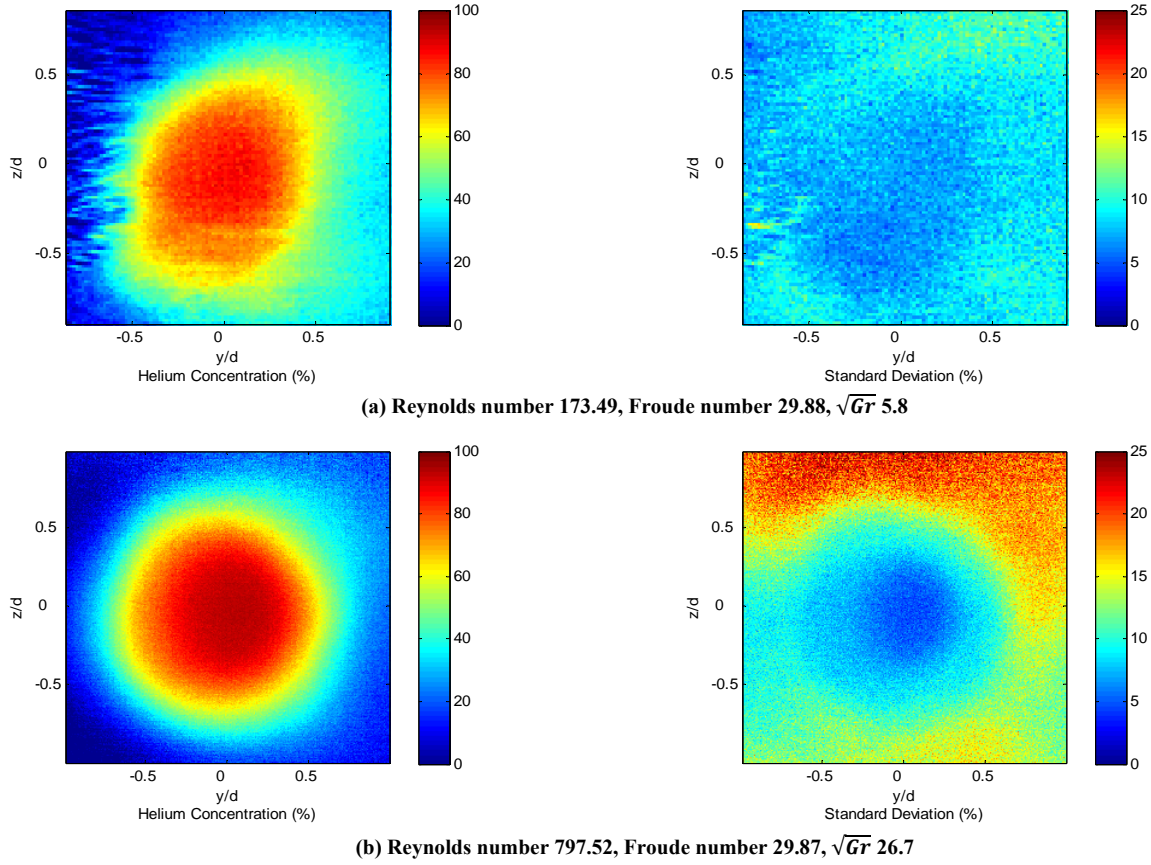


Figure 53. Mean helium concentration and standard deviation for the same conditions listed in Table 7, averaged over 50 images taken at an 80 ms exposure rate.

Just like previously, the increase in Reynolds number appears to cause a greater amount of mixing farther away from the core of the jet as shown by the two standard deviation plots above.

4.4 Experiment 3 Results: Fixed Reynolds Number Helium Flow

This experiment is conducted identically to the previous, only this time, the Reynolds number is held constant while the Froude number is changed. There are three total sets of data presented in this section, and they examine fixed Reynolds numbers of ~ 240 , ~ 400 , and ~ 670 respectively.

The first set of data covers five different flow conditions that are shown below in Table 8:

Table 8. Fixed Reynolds number of 240 (approx.) test conditions.

Picture Set	Tube I.D. (in.)	Velocity (m/s)	Flow Rate (SLPM)	Re	Fr	\sqrt{Gr}
(a)	0.081	14.90	2.98	241.81	41.64	5.8
(b)	0.224	5.36	8.20	240.51	9.00	26.7
(c)	0.306	3.95	11.28	242.05	5.68	42.6
(d)	0.352	3.43	12.96	241.69	4.59	52.6
(e)	0.454	2.65	16.68	241.23	3.13	77.1

Note that the velocity of the helium jet decreases as the flow rate increases, and the Froude number also decreases from one flow condition to the next. The five sets of four consecutive, false-color images are shown on the following page:

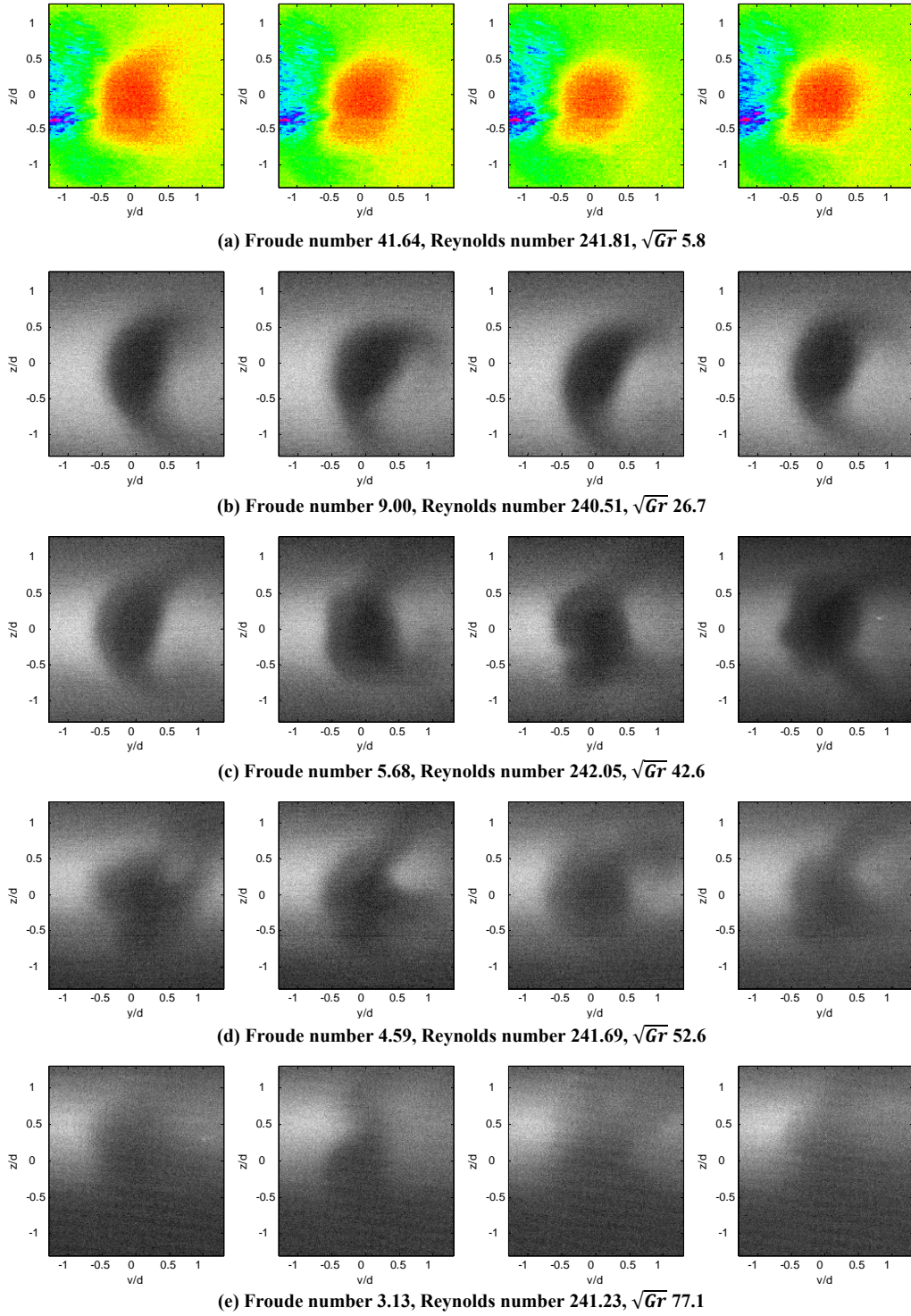


Figure 54. Five sets of four images representing the conditions listed in Table 8 taken at an exposure rate of 80 ms.

The first set of images in Fig. 54 (a) is unremarkable, and indicates a mostly stable helium jet. As the Froude number decreases, the helium jet takes on the crescent moon shape shown in Fig. 54 (b), the side lobes of helium show up in Fig. 54 (c) and (d), and at the lowest Froude number in Fig. 54 (e), the helium jet shows a great deal of dispersion, evidenced by the fact that it is very hard to see in the false color images. The helium concentrations and standard deviations are shown on the next page:

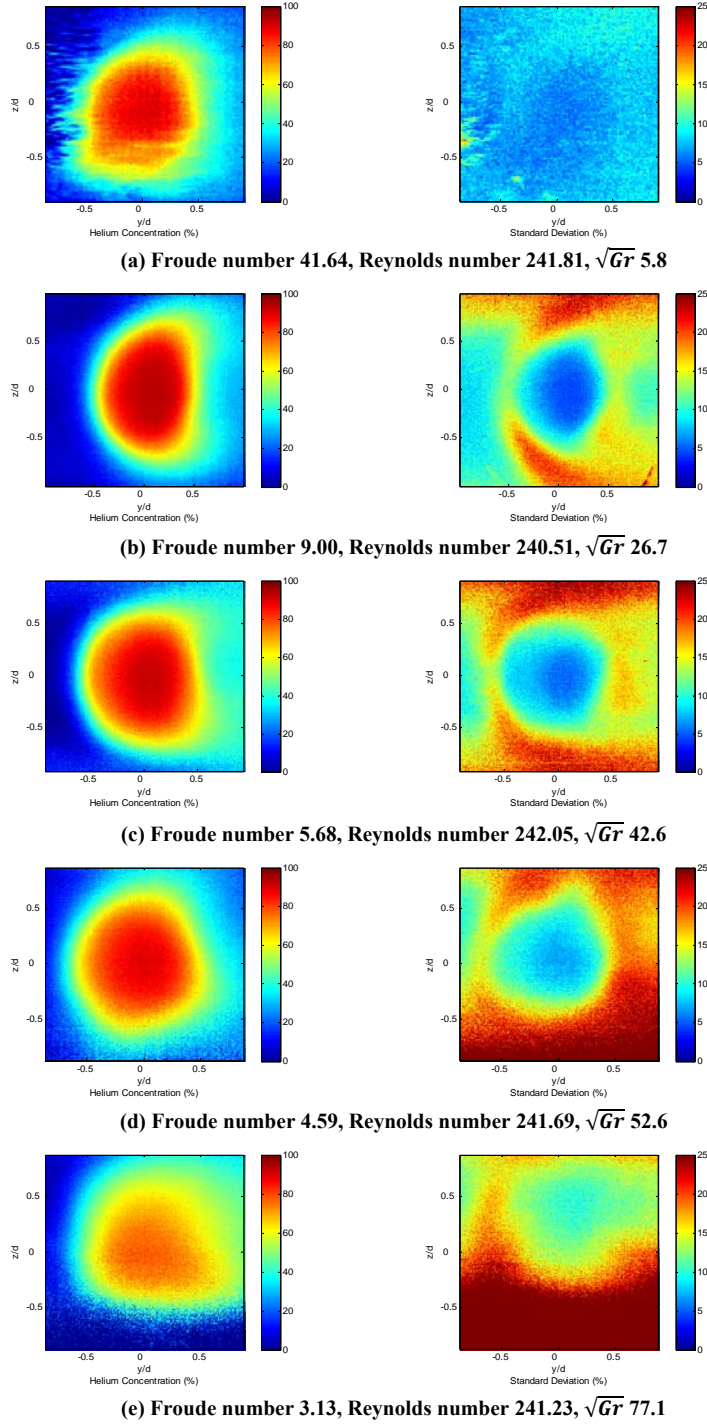


Figure 55. Mean helium concentration and standard deviation for the same conditions listed in Table 8, averaged over 50 images taken at an 80 ms exposure rate.

The most notable trends in Figure 55 show that the core concentration of the helium jet starts off very tight around the center of the jet, and as the Froude number is decreased, the core keeps spreading apart, and ends up looking somewhat disorganized at the lowest Froude number condition. The standard deviation also indicates that more mixing occurs farther away from the center of the jet as the Froude number is decreased.

The second set of data increases the Reynolds to ~400, and the flow conditions tested are shown in Table 9 below:

Table 9. Fixed Reynolds number of 400 (approx.) test conditions.

Picture Set	Tube I.D. (in.)	Velocity (m/s)	Flow Rate (SLPM)	Re	Fr	\sqrt{Gr}
(a)	0.081	24.68	4.94	400.53	68.98	5.8
(b)	0.224	8.88	13.60	398.76	14.93	26.7
(c)	0.306	6.52	18.64	399.92	9.38	42.6
(d)	0.352	5.67	21.44	399.88	7.60	52.6

The four sets of four images are shown on the following page:

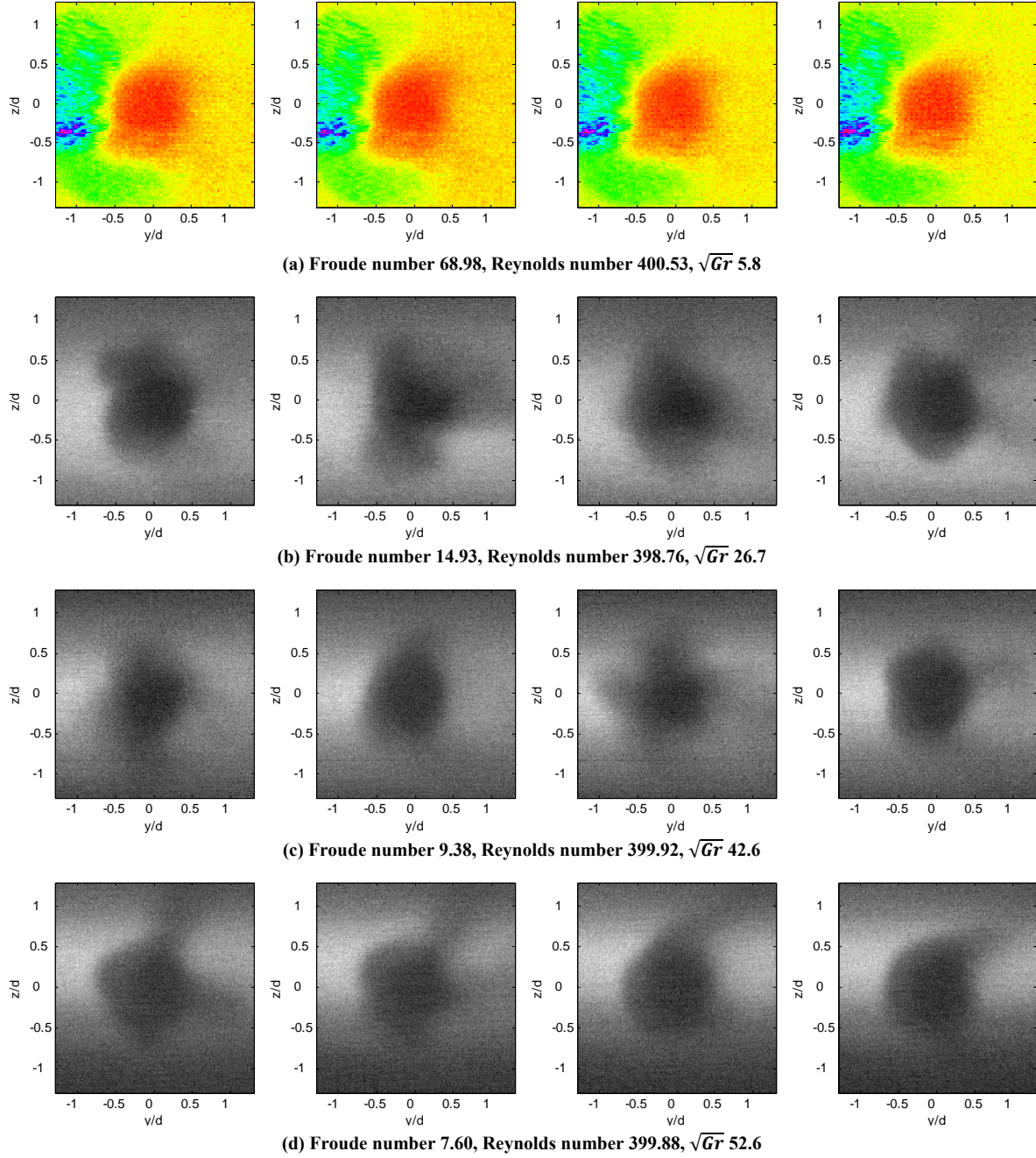


Figure 56. Four sets of four images representing the conditions listed in Table 9 taken at an exposure rate of 80 ms.

The side lobes of helium are clearly visible in Fig. 56 (b), (c), and (d), but not in (a) where the Froude number is highest. The helium concentration and standard deviation data are presented on the following page:

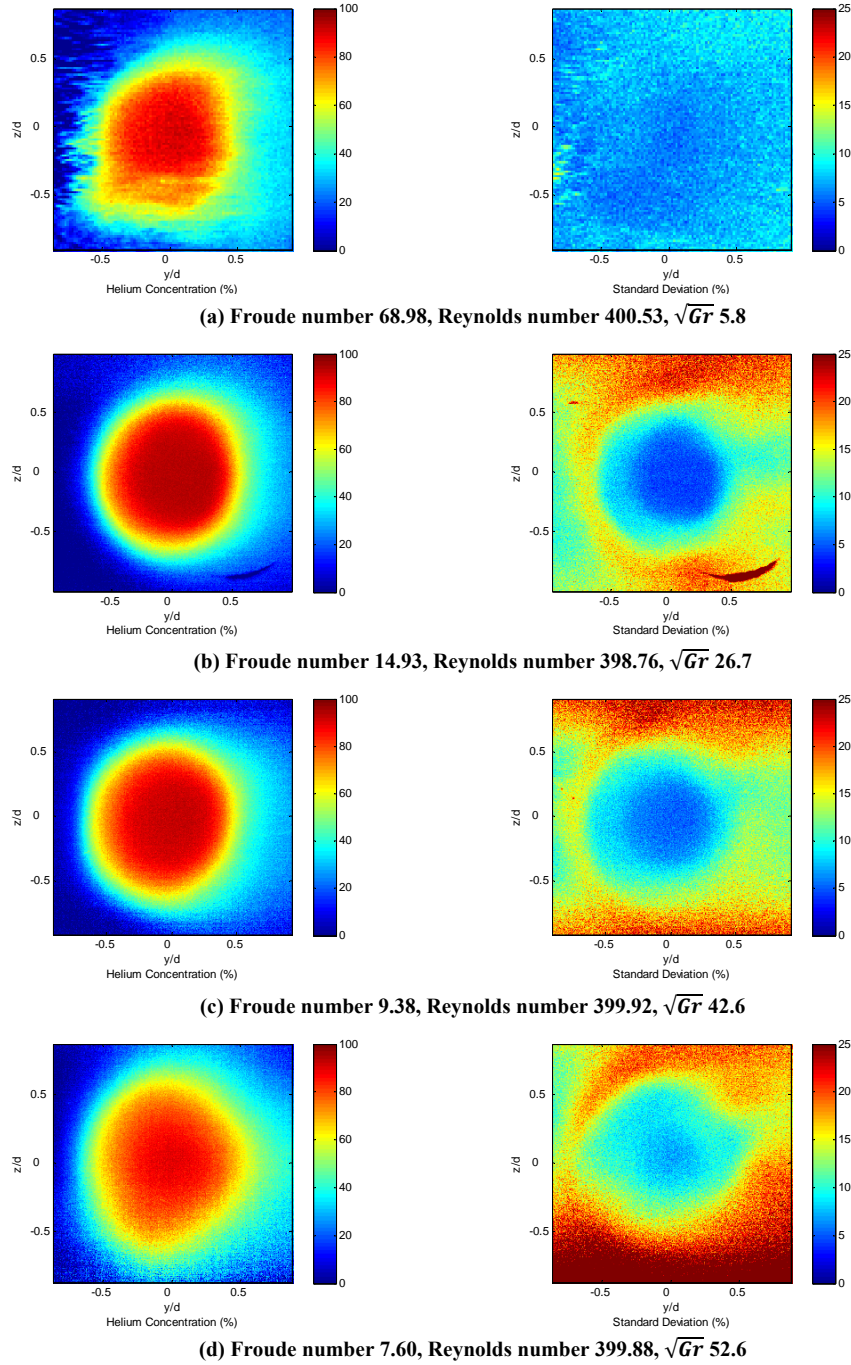


Figure 57. Mean helium concentration and standard deviation for the same conditions listed in Table 9, averaged over 50 images taken at an 80 ms exposure rate.

This set of data shows the same trends as the previous data set with the tight core of helium shrinking as well as more mixing occurring farther away from the center of the jet as the Froude number is decreased.

The final set of data only covers two flow conditions, and both have relatively high Froude numbers when compared to the previous sets of data. These flow conditions are shown below:

Table 10. Fixed Reynolds number of 670 (approx.) test conditions.

Picture Set	Tube I.D. (in.)	Velocity (m/s)	Flow Rate (SLPM)	Re	Fr	\sqrt{Gr}
(a)	0.081	41.42	8.29	672.20	115.76	5.8
(b)	0.224	14.98	22.93	672.08	25.17	26.7

As before, the sets of four consecutive images are shown next:

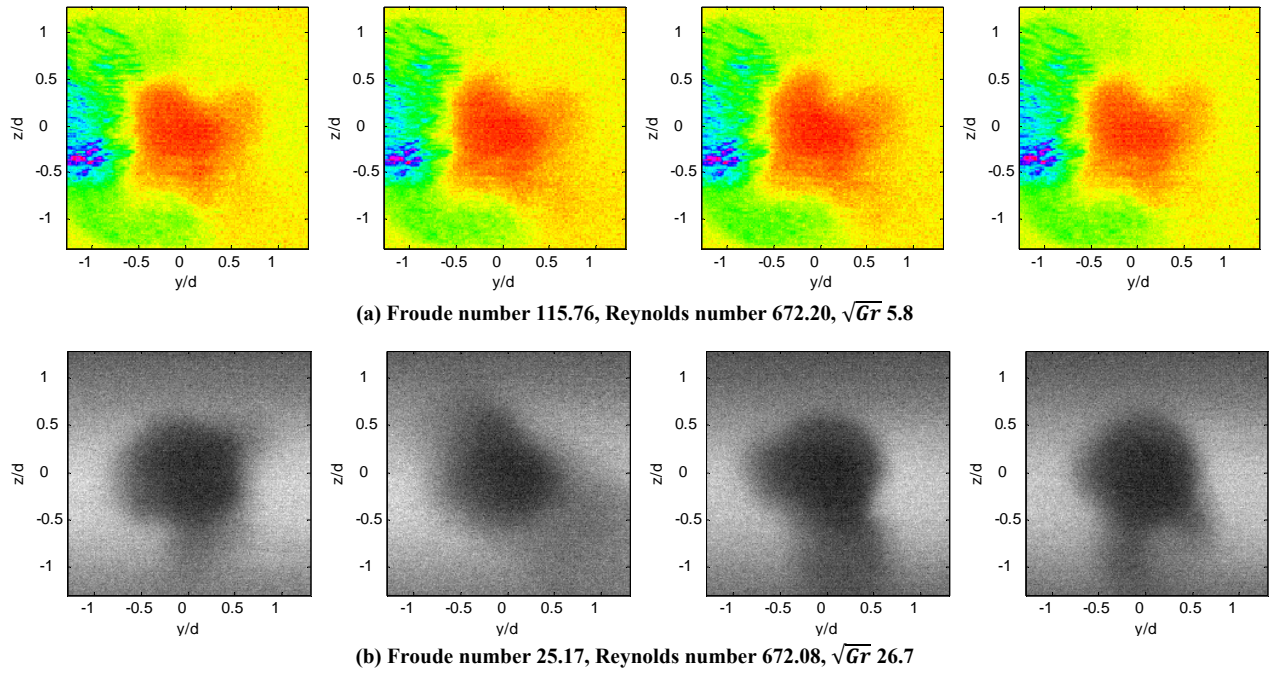


Figure 58. Two sets of four images representing the conditions listed in Table 10 taken at an exposure rate of 80 ms.

The figure above contains the most intriguing set of results between both experiments. The formation of the side lobes of helium is present in both sets of images. The previous trends showed an increased tendency towards the formation of these jets as the Froude number was decreased, and once it was decreased far enough, they ceased to exist. The Froude numbers

tested for this final set of data are notably higher than those previously examined, yet the side jets are present, thus indicating that the Reynolds number has some control over this phenomenon as well. The helium concentration and standard deviation are shown below:

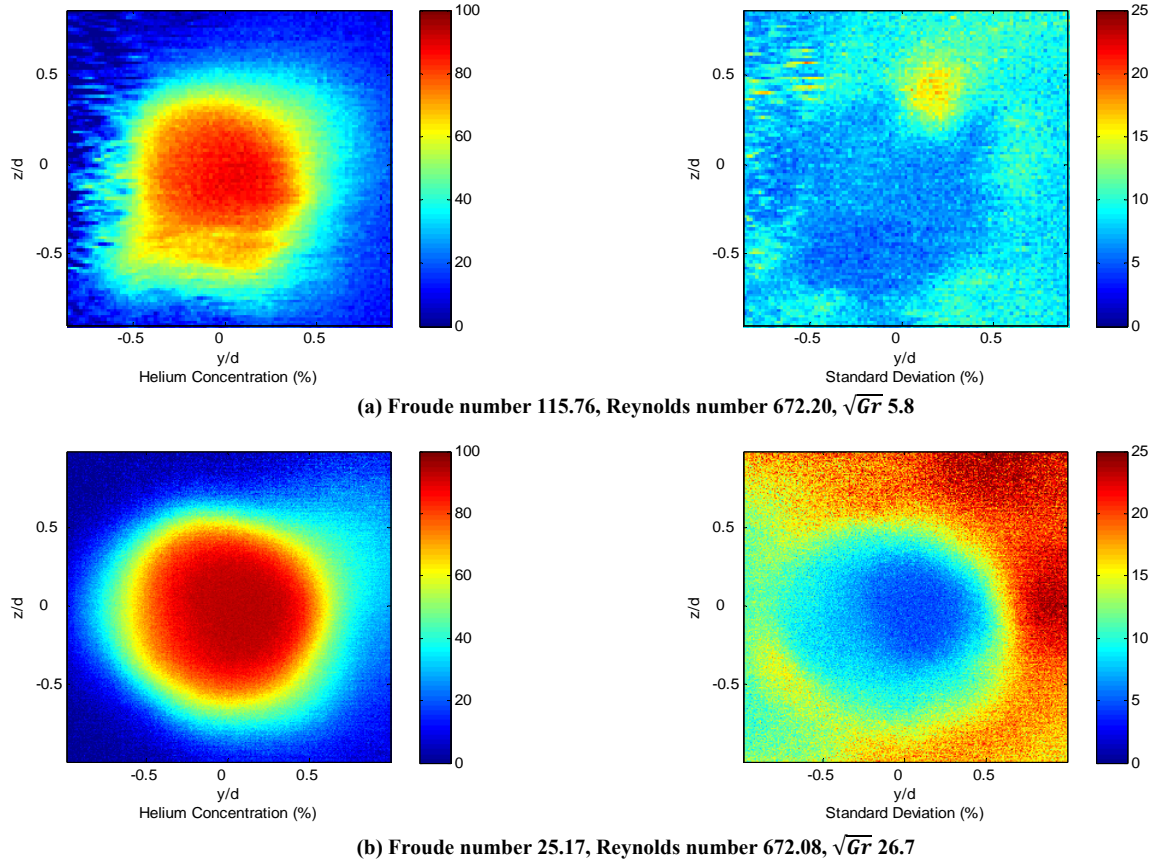


Figure 59. Mean helium concentration and standard deviation for the same conditions listed in Table 10, averaged over 50 images taken at an 80 ms exposure rate.

The results shown in Fig. 59 (a) and (b) follow the same trends noted throughout this particular experiment as the highest core concentration of helium shrinks and more mixing occurs farther away from the center of the jet with the decrease in Froude number.

4.5 Experiment 4 Results: Helium Flow Trajectory

This final experiment serves a two-fold purpose: the first is to map the trajectories of two of the more interesting flow conditions where side lobes were formed as observed from the previous experiments, and the second is to see if these side jets are formed as a function of the normalized distance away from the tube exit. Four sets of data are collected at x/d distances of 2, 4, 6, and 8 for each of the two flow conditions chosen.

The first set of conditions for this experiment is listed in Table 11 below:

Table 11. Trajectory experiment test conditions at a fixed Reynolds and Froude number.

Picture Set	X/D	Tube I.D. (in.)	Velocity (m/s)	Flow Rate (SLPM)	Re	Fr	\sqrt{Gr}
(a)	2	0.224	5.84	8.94	262.10	9.82	26.7
(b)	4	0.224	5.84	8.94	262.10	9.82	26.7
(c)	6	0.224	5.84	8.94	262.10	9.82	26.7
(d)	8	0.224	5.84	8.94	262.10	9.82	26.7

Just like in the previous experiment, four consecutive images are shown for each of the different conditions in order to get a qualitative idea of what the helium jet is doing in each case. These images are shown on the following page:

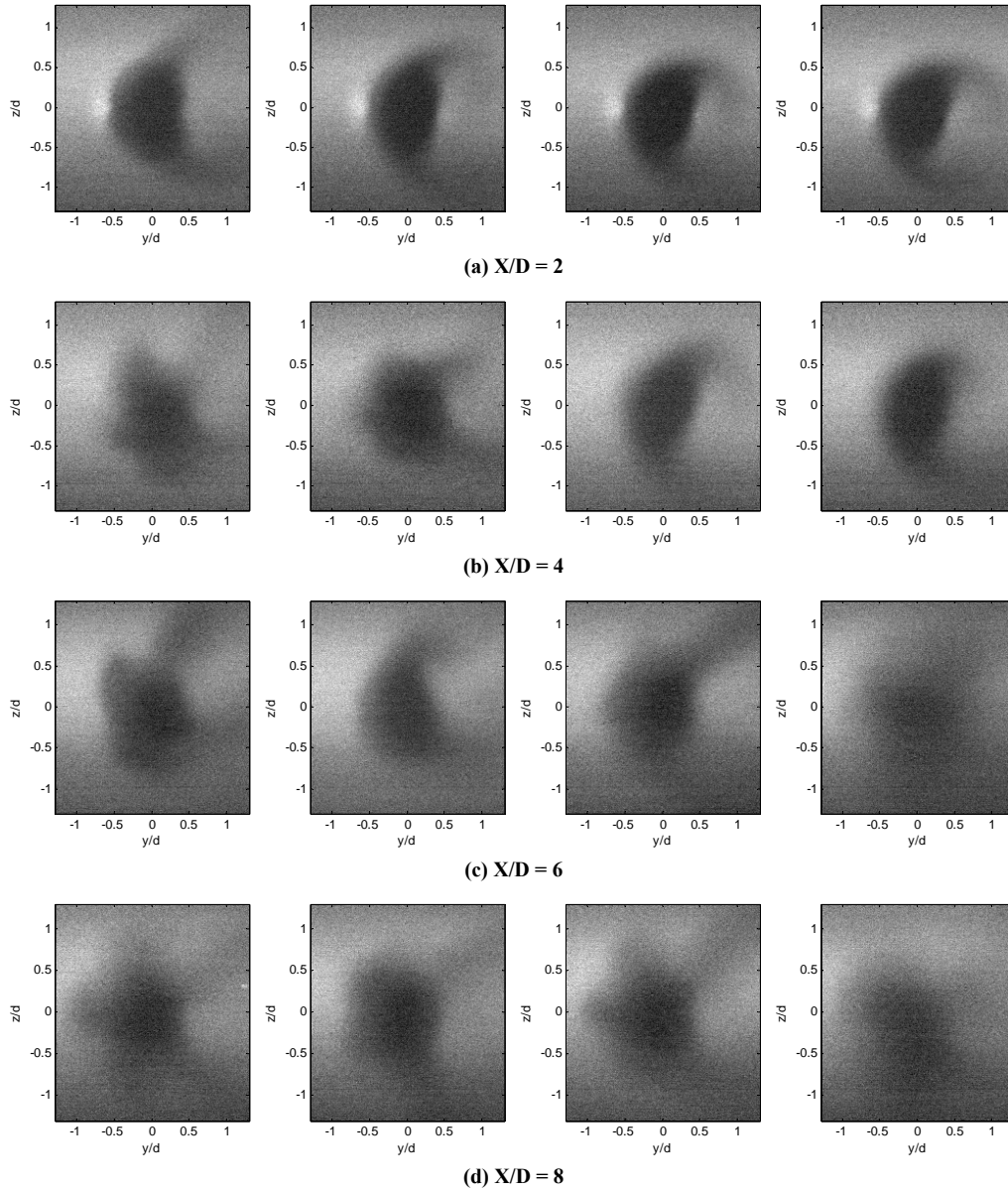


Figure 60. Four sets of four images representing the conditions listed in Table 11 taken at an exposure rate of 80 ms.

It is interesting to note that the formation of the multiple side lobes of helium does not appear until $x/d = 4$, and is present for the two following normalized distances. This observation seems to indicate that these side lobes are indeed a function of the distance of the helium jet away from the tube exit. The helium concentration and standard deviation plots are shown on the next page:

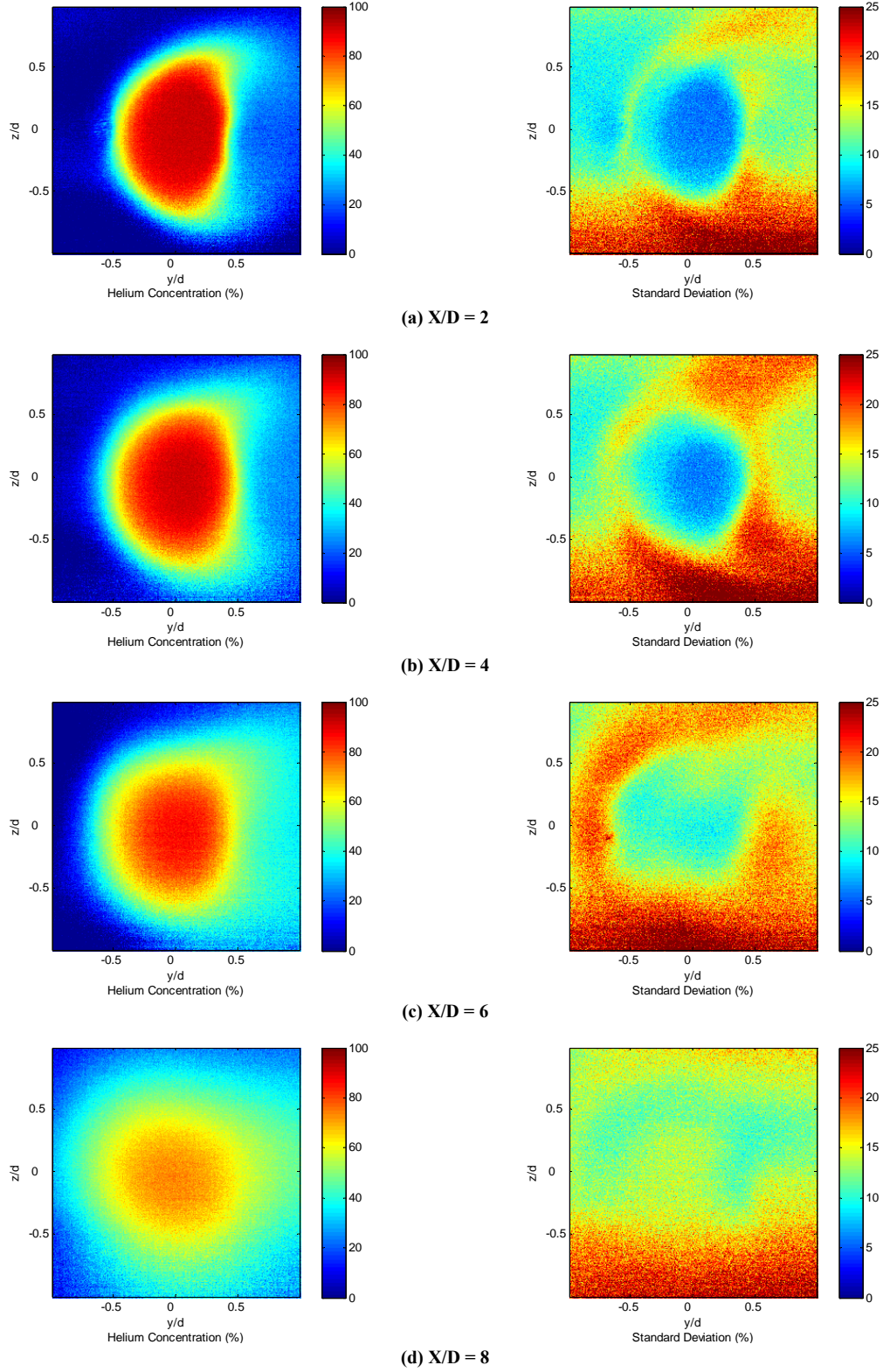


Figure 61. Mean helium concentration and standard deviation for the same conditions listed in Table 11, averaged over 50 images taken at an 80 ms exposure rate.

There are no surprises with this data; the most densely packed core of the helium jet shrinks as the jet moves away from the tube exit, and the mixing occurs farther away from the center of the jet as well with the increased normalized distance.

The next set of data again spans four different distances from the tube exit, this time for a higher Reynolds number, but nearly identical Froude number. The flow conditions tested are shown in Table 12 below:

Table 12. Trajectory experiment test conditions at a fixed Reynolds and Froude number. The Froude number has remained nearly constant compared to the previous set of data.

Picture Set	X/D	Tube I.D. (in.)	Velocity (m/s)	Flow Rate (SLPM)	Re	Fr	\sqrt{Gr}
(a)	2	0.306	6.85	19.56	419.84	9.85	42.6
(b)	4	0.306	6.85	19.56	419.84	9.85	42.6
(c)	6	0.306	6.85	19.56	419.84	9.85	42.6
(d)	8	0.306	6.85	19.56	419.84	9.85	42.6

The four sets of four images generated from these flow conditions are shown on the next page:

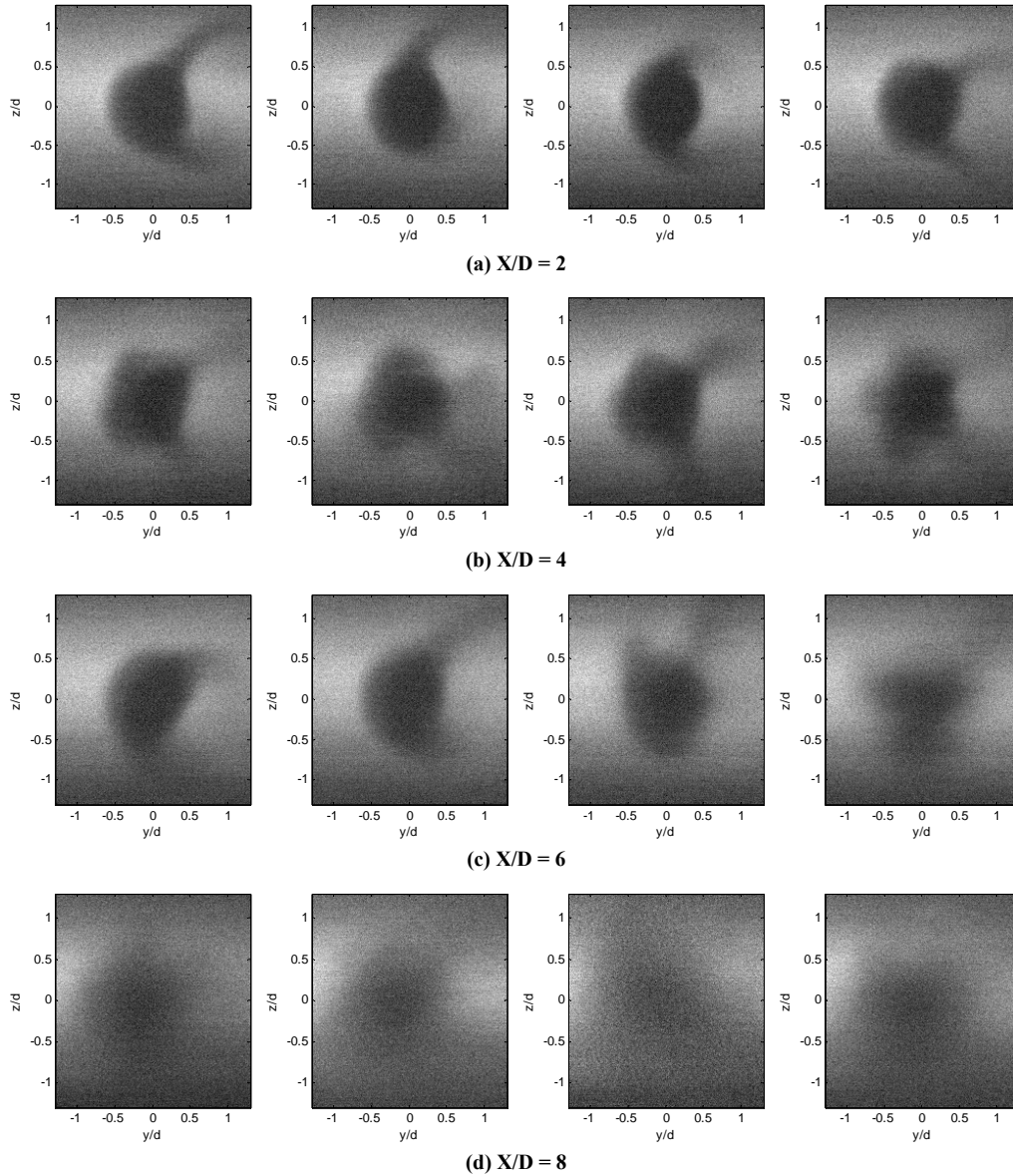


Figure 62. Four sets of four images representing the conditions listed in Table 12 taken at an exposure rate of 80 ms.

The results presented in Fig. 62 are slightly different from the previous set of data. The first sign of the formation of the side lobes still occurs at a normalized distance of four diameters away from the tube exit, but by the time the helium has reached 8 diameters away from the tube exit, the jet becomes very poorly defined, and there are no longer signs of clearly defined side lobes.

The helium concentrations and standard deviations are presented on the following page:

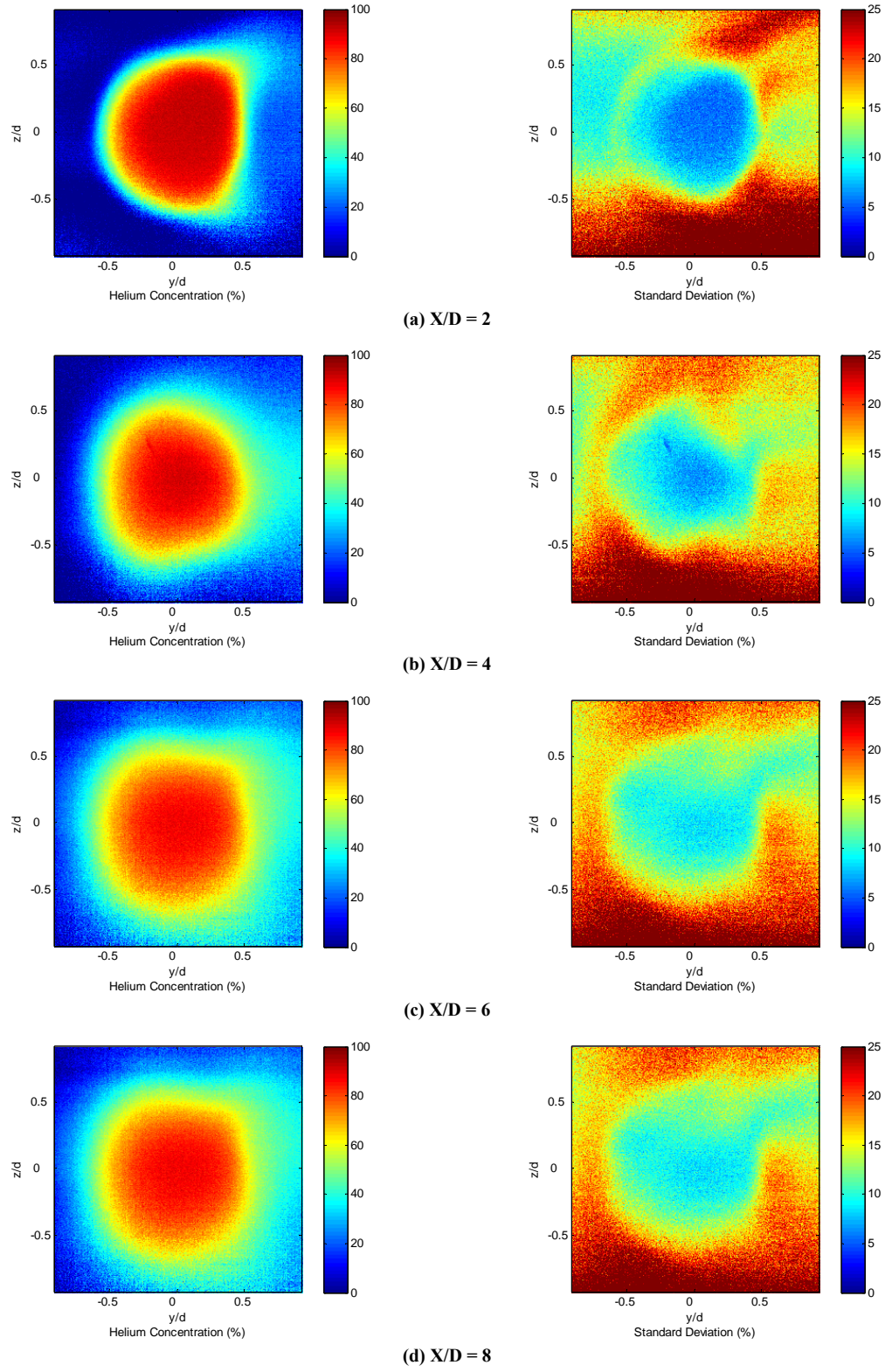


Figure 63. Mean helium concentration and standard deviation for the same conditions listed in Table 11, averaged over 50 images taken at an 80 ms exposure rate.

This data mirrors the trends seen previously. It is also interesting to note that the crescent moon shape present in the 50 image average helium concentration disappears in both cases once the jet has traveled at least six diameters away from the tube's exit.

Any movement in the vertical direction of the helium jet over the four different data points was very small, if any, indicating that the jet was clearly not under the influence of its buoyancy. It was clear, however, that the jet was moving to the right with each successive increment of x/d . The following trajectory map looks at the jet from a bird's eye perspective, and shows the helium jet's inclination to move to one side or the other. This map is shown in Figure 64 below:

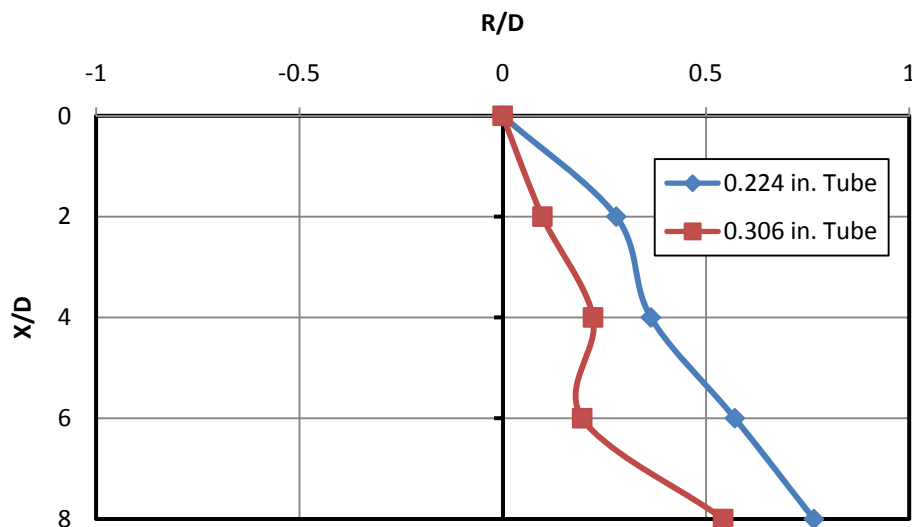


Figure 64. The trajectory of the jets as viewed from the top looking down in terms of the normalized horizontal distance as related to the tube radius compared to the normalized distance the jet has traveled from the tube exit as related to the tube diameter.

This result is quite interesting. The helium flow exiting the 0.224" inner diameter tube moves approximately three-quarters of a radius to the right by the time the flow reaches $x/d = 8$, and the 0.306" inner diameter tube's helium flow, which is at a comparatively higher velocity than the

flow exiting from the smaller tube, moves a little over a half radius to the right by the time it reaches the same x/d value. This jet movement seems to indicate that there is some sort of room current that is driving this behavior, and also helps to explain the presence of the crescent moon shapes that faced this direction. This observation will be discussed further in the following section.

4.6 Summary of Helium Jet Results

The point of this research from the outset was to characterize the formation of side jets of helium that were expelled from the core fluid in terms of Reynolds, Froude, and Grashof numbers. This behavior has been documented many times in the past as was eluded to in chapter two, and was found in the previous FRS research effort at AFIT. The formation of side jets proved to be a repeatable event during the experiments performed as detailed in this document, thus providing reliable and expected results. There was an additional behavior, however, that came in the form of a crescent moon shape that pointed to the right that was not expected. This crescent moon behavior is described first, and the discussion about the formation of the helium side lobes is reserved for last.

The crescent moon behavior of the helium jet was not present for all of the flow conditions tested, but was consistent and repeatable enough to warrant further investigation. The definition of crescent moon behavior is somewhat subjective since it is based on a qualitative analysis of the images gathered, but for the purposes of this research, it is defined as a helium flow that takes on the shape of a crescent moon pointing to the right, and must be the dominant behavior over all 50 images; i.e. the mean helium concentration must look like a crescent moon. The flow conditions where this behavior was present are listed on the next page in Table 13:

Table 13. Flow conditions where the crescent moon to the right is present as the dominant jet behavior determined from the mean helium concentration of the 100 images taken for each flow condition.

Case	X/D	Tube I.D. (in.)	Velocity (m/s)	Flow Rate (SLPM)	Re	Fr	\sqrt{Gr}
1	4	0.081	5.10	1.02	82.77	14.25	5.8
2	4	0.224	5.36	8.20	240.51	9.00	26.7
3	2	0.224	5.84	8.94	262.10	9.82	26.7
4	4	0.224	5.84	8.94	262.10	9.82	26.7
5	4	0.306	3.95	11.28	242.05	5.68	42.6
6	2	0.306	6.85	21.00	419.84	9.85	42.6
7	4	0.306	6.85	21.00	419.84	9.85	42.6

The table above indicates that this behavior occurs between a Froude number of approximately 5 and 14, and a Reynolds number between approximately 80 and 420. Lower Froude number flow conditions were also examined (see Figs. 46 and 47), but this crescent moon behavior was not dominant under those conditions. The lower Froude numbers examined indicate that the buoyant force was dominant enough to overcome this behavior. A similar argument could be made for the higher ends of the Reynolds and Froude numbers tested when compared to the conditions above. The helium flows stopped exhibiting this behavior at higher Reynolds and Froude numbers, indicating that the inertial forces at those points were enough to overcome the cause of this behavior.

It seems most likely that a room current could have caused this phenomenon. The two helium jets examined with respect to their trajectories in section 4.5 indicated that both jets were being pushed to the right, and both cases clearly showed the crescent moon behavior in their respective images. Every effort was made to minimize the possibility of adverse room currents, and none were discernable by physically feeling for a current in the region of the helium flow, but the evidence is stacked in favor of an air current, however small it may have been.

It should be noted that the presence of the crescent moon behavior and the formation of helium side lobes were not mutually exclusive events. Both events could happen under the same flow conditions, and would alternate back and forth as the data was taken. This observation is important; it indicates that these two phenomena are not interrelated, thus preventing the casual reader from questioning whether the crescent moon behavior documented kept the helium side lobes of interest from forming.

The focus on the formation of helium side lobes provided an interesting set of results. The definition of helium side lobes is subjective in nature but they most closely resemble the images shown in Figure 4 of [24], which were termed as azimuthal fingers in that particular study. The azimuthal fingers in that study were excited with piezoelectric actuators, which would often enhance their structure, making them easier to see [24]. This research did not explore the helical excitation of the observed helium side lobes (fingers), but instead focused on their natural occurrence as a result of changing the flow rates of the helium as it exited from different sized tubes. For the purposes of this document, helium side lobes are defined as azimuthal fingers that are the result of an expulsion of the core helium fluid into the surrounding environment. This behavior is vastly different from the crescent moon behavior discussed previously. Based on observation, the crescent moons were formed by helium being stripped from the top and bottom of the helium jet. The helium side lobes were fundamentally different in behavior in that the core of the helium flow would visibly shrink during the presence of the azimuthal fingers; this is somewhat intuitive since these fingers are formed by helium that was originally part of the core flow. The side lobes, however, were very fleeting in appearance; they would often only appear in two or three consecutive frames and then disappear, only to reappear again a few frames later. The flow conditions where these helium side lobes occurred in this

research is presented in the table below, listed in order of smallest diameter tube to the largest, and further sorted by the flow rates:

Table 14. Flow conditions where helium side lobes were present in the helium jet determined from examination of the images for each set of conditions.

Case	X/D	Tube I.D. (in.)	Velocity (m/s)	Flow Rate (SLPM)	Re	Fr	\sqrt{Gr}
1	4	0.081	41.42	8.29	672.20	115.76	5.8
2	4	0.224	5.36	8.20	240.51	9.01	26.7
3	4	0.224	5.84	8.94	262.10	9.82	26.7
4	6	0.224	5.84	8.94	262.10	9.82	26.7
5	8	0.224	5.84	8.94	262.10	9.82	26.7
6	4	0.224	8.34	12.77	374.30	14.01	26.7
7	4	0.224	8.88	13.60	398.76	14.93	26.7
8	4	0.224	14.98	22.93	672.08	25.17	26.7
9	4	0.224	17.77	27.20	797.52	29.87	26.7
10	4	0.306	3.95	11.28	242.05	5.68	42.6
11	4	0.306	6.52	18.64	399.92	9.38	42.6
12	4	0.306	6.85	19.56	419.84	9.85	42.6
13	6	0.306	6.85	19.56	419.84	9.85	42.6
14	4	0.306	9.75	27.86	597.89	14.02	42.6
15	4	0.352	3.43	12.96	241.69	4.59	52.6
16	4	0.352	5.67	21.44	399.88	7.60	52.6
17	4	0.352	7.35	27.77	518.01	9.85	52.6

The above table of results shows the conditions where the helium side lobes were formed, but the data trends are much easier to understand when viewed in graphical form. A previous study was done that examined the behavior of a buoyant, pure water jet injected into a brine solution [19]. Under certain conditions, a phenomenon referred to as bifurcation occurred, and this data was presented as a scatter plot of the data points plotted against the square root of the Grashof number and the Reynolds number [19]. A similar approach is taken with the data presented in Table 14, and the results are shown in the figure on the following page:

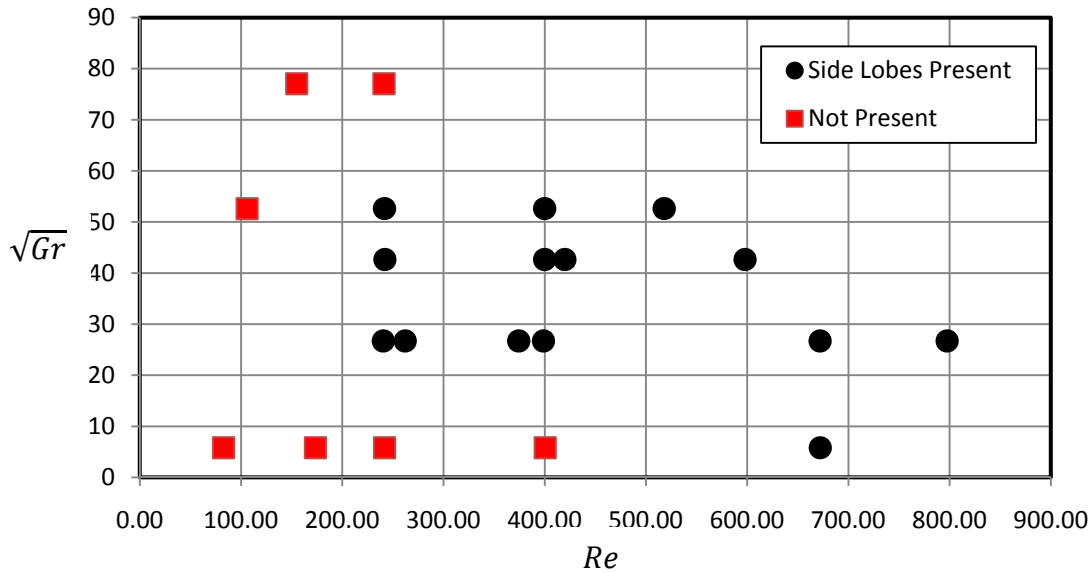


Figure 65. Scatter plot of all 21 data points taken at $x/d = 4$ plotted against the square root of the Grashof number and the Reynolds number. The black circles indicate that helium side lobes occurred under the conditions present at that point, and the red squares indicate data points where this phenomenon was not observed.

Figure 65 is important for two reasons. First, it clearly shows that the helium side lobes favor conditions that are grouped relatively close together when presented in this format. There appear to be upper and lower bounds to the Grashof and Reynolds numbers between which this phenomenon occurs, although there are not enough data points to clearly define these boundaries. Second, these results resemble those seen in [19] even though the only similarity between this document and that research is that buoyant jets were studied. Helium side lobes are clearly not the same phenomenon as the bifurcation of water presented in [19], yet they seem to be governed by similar values of the Grashof and Reynolds numbers.

Another observation of this helium side lobe phenomenon relates back to the study of helical mode excitation in [24]. According to that research, the observed azimuthal fingers could be enhanced due to certain modes of helical excitation, and one particular mode would often cause one of the fingers to become more enhanced than the others, and would sometimes

develop into a strong stream-wise vortex [24]. There were many instances where one helium side lobe would be much larger than the rest, as can be seen in Figure 66 below:

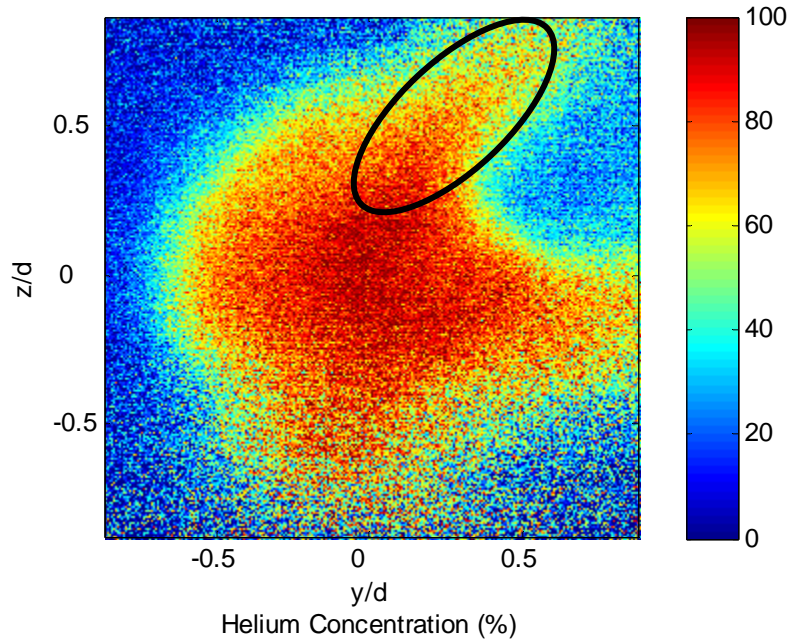


Figure 66. Single image taken from Fig. 54 (d) showing the formation of helium side lobes at a Froude number of 4.59 and a Reynolds number of 241.69. One of the side lobes, circled in black, is larger than the others.

Any of these abnormally large lobes observed tended to extend to the right of the image, suggesting that the same small room current that is suspect in the presence of the crescent moon phenomenon could also be responsible for this excitation.

Overall, the helium side lobes seemed to be more strongly a function of Froude number than the Reynolds number, but the Reynolds number played a role that cannot be ignored. A low Froude number, which indicates that buoyancy forces dominate over inertia, would not cause the helium side lobes. As the Froude number increased, the side lobes appeared, but only to a certain point. If the Froude number was held constant while the Reynolds number varied, any

side lobes present would become noticeably less exaggerated as the Reynolds number was increased. These observations were somewhat counteracted when the Reynolds number reached a value of around 670 when the helium side lobes appeared seemingly regardless of the size of the Froude number. These results were all repeatable, suggesting that this phenomenon, although fleeting in nature, is one that consistently occurs given the right conditions.

5. Conclusions and Recommendations

5.1 Research Conclusions

AFIT's Filtered Rayleigh Scattering experimental setup was further evaluated and refined with the addition of a wavelength meter that was used to observe and record the Argon ion laser's wavelength. This information was crucial to being able to evaluate the iodine filter that was chosen for this setup. This molecular absorption filter was fully characterized, and the laser's output wavelength was adjusted to match the filter's absorption notch to suppress any errant background and particle reflections.

The FRS system was then used to evaluate the behavior of a buoyant helium jet that was injected horizontally into the ambient air of the lab environment. Previous research at AFIT indicated the tendency of this jet to form side lobes of helium where helium was expelled from the core of the jet in a manner that was strikingly similar to helically excited azimuthal fingers. Although this type of behavior has been documented in many other sources, it has not, to this author's knowledge, been examined by systematically varying the Reynolds, Froude, and Grashof numbers. That was the focus of this research, and the results were presented as a series of false-color images to show the qualitative properties of different helium flow conditions, and these flow conditions were further evaluated by reducing the data gathered in terms of helium concentration and standard deviation.

The helium side lobes formed during the experiments performed in this research bear the same resemblance to the azimuthal fingers that have been well-documented. The side lobes observed suggest that they are strongly a function of the Froude number of the helium flow, but

the Reynolds number plays a role as well. This data was presented as a function of the square root of the Grashof number and the Reynolds number for ease of comparison to other research, and the results indicated a striking similarity in the behavior of the helium side lobes to the behavior of a bifurcating jet of water injected into a brine solution. The buoyant water and helium jets have little in common other than their buoyancy, yet similar numerical values that show the water jet's tendency to bifurcate also indicate a strong possibility that the helium jet will form side lobes. Unfortunately, there are not enough data points to clearly define a region where a helium jet would be expected to form side lobes with consistency, but this research further defines this behavior pattern and is a clear indication that this phenomenon is more than a random occurrence.

5.2 Significance of Research

This research effort has further refined AFIT's FRS data acquisition system, and has also helped to explore a buoyant jet flow phenomenon that has been previously documented, but not examined in this manner. The significance lies in the ability to directly compare this research to the bifurcation study previously referenced and observe that the non-dimensional parameters chosen to characterize these two different flow fields are similar in numerical value between the two studies when either bifurcation or side jets appear in their respective environments. Additionally, it adds more literature that discusses the behavior of horizontal buoyant jets, which is still currently lacking when compared to the amount of literature available that discusses vertical buoyant jets.

5.3 Recommendations for Future Research

Monitoring the laser's wavelength output is essential to gathering good, clean data. The iodine filter's absorption notch is constant, so the laser's wavelength must remain stable throughout the data gathering session. Any drift in the wavelength, even if small, can make the difference between seeing unwanted particles in the flow field versus seeing hardly any at all. The experiments involving the helium jet required that the laser beam be spread into a sheet of light, which was accomplished with a cylindrical lens. Unfortunately, this left no way to use the wavelength meter during these experiments since its sensor required a pinpoint light source in order to be able to measure the wavelength. It would be greatly beneficial to pick off a small portion of the laser beam with an additional beam splitter before it encounters the cylindrical lens. This would allow the laser's wavelength to be continuously monitored instead of relying on instinct to tell whether or not the laser was drifting from its settings.

The test points chosen for this research required that the helium flows be able to be adjusted down to a tenth of a standard liter per minute. The only mass flow controller available that could provide this kind of resolution was limited to a maximum flow rate of 30 SLPM. This limitation reduced the potential size of the test matrix, so it would have been ideal to have a mass flow controller that was adjustable from 0 – 100 SLPM in increments of ± 0.1 SLPM. Alicat Scientific makes such a mass flow controller, which is more compact, more accurate, and easier to use than the Brooks unit used in this research.

Additionally, the entire flow field setup and camera should be moved around on the optics table to see if the room currents are different at different locations. This change could have potentially eliminated the crescent moon behavior that was observed, but since this was

realized only after all of the data had been taken and reduced, it was too late to go back and fix this one thing that could have had a simple solution. In the end, it had no bearing on the overall results, but is another variable that should be eliminated if possible.

These small changes to the experimental setup would allow for the acquisition of a greater amount of data to help characterize the horizontal buoyant side jet phenomenon. Future research should focus on gathering more points to help fill in the Grashof versus Reynolds number plot, and further define the regions where this behavior is most likely to occur. Additional flow field properties, such as the temperature, pressure, and velocity might also yield additional insight into the side jet behavior, and thus make it easier to distinguish this phenomenon from a simple breakdown of the helium jet core.

Appendix A: Additional Iodine Filter Characterization Plots

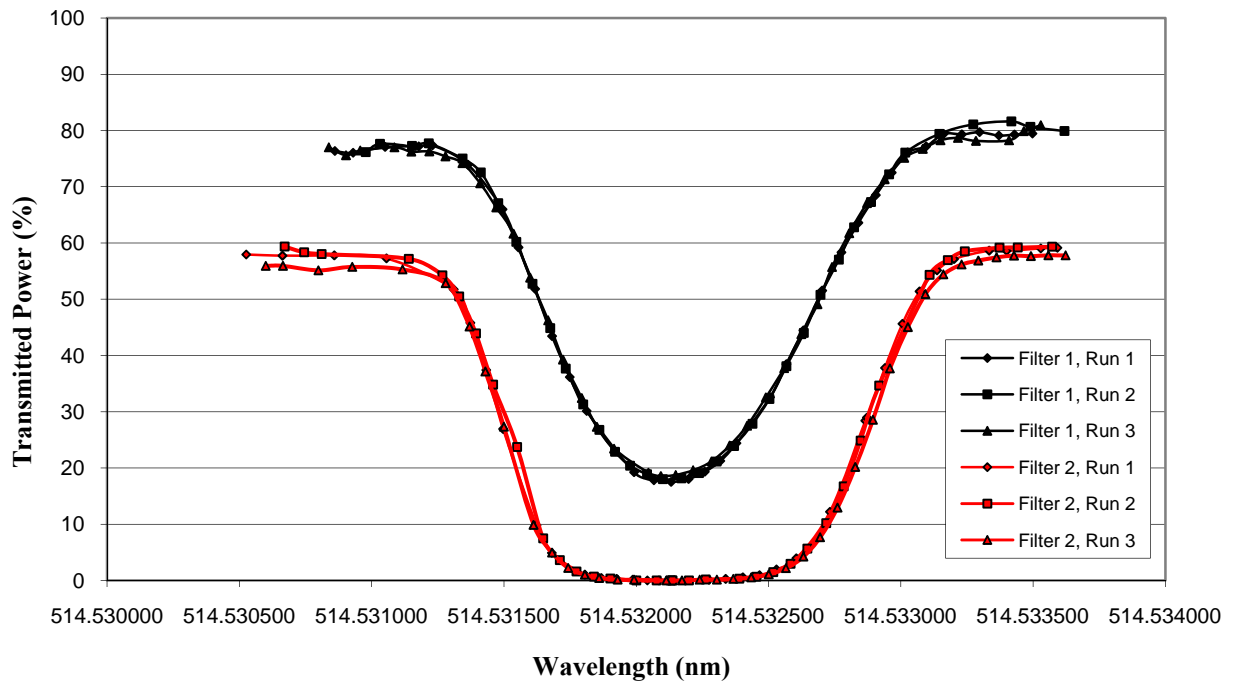


Figure 67. Results of the iodine filter characterization for the two filters available for testing plotted versus wavelength. The black lines represent three separate runs for the first filter, and the red lines represent the three runs provided by the second, deeper filter.

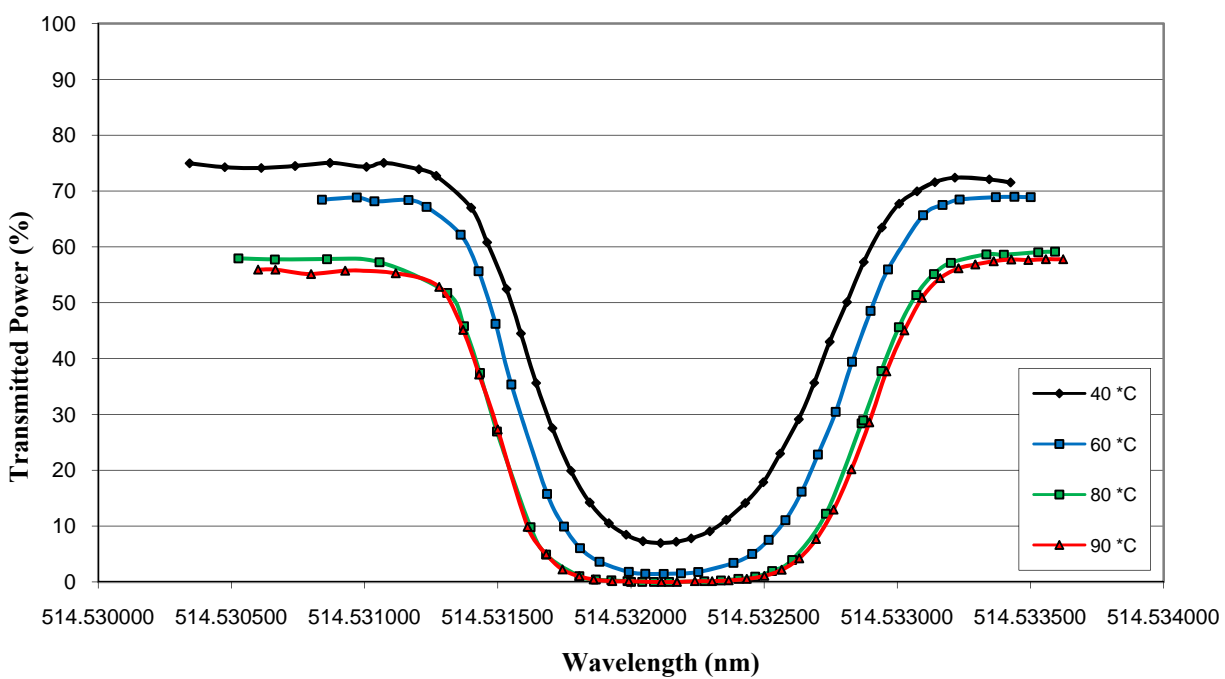


Figure 68. Results of the characterization of iodine Filter 2 at various temperatures plotted versus wavelength.

Bibliography

1. Adrian, R. J., "Twenty years of particle image velocimetry," *Experiments in Fluids*, Vol. 39, pp. 159-169, 2005.
2. Miles, R. and Lempert, W., "Flow diagnostics in unseeded air," *28th Aerospace Sciences Meeting*. 8-11 January 1990. Reno, NV. AIAA Paper 1990-624.
3. McCartney, Earl J. Optics of the Atmosphere: Scattering by Molecules and Particles, John Wiley and Sons, 1976.
4. Miles, R., Qian, L., and Zaidi, S.H., "Imaging flow structure and species with atomic and molecular filters," *Optics and Lasers in Engineering*, Vol. 44, pp. 240-260.
5. Boguszko, M. and Elliot, G.S., "Property measurement utilizing atomic/molecular filter-based diagnostics," *Progress in Aerospace Sciences*, Vol. 41, pp. 93-142.
6. Law, Adrian Wing-Keung, Wang, Hongwei, and Herlina, "Combined Particle Image Velocimetry/Planar Laser Induced Fluorescence for Integral Modeling of Buoyant Jets," *Journal of Engineering Mechanics*, Vol. 129, pp. 1189-1196.
7. Jiang, X. and Luo, K.H., "Dynamics and structure of transitional buoyant jet diffusion flames with side-wall effects," *Combustion and Flame*, Vol. 133, pp. 29-45.
8. Miceli, David S., "Characterizing a Co-flow Nozzle for use in a Filtered Rayleigh Scattering System," Master of Engineering thesis, Department of Aeronautics, AFIT, WPAFB, OH, 2006.
9. McGaha, Christopher C., "Filtered Rayleigh Scattering Measurements in a Buoyant Flow Field," Master of Engineering thesis, Department of Aeronautics, AFIT, WPAFB, OH, 2007.
10. Lee, J., Won, S.H., Jin, S.H. and Chung, S.H. (2003), "Lifted flames in laminar jets of propane in coflow air," *Combustion and Flame*, Vol. 135, pp. 449-462.
11. Miles, Richard B., Yalin, Azer P., Tang, Zhen, Zaidi, Shoail H. and Forkey, Joseph N, "Flow field imaging through sharp-edged atomic and molecular 'notch' filters," *Institute of Physics Publishing. Measurement Science and Technology*, Vol. 12, pp. 442-451.
12. Boguszko, Martin and Elliot, Gregory S., "Measurements in Fluid Flows Using Molecular Filter-based Techniques," *42nd AIAA Aerospace Sciences Meeting and Exhibit*. 5-8 January 2004. Reno, NV. AIAA Paper 2004-18.
13. Forkey, J.N., "Development and Demonstration of Filtered Rayleigh Scattering—A Laser Based Flow Diagnostic for Planar Measurement of Velocity, Temperature and Pressure," *Ph.D. dissertation #2067-T*, Princeton University, 1996.

14. Seasholtz, Richard G. and Buggele, Alvin E., "Improvement in Suppression of Pulsed Nd:YAG Laser light with Iodine Absorption Cells for Filtered Rayleigh Scattering Measurements," NASA Technical Memorandum 113177.
15. Munson, Bruce R., Young, Donald F., and Okiishi, Theodore H. Fundamentals of Fluid Mechanics, Third Edition, John Wiley and Sons, Inc., 1998.
16. White, Frank M. Viscous Fluid Flow, Third Edition, McGraw-Hill, 2006.
17. Borg, A., Bolinder, J. and Fuchs, L., "Simultaneous velocity and concentration measurements in the near field of a turbulent low-pressure jet by digital particle image velocimetry-planar laser induced fluorescence," *Experiments in Fluids*, Vol. 31, pp. 140-152.
18. Helmer, D.B. and Su, L.K., "Imaging of turbulent buoyant jet mixing," AIAA paper 2006-396. 44th AIAA Aerospace Sciences Meeting and Exhibit, January 9-12, 2006 Reno, NV.
19. Arakeri, Jaywant H., Das, Debopam and Srinivasan, J., "Bifurcation in a buoyant horizontal laminar jet," *Journal of Fluid Mechanics*, Vol. 412, pp. 61-73.
20. Papantoniou, D. and List, E.J., "Large-scale structure in the far field of buoyant jets," *Journal of Fluid Mechanics*, Vol. 229, pp. 151-190, 1989.
21. Helmer, D.B., Brownell, C.J., and Su, L.K., "Experimental Investigations of Mixing in Turbulent Jets with Buoyancy," AIAA Paper 2007-1314, 45th AIAA Aerospace Sciences Meeting and Exhibit, Reno NV, Jan. 8-11, 2007.
22. Pitts, W.M. and Johnson, A.W., "Mixing behavior of absolutely unstable axisymmetric shear layers forming side jets," 1997.
23. Monkewitz, P.A. and Pfizenmaier, E., "Mixing by 'side jets' in strongly forced and self-excited round jets," *Physics and Fluids*, Volume 3, No. 5, May 1991.
24. Chao, Y.C., Jong, Y.C., and Sheu, H.W., "Helical mode excitation of lifted flames using piezoelectric actuators," *Experiments in Fluids*, Vol. 28, 2000, pp. 11-20.
25. Operator's Manual. The Coherent INNOVA® Sabre™ R Series Ion Laser. Coherent Inc., 2001.
26. Operator's Manual. PCO.4000 Cooled Digital 14-bit CCD Camera System. The Cooke Corporation, 2008.
27. Operator's Manual. FastCam-X 1280 PCI Hardware Manual, Rev. 1.0. Photron Limited, 2002.

28. Operator's Manual. Bristol Instruments Model 621 Laser Wavelength Meter. Bristol Instruments, Inc., 2005.
29. "Fieldmaster" at <http://www.coherent.com/Lasers/index.cfm?fuseaction=show.page&id=254&loc=830>. Published: 2008. Accessed: 14 January 2008.
30. "Fixed Lens Mounts" at http://www.thorlabs.com/NewGroupPage9.cfm?ObjectGroup_ID=1433&pn=LMR2&CFID=10093111&CFTOKEN=53524232. Published: Unknown. Accessed: 11 January 2008.
31. "Beam Sampler" at http://www.thorlabs.com/NewGroupPage9.cfm?ObjectGroup_ID=913&visNavID=149. Published: Unknown. Accessed: 11 January 2008.
32. " $\lambda/10$ Aluminum Mirrors" at http://www.thorlabs.com/NewGroupPage9.cfm?ObjectGroup_ID=264&pn=PF10-03-G01. Published: Unknown. Accessed: 11 January 2008.
33. "Digital/Analog Gas Flow Controllers" at <http://www.alicatscientific.com/products/gas-flow-controller.php>. Published: 2005. Accessed: 21 January 2008.
34. "Brooks Instrument Flow Measurement and Control Product Selection Guide" at http://www.lirasrl.it/PDF/brooks/SP210_eng.pdf. Published: 2003. Accessed: 21 January 2008.
35. Operator's Manual. Alicat Scientific 16 Series Mass and Volumetric Precision Gas Flow Controller. Alicat Scientific, Inc., 2005.
36. Mosedale, A., Elliott, G.S., Carter, C.D., and Beutner, T.J., "Planar Doppler velocimetry in a large-scale facility," AIAA Paper 2006-835.
37. Shirley, J.A. and Winter, M., "Air-Mass Flux Measurement System Using Doppler-Shifted Filtered Rayleigh Scattering," AIAA Paper 93-0513, 31st Aerospace Sciences Meeting & Exhibit, Reno NV, January 11-14, 1993.

Vita

Captain Steven M. Meents is a 2003 graduate of the United States Air Force Academy, where he received a Bachelor of Science degree in Mechanical Engineering. After graduation, he was stationed at Eglin Air Force Base, FL where he was assigned to the 46th Test Wing's Air-to-Air Missile Test Flight. He became certified as a test engineer, and was responsible for the coordination and execution of test plans for the next generation AIM-9X, ASRAAM, and AMRAAM air-to-air missiles that were under development.

Captain Meents was next assigned to the Air Force Institute of Technology at Wright-Patterson Air Force Base in Dayton, OH, and enrolled in the Aeronautical Engineering Master's degree program. Upon completion of this assignment, he has been selected to join the National Air and Space Intelligence Center, where he will continue to serve his country as an engineer in the United States Air Force.

REPORT DOCUMENTATION PAGE			Form Approved OMB No. 0704-0188	
<p>The public reporting burden for this collection of information is estimated to average 1 hour per response, including the time for reviewing instructions, searching existing data sources, gathering and maintaining the data needed, and completing and reviewing the collection of information. Send comments regarding this burden estimate or any other aspect of this collection of information, including suggestions for reducing this burden to Department of Defense, Washington Headquarters Services, Directorate for Information Operations and Reports (0704-0188), 1215 Jefferson Davis Highway, Suite 1204, Arlington, VA 22202-4302. Respondents should be aware that notwithstanding any other provision of law, no person shall be subject to any penalty for failing to comply with a collection of information if it does not display a currently valid OMB control number. PLEASE DO NOT RETURN YOUR FORM TO THE ABOVE ADDRESS.</p>				
1. REPORT DATE (DD-MM-YYYY) 14-03-2008		2. REPORT TYPE Master's Thesis		3. DATES COVERED (From — To) Jul 2007 — Mar 2008
4. TITLE AND SUBTITLE Filtered Rayleigh Scattering Measurements in a Buoyant Flow Field		5a. CONTRACT NUMBER JON ENY 07-116		
		5b. GRANT NUMBER		
		5c. PROGRAM ELEMENT NUMBER		
6. AUTHOR(S) Steven M. Meents, Capt, USAF		5d. PROJECT NUMBER		
		5e. TASK NUMBER		
		5f. WORK UNIT NUMBER		
7. PERFORMING ORGANIZATION NAME(S) AND ADDRESS(ES) Air Force Institute of Technology Graduate School of Engineering and Management (AFIT/EN) 2950 Hobson Way WPAFB OH 45433-7765		8. PERFORMING ORGANIZATION REPORT NUMBER AFIT/GAE/ENY/08-M22		
9. SPONSORING / MONITORING AGENCY NAME(S) AND ADDRESS(ES) AFRL/RZAS 1950 Fifth Street WPAFB, OH 45433-7251		10. SPONSOR/MONITOR'S ACRONYM(S)		
		11. SPONSOR/MONITOR'S REPORT NUMBER(S)		
12. DISTRIBUTION / AVAILABILITY STATEMENT APPROVED FOR PUBLIC RELEASE; DISTRIBUTION UNLIMITED				
13. SUPPLEMENTARY NOTES				
14. ABSTRACT Filtered Rayleigh Scattering (FRS) is a non-intrusive, laser-based flow characterization technique that consists of a narrow linewidth laser, a molecular absorption filter, and a high resolution camera behind the filter to record images. Gases of different species have different molecular scattering cross-sections that become apparent as they pass through the interrogating laser light source, and this difference is used to discriminate between the different gaseous components. This study focuses on the behavior of a buoyant helium jet exiting horizontally into ambient air, and more specifically this jet's tendency to form side lobes that are discharged from the core fluid under low flow rate conditions. This jet behavior is documented and examined with relation to Froude, Grashof, and Reynolds numbers, and the behavior patterns are noted.				
15. SUBJECT TERMS Filtered Rayleigh Scattering, Argon Ion Laser, Continuous Wave Laser, Horizontal Buoyant Jet				
16. SECURITY CLASSIFICATION OF:		17. LIMITATION OF ABSTRACT UU	18. NUMBER OF PAGES 141	19a. NAME OF RESPONSIBLE PERSON Dr. Mark F. Reeder
a. REPORT U	b. ABSTRACT U			c. THIS PAGE U